University of California

Los Angeles

Nanocluster Nucleation in Expanding Gas Nozzles and Well-Stirred Reactors

A dissertation submitted in partial satisfaction

of the requirements for the degree

Doctor of Philosophy in Nuclear Engineering

by

Gregory A. Johnson

2003

The dissertation of Gregory A. Johnson is approved.

Ann R. Karagozian

Adrienne G. Lavine

Xiang Zhang

George J. Morales

Nasr M. Ghoniem, Committee Chair

University of California, Los Angeles

2003

To my wife Shelley,

and my children Maggie Ann, Katie and Jack,

Whose loving support and encouragement sustained me during this work.

TABLE OF CONTENTS

List of Figures

LIST OF TABLES

Acknowledgments

I would like to thank the numerous people who helped me to perform this dissertation. First, I want to thank each member of my dissertation committee: Professor Karagozian, Professor Lavine, Professor Zhang and Professor Morales. A special thank you to my advisor, Professor Ghoniem, whose patience, support and advice helped tremendously. I would also like to express my gratitude to Dr. Shahram Sharafat for his advice and support and especially for his help with the introduction of this dissertation. I would also like to thank two of my original committee members who can no longer serve; Professor Gang Chen, who has moved on to the Massachusetts Institute of Technology (MIT), and the late Professor John Dawson, who lost his battle with cancer; my condolences to his family, friends and loved ones. I would also like to express my gratitude to Dr. Alan Von Arx for his advice and support regarding dissertation preparation and presentation.

I would like to thank The Boeing Company for providing financial support and for allowing me to use their computer resources to perform many of the arduous calculations involved during this research effort. I would also like to thank my colleagues at Rocketdyne for their continuous support and encouragement.

Finally, I must acknowledge the love, support and patience of my wife and children, who endured many lonely hours during the execution of this dissertation.

Vita

1960	Born, Long Beach, California,
1983	B.S. Chemical Engineering
	California State University, Long Beach,
	Long Beach, California
1983–87	Lieutenant, US Navy
1988–present	Engineer
	The Boeing Co., Rocketdyne Division
	Los Angeles, California
1994	M.S. Nuclear Engineering
	University of California, Los Angeles
	Los Angeles, California
1997	Licensed Professional Engineer
	Mechanical Engineering
	State of California

PUBLICATIONS

G. A. Johnson and N. M. Ghoniem, *"Hierarchical Modeling of C and Si Nanocluster Nucleation Utilizing Quantum and Statistical Mechanics,"* J. Computer-Aided Materials Design, **6:** 337-347, 1999.

Abstract of the Dissertation

Nanocluster Nucleation in Expanding Gas Nozzles and Well-Stirred Reactors

by

Gregory A. Johnson

Doctor of Philosophy in Nuclear Engineering

University of California, Los Angeles, 2003

Professor Nasr M. Ghoniem, Chair

Methods of developing nanophase materials of controlled and uniform size distribution are critical to many emerging electronic and mechanical applications. The objective of this thesis is to develop a hierarchy of models, based on quantum chemistry, statistical mechanics and the theory of rate processes, to enable a complete description of the nucleation and growth of nanoclusters of controlled size distributions. The model is applied to the process of nanocluster nucleation in expanding plasma or combustion nozzles, and is compared to the experimental results of the Minnesota group. The energetics of Si and C clusters containing up to size 10 atoms have been developed using ab initio and semi-empirical quantum mechanics. Rate constants have been developed for determining Si clustering rates as a function of time. The results of these calculations compare well to published experimental data.

CHAPTER 1

Introduction

In recent years, nanophase materials have become of great interest. A nanophase material is a material made up of very small grains. The size of these grains is on the order of 100 nanometers or less and each grain contains fewer than tens of thousands of atoms. Conventional materials, on the other hand, consist of grains ranging from microns to millimeters and each contains several billion atoms[Sie96]. The small size of the grains plus the distribution of the grain size is what gives nanophase materials their unique properties, many of which are still under investigation.

The application or use of nanophase materials is endless and is only dependent on the imagination of the designer. For instance, nanophase metals are many times stronger than their conventional counterparts are. This is because the smallness of the grain size prevents the development of large numbers of dislocations. Dislocation glide is the method by which metals fail. Lacking large numbers of dislocations, nanophase metals cannot easily support dislocation glide and are hence much stronger[Sie96]. Nanophase metals, such as aluminum, could be used in aerospace structures, increasing the strength to weight ratio significantly and making the craft significantly lighter.

On the other hand, nanophase ceramics are much more ductile than their conventional counterparts. They can be deformed up to 60 percent before breaking. This unique feature can again be attributed to the smallness of the grains.

Nanometer size grains, it turns out, are much more likely to slide over one another than larger size ones. This grain boundary sliding process is the fundamental way in which nanophase ceramics are deformed[Sie96, Kar87]. In the past, the inherent difficulty in using ceramics has been their brittleness. Using nanophase ceramics can open up many new opportunities and technological advances where the use of conventional ceramics has failed. For instance, ceramics are sometimes the only materials which can be used on technologies requiring high-temperatures. However, the brittleness of the ceramic may have impeded or prevented the technology from being fully developed. The use of nanophase ceramics can resurrect these technologies allowing them to come to fruition.

In addition to mechanical properties, the electrical, magnetic, chemical, and optical properties of nanophase materials can be tailored to meet specific needs as well. Controlling the grain size distribution is essential in tailoring these properties. For example, particles less than 50 nanometers in size are too small to scatter visible light (i.e. wavelengths from 380 to 765 nanometers). A nanophase material with grain sizes less than 50 nanometers would be transparent[Sie96]. In fact, transparent nanophase ceramics have been made from materials for which their conventional counterparts are opaque[Sie96]. By controlling the grain size distribution, the wavelengths at which light is scattered can be tailored. Coatings could be developed with tailorable optical properties providing an added degree of freedom for technology development. Other areas of interest are Artificial Dielectrics[Pan96, TA95, AT95b, AT95a, Kon97], Microstrains[Kon97], Magnets[Sub98, Fan98, Gaz98], Giant Magneto Resistors[Kai98, Kno98, Chi98, Wan98], and Doped Nanoparticles[Car98b, Car98a].

Again, the key in using nanophase materials is the control of the grain size and size distribution allowing the properties of the material to be tailored for

the specific need. Theoretical methods for accurately determining the properties of nanophase materials based on their grain size distribution are needed to predict properties before the materials are produced. In addition, manufacturing processes are needed in which the grain size distribution can be controlled and which are scalable to volume production at low cost. Nanophase materials have been manufactured on an experimental scale by a wide variety of processes including; vapor condensation, wet chemistry, mechanical machining (e.g. milling, grinding, etc.), and plasma beam processes[Sha, Wu87]. Of all these processes, plasma processes hold the most promise for making a large variety of nanophase materials on a wide industrial type scale while controlling the grain size distribution to obtain the desired properties. The reason is that plasma processes provide additional degrees of freedom not normally available by other processes for controlling nanoparticle nucleation and deposition. Some of these are independent control of the ion and neutral densities, the temperature of each species, the kinetic energy of interaction between nano-clusters, nano-cluster deposition energy, and the ability to produce and sustain a non-equilibrium state to obtain the desired nucleation rates[Sha]. The flexibility of this process allows it to be used for making bulk material, thin films, and coatings.

The primary focus of this dissertation is to develop the models to describe the nucleation, formation, and cluster size distribution within an expanding plasma or high temperature combustion nozzle. The objective is to find ways to control the cluster size distribution, and to eliminate the characteristic tail occurring at the high end of the size distribution function. This tail is characteristic of all experimental results to date[Rao95, GC89]. The goal of this research is to develop a detailed model of sufficient accuracy to emulate experimental results. With this model, investigations of the effects of quench rate, pulsed feed mode, and other parameters of interest on the cluster size distribution can be carried

out.

In chapter 2, we provide a brief overview of quantum mechanics. Quantum mechanics is used to obtain the energetics (i.e. binding energy), geometry, rotational constants and vibrational constants of small size clusters. Methods for extrapolating the information to larger size clusters are developed. Rate constants that describe the dynamics of nano-cluster formation are developed next. Information obtained from quantum mechanics is used to calculate the rate constants. In chapter 3, we develop the gas dynamic equations for one-dimensional reacting flows. We also develop the equations for a well-stirred tank-type reactor model. The master equations which describe the nucleation phenomenon, are also developed. In addition, in order to handle the large number of equations required to describe the nucleation phenomenon, two approximation techniques are developed. In chapter 4, we present the results of the quantum mechanics calculations, and the model is compared to experimental data. Finally, a design case is presented where a reactor is sized to give a specific size distribution. In chapter 5, we present the conclusions derived from this work.

CHAPTER 2

Energetics and Reaction Rates of Nanoclusters

2.1 Introduction

The first step of this research is to develop a model of nano-cluster formation within an expanding high temperature gas nozzle, such as a plasma jet, detonation gun or combustion nozzle. Such techniques are being developed for the rapid manufacturing of nano-phase atomic clusters for many applications. This model should be of sufficient detail to accurately emulate experimental results to date. The details of this model are given below.

2.1.1 Current Approaches

The current approach for modeling the formation of nanoclusters is based on classical nucleation theory. In this approach, isolated atoms or molecules combine to form embryos. These embryos are unstable until a critical size is reached. The critical size is determined by the vapor pressure and surface tension of the material at the temperature and supersaturation of interest by use of Kelvin's equation[Atk82, SP98, Stu91].

$$\ln S = 2\gamma V / rRT \tag{2.1}$$

where

$$S \quad \text{is the supersaturation}$$

$$\gamma \quad \text{is the surface tension}$$

$$V \quad \text{is the molar volume}$$

$$r \quad \text{is the radius of the cluster}$$

$$R \quad \text{is the universal gas constant}$$

$$T \quad \text{is absolute temperature}$$

Once the critical radius is reached, atoms will condense on the surface and the cluster size will increase. This approach, however, does not reveal the time dependent nature of cluster formation or the cluster size distribution. These must be determined by other methods.

The time dependent growth and size distribution of nanoclusters can easily be modeled using reaction kinetics. Typically, clusters are assumed to grow and shrink one atom at a time[LA78, SP98]. However, provisions can be added to account for coalescence, sputtering, and fragmentation. The set of equations used to model cluster growth one atom at a time is given as[LA78, SP98, Rao95, RM89, GC89, Wei94]

$$
\begin{aligned}
\frac{\partial C_1}{\partial t} &= \sum_{j=2}^{\infty} 2^{\delta_{2,j}} k_{diss} \left(j \rightarrow j-1, 1\right) C_j - \sum_{j=1}^{\infty} k_{rec} \left(1, j \rightarrow j+1\right) C_1 C_j + Q_1 \\
\frac{\partial C_i}{\partial t} &= \left(\frac{1}{2}\right)^{\delta_{2,i}} k_{rec} \left(1, i-1 \rightarrow i\right) C_1 C_{i-1} - k_{rec} \left(1, i \rightarrow i+1\right) C_1 C_i \qquad (2.2) \\
&\quad + \; k_{diss} \left(i+1 \rightarrow 1, i\right) C_{i+1} - k_{diss} \left(i \rightarrow 1, i-1\right) C_i
\end{aligned}
$$

where

$$C_i \quad\quad\quad\quad\quad\quad \text{is the concentration of clusters of size } i \text{ atoms}$$

$k_{diss}\,(i \rightarrow i-1, 1)$ is the rate constant for dissociation of clusters of size i to size $i-1$ and 1

$k_{rec}\,(1, i \rightarrow i+1)$ is the rate constant for recombination of clusters of size i and 1 to size $i+1$

Q_1 is the monomer source term

The rate constants are usually determined by the collision rate as determined by kinetic theory of gases, multiplied by a "sticking" or accommodation coefficient[LA78, SP98, Rao95, RM89, GC89, Wei94]. The accommodation coefficient is the probability that the incident atom attaches to the cluster after suffering a collision with that cluster. An approach similar to this was used to model silicon clustering in a plasma jet by a group at the University of Minnesota[Rao95, RM89, GC89, Wei94]. They used a sticking coefficient of unity and a discrete-sectional algorithm to handle the large size clusters[Rao95, RM89, GC89, Wei94]. In the discrete-sectional approach, individual rate equations are written for the small-size clusters up to a specified size. The large-size clusters are grouped into size sections which are typically spaced logarithmically apart by particle volume[Rao95, RM89, GC89, Wei94]. The disadvantage of this modeling approach is the uncertainty and crude method of determining rate constants and the necessity to truncate the set of equations at some predetermined finite size. This size is usually picked for calculational convenience.

2.1.2   Modeling Strategy

The strategy employed in this disertation is a somewhat different approach. Here, quantum mechanics is used to determine cluster energetics for cluster sizes up to 10 atoms. With this information, rate constants can be accurately determined. Quantum-Rice-Ramsperger-Kassel (QRRK) theory[RH72, Sen92, Wes71, DW87, Kas32, Kas28b, Kas28c, Kas28a] augmented by transition state theory[Atk82, Sen92, Gla41] and collision rate theory[Atk82, SP98, Pre58] are used to determine the rate constants for the clustering reactions. Not only will rate constants be determined for monomer addition and evaporation, but also for coalescence, sputtering, and fragmentation.

Once this information is in hand, the rate equations can be developed as before. However, instead of truncating the equations at a predetermined size, the equations can be separated into two groups according to size: the first containing clusters with up to x* atoms, and the second containing clusters with more than x* atoms[VG92]. The quantity x* is some small integer that may be suggested, in some cases, by physical properties of the clusters (e.g., their stability). For the first group, a set of discrete equations describes the concentration of individual cluster sizes; the second group is characterized by an equation which represents the distribution of cluster sizes greater than x* atoms as a continuum. This set of equations can then be solved by the method of moments, a very powerful technique[VG92]. The advantage to this approach is that the set of equations describing the system is greatly reduced.

2.2 Quantum Mechanics Overview

The determination of the total energy, E_T, requires that Schrödinger's equation for the collection of atoms must be solved with all the associated nuclei and electrons in three dimensions. For a molecule with N nuclei and n electrons, the time-independent Schrödinger's equation is given by[Atk82, Sen92, Low93, Par64]

$$\left[\begin{array}{l} -\sum_{j=1}^{N} \left(\hbar^2 \big/ 2M_j \right) \nabla_j^2 - \left(\hbar^2 \big/ 2m \right) \sum_{i=1}^{n} \nabla_i^2 - \sum_{i=1}^{n} \sum_{j=1}^{N} \frac{Z_j e^2}{4\pi\varepsilon_0 |R_j - r_i|} \\ + \sum_{i=1}^{n-1} \sum_{j=i+1}^{n} \frac{e^2}{4\pi\varepsilon_0 |r_i - r_j|} + \sum_{i=1}^{N-1} \sum_{j=i+1}^{N} \frac{Z_i Z_j e^2}{4\pi\varepsilon_0 |R_i - R_j|} \end{array} \right] \Psi = E_T \Psi \quad (2.3)$$

where

$$\hbar \quad = h\big/2\pi$$

h is Planck's constant

e is the electronic charge

∇_j^2 is the Laplacian operator centered around j

R_i is the position vector for nuclei i

r_j is the position vector for electron j

ε_0 is the permittivity of vacuum

m is the mass of the electron

M_j is the mass of the jth nucleus

Ψ is the total wave function

In shorthand notation Schrödinger's equation can be written as[Sen92]

$$H\Psi = (T_N + T_e + V_{Ne} + V_{ee} + V_{NN}) \Psi = E_T \Psi \quad (2.4)$$

where

9

H is the Hamiltonian operator

T is the kinetic energy operator

V is the potential energy operator

and subscripts

N refers to nuclear components of T and V

e refers to electronic components of T and V

For the hydrogen atom, which has one nucleus (charge +e) and one electron (charge -e), Equation (2.4) can be reduced into the following familiar form:

$$\left[-\left(\hbar^2 \big/ 2\mu \right) \nabla^2 + \frac{e^2}{4\pi\varepsilon_0 r} \right] \Psi\left(r, \theta, \phi\right) = E_T \Psi\left(r, \theta, \phi\right) \qquad (2.5)$$

where

∇^2 is the Laplacian operator in spherical coordinates (r,θ,ϕ)

r is the distance between the nucleus and the electron

μ is the reduced mass, $\mu = \frac{mM}{(m+M)}$

Exact solutions of Equation (2.5) are available in the references[Low93, Par64, Atk82, Atk86, Dau83]. It should be noted that these exact solutions provide valuable insights into the electronic structure of larger atoms, since they can be viewed as being made from the hydrogen atom by suitably adding electrons and protons. In particular, hydrogen-atom-like wave functions clearly illustrate the angular dependency of electronic orbitals.

Because the exact solution of Schrödinger's equation for multi-electron, multi-nucleus systems is impossible, efforts have been directed towards the determination of approximate solutions. Most modern approaches rely on the implementation of the Born-Oppenheimer (BO) approximation[Sen92, Low93, Par64], which is based on the large difference in the masses of the electrons and the nuclei. Under the BO approximation, the total wave function can be expressed as the product of the electronic (ψ) and nuclear (η) wave functions, leading to the following electronic and nuclear Schrödinger's equations[Sen92, Low93]:

$$(T_e + V_{Ne} + V_{ee} + V_{NN})\,\psi = E_e\psi \tag{2.6}$$

$$(T_N + E_e)\,\eta = E_T\eta \tag{2.7}$$

where

T_e is the electronic kinetic energy

V_{Ne} is the potential energy for the nuclear electronic interactions

V_{ee} is the potential energy for the interactions between electrons

V_{NN} is the potential energy for the interactions between nuclei

E_e is the electronic energy

E_T is the total energy

Once the electronic Schrödinger equation is solved, the total energy of the molecule can then be obtained from the solution of the nuclear equation (2.7).

For a fixed nuclear configuration, V_{NN} would be constant; thus, the electronic Schrödinger equation can be rewritten as the following[Sen92, Low93]:

$$(T_e + V_{Ne} + V_{ee})\,\psi = \varepsilon_e \psi \tag{2.8}$$

where

$$\varepsilon_e = (E_e - V_{NN}) \tag{2.9}$$

The nuclear configuration can then be changed to establish new potential fields V_{Ne} and V_{NN}, which in turn leads to a new set of wave functions, and thus to a new electronic energy and a new total energy. By repeating this procedure for a large number of nuclear configurations, the potential energy surface can be generated.

Under the Born-Oppenheimer approximation, two major methods exist to determine the electronic structure of molecules: The valence bond (VB) and the molecular orbital (MO) methods[Sen92, Low93, Atk86]. In the valence bond method, the chemical bond is assumed to be an electron pair at the onset. Thus, bonds are viewed to be distinct atom-atom interactions, and upon dissociation molecules always lead to neutral species. In contrast, in the MO method the individual electrons are assumed to occupy an orbital that spreads the entire nuclear framework, and upon dissociation, neutral and ionic species form with equal probabilities. Consequently, the charge correlation, or the avoidance of one electron by others based on electrostatic repulsion, is overestimated by the VB method and is underestimated by the MO method[Sen92, Low93, Atk86]. The MO method turned out to be easier to apply to complex systems, and with the advent of computers it became a powerful computational tool.

In the MO approach, molecular orbitals are expressed as linear combinations of atomic orbitals (LCAO); atomic orbitals (AO), in return, are determined from

the approximate numerical solution of the electronic Schrödinger's equation for each of the parent atoms in the molecule. This is the reason why hydrogen-atom-like wave functions continue to be so important in quantum mechanics. Mathematically, MO-LCAO means that the wave functions of the molecule containing N atoms can be expressed as[Sen92, Low93, Atk86]

$$\psi_{MO} = \sum_{k=1}^{N} C_k \phi_k \tag{2.10}$$

where ϕ_k are the approximate atomic wave functions (i.e. wave functions centered around the kth atom), and C_k are the LCAO expansion coefficients. The direct implementation of the MO-LCAO to systems consisting of many nuclei and many electrons turned out to be difficult because of the three-dimensional nature of orbitals, especially in evaluating the contributions of electronic repulsions to the total energy. These difficulties are partially removed by the use of the self-consistent field (SCF) method[Sen92, Low93, Dau83].

In the SCF approach, each electron is assumed to move in an average field due to nuclei and the remaining electrons. Consequently, electronic repulsions are formally considered in the procedure. For example, consider a hypothetical atom (nuclear charge Z) containing two electrons. The electrons occupy orbitals ϕ_1 and ϕ_2, with corresponding electron densities of $-e\phi_1^2$ and $-e\phi_2^2$, respectively. According to the SCF approach, the potential seen by electron 2 would be

$$V_2 = \frac{-Ze^2}{4\pi\varepsilon_0 |R - r_2|} + \frac{e^2}{4\pi\varepsilon_0} \int \frac{\phi_1^2(r_1)}{(r_1 - r_2)} d\tau_1 \tag{2.11}$$

where the second term represents the electronic repulsion integral in which $d\tau_1$ is the volume element in the orbital ϕ_1. To determine ϕ_2, the following Schrödinger equation must be solved:

$$\left[-\left(\hbar / 2m \right) \nabla_2^2 + V_2 \right] \phi_2 = E_2 \phi_2 \tag{2.12}$$

or, in shorthand notation, the following Hartree-Fock (H-F) equation:

$$H_2^F \phi_2 = E_2 \phi_2 \tag{2.13}$$

However, as evident from these equations, ϕ_1 must be known to determine ϕ_2, and vice versa; thus, an iterative calculation would be needed. For the general case of N nuclei and n electrons, the resulting H-F expression for the wave function ϕ_1 will be

$$H_i^F \phi_i = E_i \phi \tag{2.14}$$

Since the exact solution of the Hartree-Fock equation for molecules also proved to be impossible, numerical methods approximating the solution of the Schrodinger's equation at the HF limit have been developed. For example, in the Roothan-Hall SCF method, each SCF orbital is expressed in terms of a linear combination of fixed orbital or basis sets (ϕ_i). These orbitals are fixed in the sense that they are not allowed to vary as the SCF calculation proceeds. From n basis functions, new SCF orbitals are generated by[Sen92, Low93]

$$\psi_k = \sum_{i=1}^{n} C_{k,i} \phi_i \tag{2.15}$$

and for each k, a vector of C_k values are obtained. The C_ks are then determined from the solution of the matrix Hartree-Fock equations:

$$H^F C_k = E_k S C_k \tag{2.16}$$

14

where S represents the matrix of electron overlap integrals in which

$$S_{ij} = \int \phi_i \phi_j d\tau \qquad (2.17)$$

where $d\tau$ is the volume element. Because the calculation of HF also involves the evaluation of a large number of one and two-electron integrals, the need for computational resources increases with increasing number of electrons. As an approximate guideline, computational requirements increase with the fourth power of the number of electrons present in the system.

In minimal basis sets, each atom is represented by a single orbital of each type. For example, oxygen is represented by $1s$, $2s$, $2p_x$, $2p_y$, and $2p_z$ orbitals only. In double zeta basis sets, twice the functions in the minimum basis sets are used, and in triple zeta basis sets, three times the functions as in the minimum basis sets are used[Sen92, Low93]. Extended basis sets generally refer to sets that make use of functions that are more than the minimum basis set.

Among the earlier basis sets have been the Slater-type orbitals (STO). The STO sets make use of functions of the type e^{-ar}, where r is the distance from the center of the nucleus, because of their initial use in the SCF calculations for atoms. Most of the current SCF calculations make use of Gaussian-type orbitals (GTO), in which basis sets are constructed using functions of the form e^{-br^2}. Even though the Gaussian functions have improper feature (i.e. they have the wrong behavior at $r = 0$ and they decay too fast at large r), their form helps enormously in the numerical integration of electron repulsion integrals[Sen92, Low93].

At present, two parallel approaches are being undertaken to determine the PES or the E_T: the ab initio and the semi-empirical quantum mechanical methods. Ab initio methods attempt to undertake the just-mentioned calculations rigorously without relying on the use of any information other than the basis sets

$(\phi_i$); to increase the resulting accuracy of the calculations, large basis set are used. Ab initio methods suffer from the fact that they are computationally very demanding[Sen92].

Semi-empirical methods, on the other hand, utilize minimum basis sets to speed up computations, and the loss in rigor is compensated by the use of experimental data to reproduce important chemical properties, such as the heats of formation, molecular geometries, dipole moments, and ionization potentials[Ste89, Sen92].

Most present-day semi-empirical methods are based on the idea of the neglect of differential overlap (NDO) of inner electrons developed by Pople and co-workers[PB70]. NDO-type approximations generally result in a decrease in computational resources that are 1/100 to 1/1000 of the corresponding ab initio methods.

Once the electronic Schrödinger equations are solved, the total energy of the system of atoms (E_T) is obtained by summing all the electronic energies (E_k) and the nuclear repulsions in the following manner[Sen92, Low93]:

$$E_T = \sum_{k=1}^{n} \varepsilon_k + \sum_{i=1}^{N-1} \sum_{j=i+1}^{N} \frac{Z_i Z_j e^2}{4\pi\varepsilon_0 |R_i - R_j|} \tag{2.18}$$

Following the determination of the minimum energy (i.e. the optimal geometrical configuration of the atoms), a force calculation can also be undertaken to determine the normal modes of vibration of the molecule. The entropy and specific heat of the molecule can then be calculated via the use of statistical mechanics in a straightforward manner by considering contributions from translational, rotational, and vibrational degrees of freedom[Atk82, Par64, Row94].

A number of highly sophisticated public domain software packages are avail-

able to undertake both ab initio and semi-empirical quantum mechanical calculations. Among the most popular ab initio packages are GAUSSIAN[Fri01] and GAMESS[Sch63]. Semi-empirical programs include the MNDO, AM1, and MNDO-PM3, all of which are available in MOPAC[Ste87] and GAMESS. These modern packages contain procedures to calculate optimized molecular geometries and thermochemical data as well as spectroscopic information of molecules using built-in basis sets.

2.3 Rate Constants

Cluster formation proceeds by recombination and dissociation reactions, where the recombination reactions increase the cluster size and the dissociation reactions decrease the cluster size. The method is general and can be applied to any material. However, using silicon as a representative material, these reactions may be represented as follows:

$$Si_i + Si_j \Rightarrow Si_{i+j} \tag{2.19}$$

for recombination, and

$$Si_{i+j} \Rightarrow Si_i + Si_j \tag{2.20}$$

for dissociation.

Ab initio calculations have shown that these types of reactions can be classified as simple fission reactions[Atk82, Sen92]. Simple fission reactions are characterized by a potential energy surface (PES) along the reaction coordinate which has a deep potential energy well for the combined cluster (e.g. Si_{i+j}) which rises to a
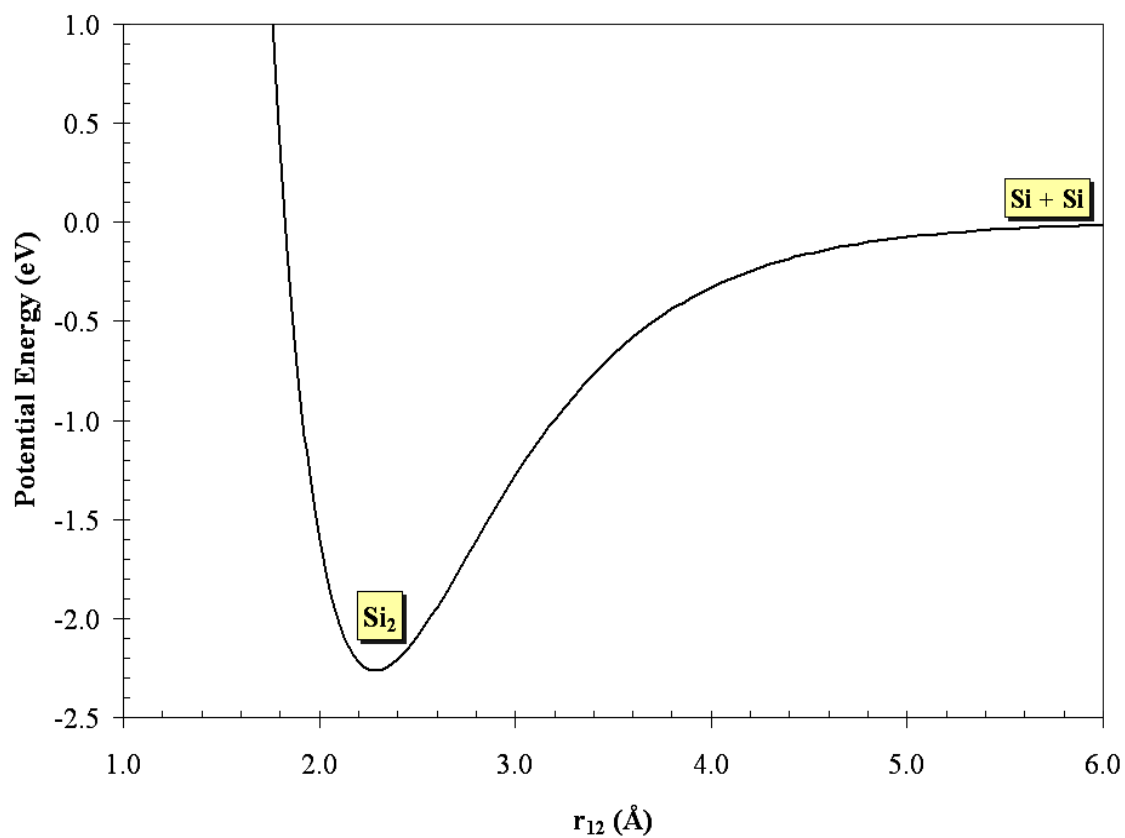
Figure 2.1: Potential Energy Surface for Silicon Dimer

potential energy plateau for the separated reactants (e.g. Si_i and Si_j) with very slight, if any, activation energy barrier. Figure 2.1 illustrates the PES for this type of reaction. The salient feature of this type of PES is the lack of a potential energy hump between the reactants and products. The activation energy for this type of reaction is commonly taken as zero for the forward (recombination) reaction and the difference between the well depth and the plateau for the reverse (dissociation) reaction.

2.3.1 Dissociation Rate Constants

For the dissociation reaction to occur, the cluster must obtain sufficient energy to surmount the energy well depth to the energy plateau. Past studies have shown that dissociating species obtain this excess energy from collisions with surrounding particles[RH72, Sen92, HA79]. Once a cluster obtains sufficient energy to dissociate, it may or may not dissociate depending on the distribution of the energy within the cluster. The mechanism for dissociation is given as

$$Si_{i+j} + M \quad \overset{k_1}{\to} \quad Si^*_{i+j} + M$$
$$Si^*_{i+j} + M \quad \overset{k_2}{\to} \quad Si_{i+j} + M \tag{2.21}$$
$$Si^*_{i+j} \quad \overset{k_3}{\to} \quad Si_i + Si_j$$
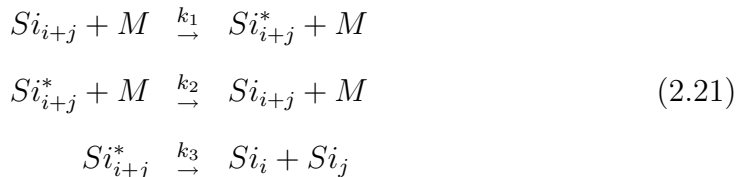
where M is a collision partner which energizes and deenergizes the cluster. Si^*_{i+j} is the energized cluster, and Si_i and Si_j are the cluster dissociation fragments. This mechanism was first proposed by Lindemann[RH72, HA79], and several modifications have been made to it since.

Two of the more recent theories in use today, which explain the reaction rate quite accurately, are the Quantum-Rice-Ramsperger-Kassel (QRRK) theory[RH72, Kas28c, HA79], and Marcus-Rice (RRKM) theory[RH72]. The RRKM theory represents the physics better, but is difficult to implement and requires several approximations. On the other hand, the QRRK theory does an adequate job of representing the physics, although not as rigorous as the RRKM theory, and is much easier to implement, and in practice, it is just as accurate as RRKM theory. For these reasons, it has been the theory of choice in representing unimolecular reaction rates and is used herein to predict the rates of cluster dissociation.

From 2.21, the rate of change of the concentration of energized clusters, Si_{i+j}^*, is

$$d[Si_{i+j}^*]\big/dt = k_1[Si_{i+j}][M] - k_2[Si_{i+j}^*][M] - k_3[Si_{i+j}^*] \qquad (2.22)$$

Assuming steady state, and upon rearrangement of equation 2.22, the concentration of energized clusters Si_{i+j}^* is found as

$$[Si_{i+j}^*] = \frac{k_1[Si_{i+j}][M]}{k_2[M] + k_3} \qquad (2.23)$$

Now the rate of dissociation is given by

$$-d[Si_{i+j}]\big/dt = k_3[Si_{i+j}^*] \qquad (2.24)$$

Substituting 2.23 into 2.24 and rearrangement gives

$$-d[Si_{i+j}]\big/dt = \frac{\frac{k_1 k_3}{k_2}[Si_{i+j}]}{1 + \frac{k_3}{k_2[M]}} \qquad (2.25)$$

which is the well-known unimolecular rate equation first proposed by Lindemann[RH72, HA79]. Two interesting features of this equation are brought out by taking the limits as $[M]$ approaches zero and infinity, which represent the lower pressure limit and the high pressure limit, respectively. These are

$$\lim_{[M]\to\infty} \left(-d[Si_{i+j}]\big/dt\right) = \frac{k_1 k_3}{k_2}[Si_{i+j}] = k_\infty[Si_{i+j}] \qquad (2.26)$$

and

$$\lim_{[M]\to 0} \left(-d[Si_{i+j}]\big/dt\right) = k_1[Si_{i+j}][M] \qquad (2.27)$$

20

where equation 2.26 is termed the high-pressure limit and equation 2.27 is called the low pressure limit[RH72]. Pressure is indicative of the concentration of M.

Application of QRRK theory to cluster dissociation notes that the cluster contains $s = 3(i + j) - 6$ normal modes of vibration or oscillators[Row94]. It is also assumed that all the oscillators vibrate at the same frequency ν [RH72, Sen92, Kas32, Kas28c]. This frequency is usually chosen as the geometric mean of all the normal mode frequencies[Sen92]. Also, in order for the reaction to take place, the cluster must obtain sufficient vibrational energy to surmount the potential energy barrier. In addition all this energy must be in the critical oscillator: the one where the bonds are broken[Kas32, Kas28c]. Since the vibrational energy is quantized, then in order for the reaction to take place, the critical oscillator must contain at least the critical number of quanta.

The number of quanta n in an oscillator with energy ε above the zero point energy is[Kas32, Kas28c]

$$n = \varepsilon/h\nu \tag{2.28}$$

The number of ways to arrange n quanta in s oscillators is[Kas32]

$$P = \frac{(n + s - 1)!}{n!(s - 1)!} \tag{2.29}$$

The critical number of quanta, m_{crit}, the critical oscillator must contain for reaction to occur is

$$m_{crit} = \varepsilon_0/h\nu \tag{2.30}$$

where ε_0 is the height of the potential energy barrier. Reaction can occur so long as the number of quanta in the critical oscillator is equal to or greater than m_{crit}.

21

The probability that the critical oscillator contains at least m_{crit} quanta is then given by[Kas32]

$$P_{m_{crit}} = \frac{(n - m_{crit} + s - 1)!}{(n - m_{crit})!(s - 1)!} \cdot \frac{n!(s - 1)!}{(n + s - 1)!} = \frac{n!(n - m_{crit} + s - 1)!}{(n - m_{crit})!(n + s - 1)!} \quad (2.31)$$

and the rate of dissociation is proportional to the probability of having sufficient number of quanta in the critical oscillator as follows[Kas32]

$$k_3 = AP_{m_{crit}} = A\frac{n!(n - m_{crit} + s - 1)!}{(n - m_{crit})!(n + s - 1)!} \quad (2.32)$$

where A is a constant of proportionality. The concentration of energized clusters, Si^*_{i+j} with respect to de-energized clusters, Si_{i+j} , can be determined using quantum statistical mechanics and assuming that the ratio does not depart too much from equilibrium. The partition function for a single cluster oscillator is[Row94]

$$q_{vib} = \frac{e^{-1/2\beta h\nu}}{1 - e^{-\beta h\nu}} \quad (2.33)$$

and for s oscillators oscillating with frequency ν, it is

$$q_{vib} = \prod_{i=1}^{s} \frac{e^{-1/2\beta h\nu}}{1 - e^{-\beta h\nu}} = \left(\frac{e^{-1/2\beta h\nu}}{1 - e^{-\beta h\nu}}\right)^{s} \quad (2.34)$$

The probability that a cluster contains n quanta in s oscillators is then given by[Kas32]

$$P_n = \frac{(n + s - 1)!}{n!(s - 1)!}\frac{\prod_{i=1}^{s} e^{-(n_i + 1/2)\beta h\nu}}{q_{vib}} = \frac{(n + s - 1)!}{n!(s - 1)!}\frac{(e^{-1/2\beta h\nu})^s e^{-n\beta h\nu}(1 - e^{-\beta h\nu})^s}{(e^{-1/2\beta h\nu})^s}$$

$$P_n = \frac{(n + s - 1)!}{n!(s - 1)!}(e^{-\beta h\nu})^n(1 - e^{-\beta h\nu})^s \quad (2.35)$$

22

where

$$\sum_{i=1}^{s} n_i = n \tag{2.36}$$

which can be equated to the concentration ratio of energized cluster to de-energized cluster and henceforth the ratio k_1/k_2 as follows from equations 2.21.

$$\frac{[Si_{i+j}^*]}{[Si_{i+j}]} = k_1/k_2 = \frac{(n+s-1)!}{n!(s-1)!}(e^{-\beta h\nu})^n(1-e^{-\beta h\nu})^s \tag{2.37}$$

From equation 2.36 the rate constant at the high pressure limit is then

$$\frac{k_1 k_3}{k_2} = \sum_{n=m_{crit}}^{\infty} A\frac{n!(n-m_{crit}+s-1)!}{(n-m_{crit})!(n+s-1)!}\frac{(n+s-1)!}{n!(s-1)!}(e^{-\beta h\nu})^n(1-e^{-\beta h\nu})$$

$$\frac{k_1 k_3}{k_2} = \sum_{n=m_{crit}}^{\infty} A\frac{(n-m_{crit}+s-1)!}{(n-m_{crit})!(s-1)!}(e^{-\beta h\nu})^n(1-e^{-\beta h\nu})^s \tag{2.38}$$

Substituting $p = n - m_{crit}$ into equation 2.38 and rearranging gives

$$\frac{k_1 k_3}{k_2} = A(e^{-\beta h\nu})^{m_{crit}}(1-e^{-\beta h\nu})^s \sum_{p=0}^{\infty} \frac{(p+s-1)!}{(p)!(s-1)!}(e^{-\beta h\nu})^p \tag{2.39}$$

Using the binomial expansion theorem, it can be shown that

$$(1-e^{-\beta h\nu})^{-s} = \sum_{p=0}^{\infty} \frac{(p+s-1)!}{p!(s-1)!}(e^{-\beta h\nu})^p \tag{2.40}$$

Therefore, using equation 2.40, equation 2.39 reduces to[Kas32, Kas28c]

$$k_\infty = Ae^{-m\beta h\nu} = Ae^{-\varepsilon_0/kT} \tag{2.41}$$

which is an Arrenhius type equation.

The constant A can be evaluated with the help of Absolute Rate Theory, commonly referred to as Transition State Theory or Activated Complex Theory. This theory has been shown to be accurate in the high-pressure limit or when the rate is independent of the rate of energization or de-energization. This theory assumes that the reactants get together to form an Activated Complex which then proceeds to transition to products as illustrated below[Gla41].

$$Si_{i+j} \leftrightarrow Si^{\ddagger}_{i+j} \rightarrow Si_i + Si_j \tag{2.42}$$
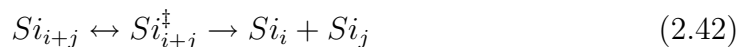
where $Si^{\ddagger}_{i+j}$ is the activated complex or transition state between reactants and products. The activated complex is a position on the potential energy surface (PES) which is a relative maxima along the reaction coordinate and a relative minima in the other directions. This is referred to as a saddle point on the PES. Because of the shape of the PES at the saddle point, the activated complex is unstable. The rate of product formation is thus given as

$$\frac{d[Si_i]}{dt} = k^{\ddagger}[Si^{\ddagger}_{i+j}] \tag{2.43}$$

where it has been shown[Atk82, Gla41, Joh66]

$$k^{\ddagger} = \frac{kT}{h} \tag{2.44}$$

where h is Planck's constant.

The ratio of activated complex concentration to reactant concentration can be determined by the ratio of their respective partition functions, as follows[Gla41, Joh66]

$$\frac{[Si_{i+j}^{\ddagger}]}{[Si_{i+j}]} = \frac{q_{trans}^{\ddagger} q_{rot}^{\ddagger} q_{vib}^{\ddagger}}{q_{trans}^{i+j} q_{rot}^{i+j} q_{vib}^{i+j}} e^{-\varepsilon_0/kT} \tag{2.45}$$

where $q_x^{\ddagger}$ is the partition function of energy mode x for the activated complex, and q_x^{i+j} is the partition function of energy mode x for the reactant cluster. Using 2.44 and 2.45, equation 2.43 becomes

$$\frac{d[Si_i]}{dt} = \left(\frac{kT}{h}\right) \frac{q_{trans}^{\ddagger} q_{rot}^{\ddagger} q_{vib}^{\ddagger}}{q_{trans}^{i+j} q_{rot}^{i+j} q_{vib}^{i+j}} e^{-\varepsilon_0/kT} [Si_{i+j}] \tag{2.46}$$

Comparing equation 2.41 to 2.46 one can deduce that

$$A = \left(\frac{kT}{h}\right) \frac{q_{trans}^{\ddagger} q_{rot}^{\ddagger} q_{vib}^{\ddagger}}{q_{trans}^{i+j} q_{rot}^{i+j} q_{vib}^{i+j}} \tag{2.47}$$

To determine the rate of de-energization, k_2 in equations 2.21, we make the assumption that every collision with a collision partner M striking an energized cluster Si_{i+j}^* results in it being de-energized. This is known as the strong collision assumption[Kas32, Kas28b]. Because the energized cluster is in such a high energy state, it is extremely likely that a single collision will de-energize it sufficiently to prevent it from reacting. Based on this assumption and using the kinetic theory of gases for the collision rate, the rate of de-energization can be written as[Kas32, Kas28b, Pre58]

$$k_2[Si_{i+j}^*][M] = [Si_{i+j}^*][M]\sigma\sqrt{\frac{8kT}{\pi m_{i+j}} + \frac{8kT}{\pi m_M}} \tag{2.48}$$

which gives a rate constant for de-energization of

$$k_2 = \sigma\sqrt{8kT/\pi\mu} \tag{2.49}$$

25

where σ is the collision cross-section and μ is the reduced mass of the two collision species. Using the results from equations 2.25, 2.32, 2.41, 2.47, and 2.49, the rate constant for dissociation of cluster Si_{i+j} becomes

$$k_{diss}\left(i+j \rightarrow i,j\right) = Ae^{-\varepsilon_0/kT}(1-e^{-\beta h\nu})^s \sum_{p=0}^{\infty} \frac{\frac{(p+s-1)!}{p!(s-1)!}e^{-p\beta h\nu}}{1+\frac{A\frac{(p+m_{crit})!(p+s-1)!}{p!(p+m_{crit}+s-1)!}}{\sigma\sqrt{8kT/\pi\mu}[M]}} \qquad (2.50)$$

2.3.2 Recombination Rate Constants

Now let's examine the recombination or clustering reaction. This reaction is also classified as energy transfer limited[Sen92]. To illustrate, we will use the same PES as the dissociation reaction, where the energy barrier between reactants and products is very slight or non-existent. When the reactants combine, the new cluster will posses excess internal energy. The excess internal energy is sufficient to cause the newly formed cluster to dissociate. The excess energy must be removed quickly in order for the cluster to survive. The mechanism for this energy removal process is collisions with the bath gas M[Wes71, DW87, GT84]. The reaction mechanism can be summarized as follows[GT84].

$$
\begin{aligned}
Si_i + Si_j &\overset{k_4}{\rightarrow} Si_{i+j}^* \\
Si_{i+j}^* &\overset{k_3}{\rightarrow} Si_i + Si_j \\
Si_{i+j}^* + M &\overset{k_2}{\rightarrow} Si_{i+j} + M
\end{aligned}
\qquad (2.51)
$$
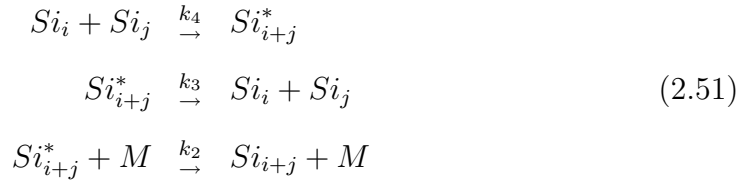
The rate of cluster formation is given by

$$\frac{d[Si_{i+j}^*]}{dt} = k_4[Si_i][Si_j] - k_3[Si_{i+j}^*] - k_2[Si_{i+j}^*][M] \qquad (2.52)$$

Assuming steady state and rearrangement gives

$$[Si^*_{i+j}] = \frac{k_4[Si_i][Si_j]}{k_3 + k_2[M]} \tag{2.53}$$

Inserting this into equation 2.52 gives

$$\frac{d[Si_{i+j}]}{dt} = \frac{k_2 k_4[Si_i][Si_j][M]}{k_3 + k_2[M]} \tag{2.54}$$

Upon rearrangement this gives

$$\frac{d[Si_{i+j}]}{dt} = \frac{k_4[Si_i][Si_j]}{1 + k_3/k_2[M]} \tag{2.55}$$

which gives a rate constant of

$$k_{rec} = \frac{k_4}{1 + k_3/k_2[M]} \tag{2.56}$$

This leads to the following high and low pressure limits.

$$\lim_{[M]\to\infty} k_{rec} = k_\infty = k_4$$

$$\lim_{[M]\to 0} k_{rec} = k_0 = \frac{k_2 k_4[M]}{k_3}$$

Rate constants k_2 and k_3 have already been treated in the previous section. The only new information we need is an expression for k_4. At equilibrium, the rate of cluster formation must equal the rate of cluster dissociation[GT84]. Then, using equations 2.25 and 2.56, we have

$$\frac{k_4}{1 + k_3/k_2[M]} [Si_i] [Si_j] = \frac{k_1 k_3/k_2}{1 + k_3/k_2[M]} [Si_{i+j}] \tag{2.57}$$

27

Rearrangement gives

$$\frac{k_4 k_2}{k_1 k_3} = \frac{[Si_{i+j}]}{[Si_i][Si_j]} = K_{equilibrium} \tag{2.58}$$

But, from statistical mechanics

$$K_{equilibrium} = \frac{q_{i+j}}{q_i q_j} e^{-\varepsilon_0/kT} \tag{2.59}$$

Combining equations 2.58 and 2.59 gives

$$k_4 = \frac{k_1 k_3}{k_2} \frac{q_{i+j}}{q_i q_j} e^{-\varepsilon_0/kT} \tag{2.60}$$

Inserting equations 2.32 and 2.35 into 2.60 gives upon rearrangement

$$k_4 = A' \frac{(n - m_{crit} + s - 1)!}{(n - m_{crit})!(s-1)!} (e^{-\beta h\nu})^{(n-m_{crit})} (1 - e^{-\beta h\nu})^s \tag{2.61}$$

where

$$A' = A \frac{q_{i+j}}{q_i q_j} = \left(\frac{kT}{h}\right) \frac{q_{i+j}^{\ddagger}}{q_i q_j} \tag{2.62}$$

Combining terms, the rate of cluster formation is given by

$$k_{rec}(i, j \rightarrow i + j) = A'(1 - e^{-\beta h\nu})^s \sum_{p=0}^{\infty} \frac{\frac{(p+s-1)!}{p!(s-1)!} e^{-p\beta h\nu}}{1 + \frac{A \frac{(p+m_{crit})!(p+s-1)!}{p!(p+m_{crit}+s-1)!}}{\sigma \sqrt{8kT/\pi\mu^{[M]}}}} \tag{2.63}$$

2.3.3 Supporting Rate Constant Data

2.3.3.1 Frequency of Vibration

In order to use the model described to determine the rates of cluster agglomeration, we must first determine the appropriate vibration frequency to use. For clusters of up to 10 atoms in size, detailed ab initio calculations have been performed and all the normal modes of vibration are known. In this case, many researchers have used the geometric mean of all the normal modes with satisfactory results[Sen92]. A slightly different approach is used herein. From statistical mechanics, the heat capacity for an ideal gas is given as[Row94]

$$c_v/k = \frac{3}{2} + \frac{3}{2} + \sum_{j=1}^{3i-6} \left(\frac{h\nu_j}{kT}\right)^2 \left[\frac{e^{-h\nu_j/kT}}{\left(e^{-h\nu_j/kT} - 1\right)^2}\right] \qquad (2.64)$$

where i is the cluster size, the two $3/2$ terms account for translation and rotation and the summation term accounts for the $3i - 6$ modes of vibration. Equating the vibration contribution of equation 2.64 to an average vibration frequency $\bar{\nu}$ gives

$$(3i-6)\left(\frac{h\bar{\nu}}{kT}\right)^2 \left[\frac{e^{-h\bar{\nu}/kT}}{\left(e^{-h\bar{\nu}/kT} - 1\right)^2}\right] = \sum_{j=1}^{3i-6}\left(\frac{h\nu_j}{kT}\right)^2 \left[\frac{e^{-h\nu_j/kT}}{\left(e^{-h\nu_j/kT} - 1\right)^2}\right] \qquad (2.65)$$

which can be solved for the average vibration frequency $\bar{\nu}$. For cluster sizes greater than ten, the normal modes of vibration are not known a priori. A closer examination of equation 2.65 reveals that the term on the left hand side is of the form of the Einstein model of a crystalline solid[Row94]. Using published data for the heat capacity of the crystalline solid, the average vibrational frequency can be deduced using the Einstein model. This frequency has been determined
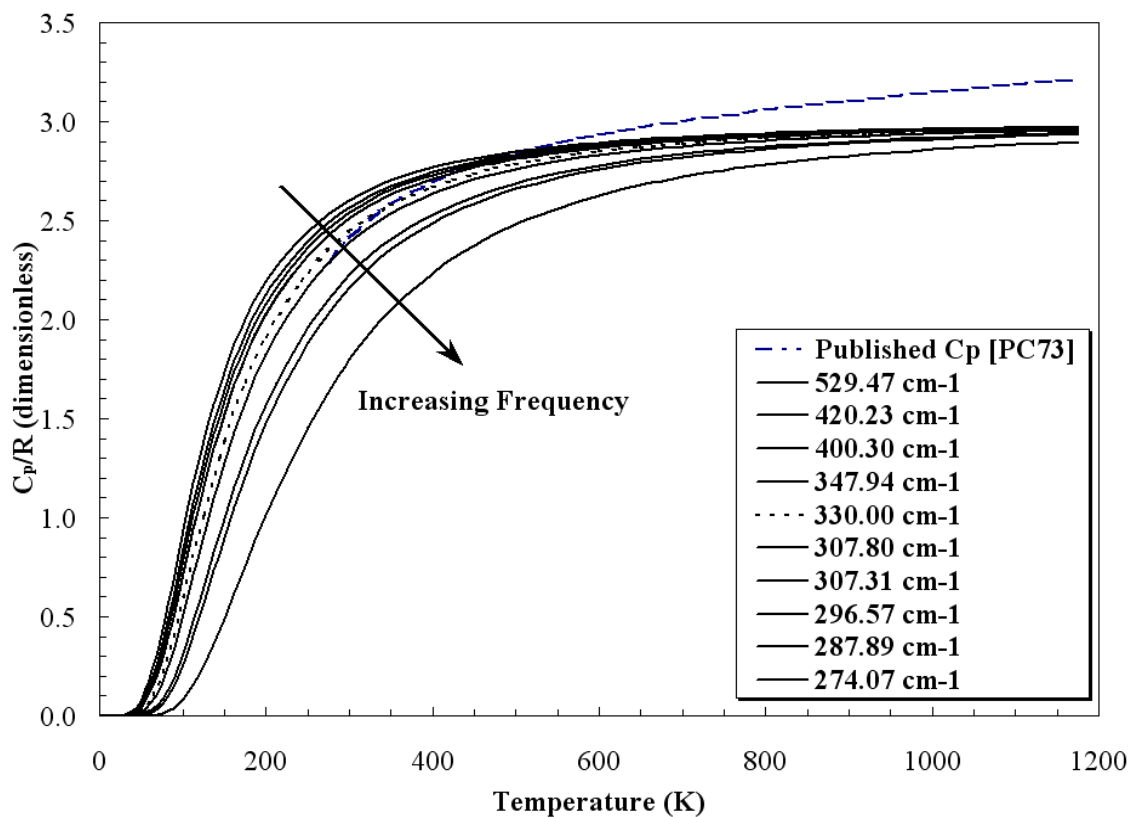
Figure 2.2: Silicon Crystalline Solid Average Vibrational Frequency from Heat Capacity Data

to be 330 cm^{-1} and is compared to the heat capacity reported in Ref. [PC73] (see Figure 2.2).

2.3.3.2 Moments of Inertia

In addition to the average vibrational frequency, the rotational partition function is needed to determine several of the constants in the rate equation. For clusters of up to size ten, the principal moments of inertia and thus the rotational partition function have been determined for the cluster. For larger size clusters, the

principal moments of inertia must be estimated. Assuming the clusters are spherical, the three principle moments of inertia are equivalent and can be determined from standard formulas. The moment of inertia for a sphere is[Lin84]

$$I = \tfrac{2}{5}mr^2 \tag{2.66}$$

where
$$\begin{aligned} m &\quad \text{is mass} \\ r &\quad \text{is radius} \end{aligned}$$

Using the molecular weight, mw, and density of the solid, ρ, the moment of inertia of a cluster of size j is

$$I_j = \tfrac{2}{5}(j \cdot mw)^{5/3} \left(\frac{3}{4\pi\rho}\right)^{2/3} \tag{2.67}$$

To determine the moments of inertia for the transition states, the parallel axis theorem is used[Lin84]. This gives

$$I_{i+j}^{\ddagger} = I_i + I_j + \mu_{ij}r_{ij} \tag{2.68}$$

where
$$\begin{aligned} \mu_{ij} &\quad \text{is the reduced mass of the cluster pair, } i \text{ and } j \\ r_{ij} &\quad \text{is the separation distance between the cluster pair } i \text{ and } j \end{aligned}$$

In addition, detailed study of the silicon dimer reaction indicates that the rotational energy barrier occurs at a separation distance of around 9 Å. This distance was used when applying equation 2.68 to determine the moments of inertia of the transition state.

2.3.3.3 Rotational Symmetry

Rotational symmetry is also needed to determine the rotational partition functions. Rotational symmetry is the number of distinct rotations that produce indistinguishable configurations. For instance, the water molecule has a rotational symmetry of two because there are two distinct rotations, and the methane molecule has a rotation symmetry of twelve. Figure 2.3 is a plot of silicon rotational symmetry as a function of cluster size. From ab initio calculations, the rotational symmetry is known for clusters up to size 10. It is also known that bulk silicon crystal has a rotational symmetry number of 36. An interpolation equation is needed to estimate rotational symmetry beyond size 10. An exponential function was proposed because it rapidly and asymptotically approaches the bulk crystalline rotational symmetry number. This function is given as follows:

$$\sigma = \sigma_a e^{-\lambda i} + \sigma_b \left(1 - e^{-\lambda i}\right) \tag{2.69}$$

where, for silicon,

σ is the cluster rotational symmetry number

σ_a $= 1.85$

σ_b $= 36$

λ $= 0.008$

i is the number of atoms in the cluster

2.3.3.4 Degeneracy

For most reactions between small molecules, degeneracy is accounted for by the rotational symmetry numbers. Take methane for example. The methane mole-
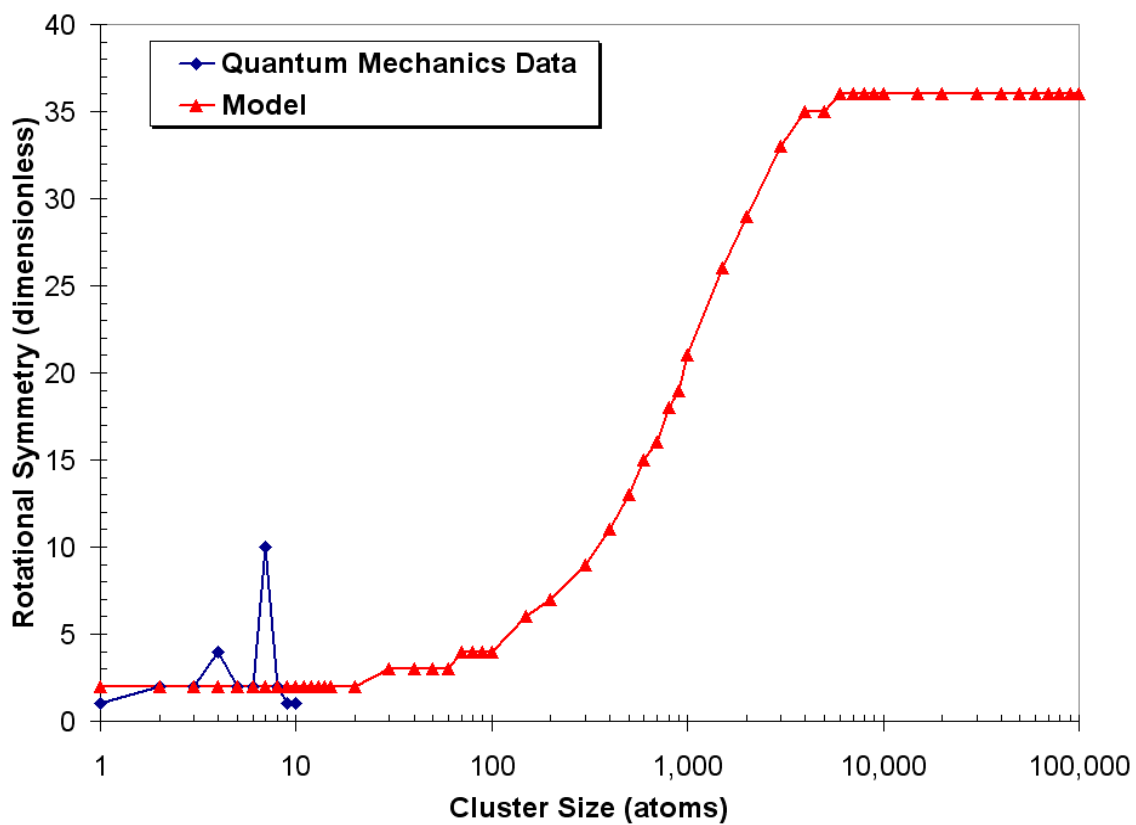
Figure 2.3: Silicon cluster rotational symmetry as a function of its size. The rotational symmetry of the Si solid crystal is 36. The quantum mechanics data for small clusters are calculated by the GAMESS[Sch63] program, while the solid triangles are for the fitted model.

cule has 4 3-fold rotational axes giving it a rotational symmetry number of 12. The methyl radical and the methane-methyl transition state only has one 3-fold rotational axis, due to the stretching and breaking of one of the C-H bonds, giving it a rotational symmetry number of 3. From equations 2.46 and 2.47, it can be seen that the reactant rotational symmetry number is divided by the transition state rotational symmetry number as follows:

$$\sigma_{CH_4}/\sigma^{\ddagger}$$

which yields a quotient of four for the formation of the methyl radical from methane. This corresponds to the four hydrogen atoms, any one of which can participate in the reaction. Thus the four-fold degeneracy for this reaction is accounted for by the rotational symmetry numbers.

Taking the reverse reaction, the recombination of a hydrogen atom with a methyl radical yields the following:

$$\sigma_{CH_3}/\sigma^{\ddagger}$$

where

σ_{CH_3} is the rotational symmetry number for the methyl radical

$\sigma^{\ddagger}$ is the rotational symmetry number for the transition state

where the rotational symmetry number is three for both species giving a quotient of one, corresponding to the single path for this recombination reaction.

We now turn our attention back to clustering reactions. For small size clusters, no modifications are necessary. The reaction degeneracy is properly taken into account by the rotational symmetries. For large size clusters however, the
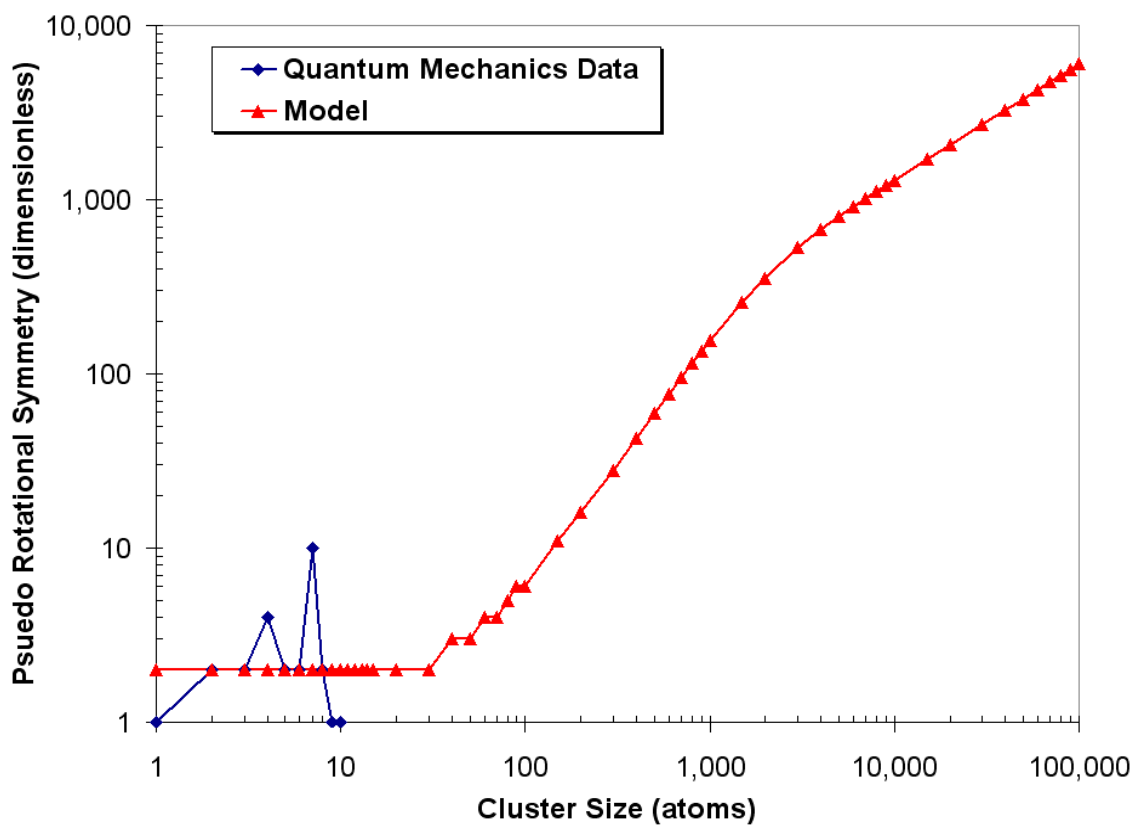
Figure 2.4: Silicon Pseudo Rotational Symmetry

maximum rotational symmetry is 36 for crystalline silicon. This would imply that the maximum number of sites available for monomer evaporation from a large size cluster would be 36. But this seems unreasonable since all surface atoms are essentially the same. Therefore, a correction is needed to account for the expected increased degeneracy. This is done by incorporating equation 4.10 into equation 2.69 yielding the following pseudo rotational symmetry numbers (see Figure 2.4).

2.3.3.5 Collision Cross-Section

Finally, the collision cross-section between the excited cluster Si_{i+j}^*,and the bath gas M, is needed to determine the de-energization rate constant k_2. The hard sphere model is used where the radius of the cluster is given by

$$r_{i+j} = \sqrt[3]{\frac{3\Omega}{4\pi}(i+j)} \tag{2.70}$$

where Ω is the atomic volume, and the radius of the bath gas M is obtained from the literature[Row94].

CHAPTER 3

Nano-cluster Nucleation Model

3.1 Introduction

In the previous section, we developed expressions for the rate constants, which describe the individual reactions that occur during nucleation. In this section, we will develop a set of coupled equations describing the overall nucleation process. This set of equations is commonly referred to as the master equations. Further, we will develop two different reactor models, which represent two bounding conditions for non-equilibrium gas phase nano-cluster nucleation. These are the one-dimensional kinetics model (ODK) which describes plug flow gas reactors, and the well-stirred reactor model which describes an ideal tank reactor. In practice, most reactors can be sufficiently described by plug flow reactors, well-stirred reactors, or combinations of both. For instance, a plug flow reactor can be modeled as one to several well-stirred reactors in series. The greater the number of well-stirred reactors, the better the approximation[HA79]. Additionally, due to the large number of coupled differential equations involved for describing nucleation of even modest-size nanoparticles (D_p on the order of 10 nm - a 10 nm silicon particle contains 7×10^5 atoms), two approximation techniques will be developed which greatly reduce the number of equations. These are the discrete sectional method and the method of moments.

3.2   Master Equations

In order to determine the nucleation behavior in a nozzle or well-stirred reactor, the rate of change of cluster size due to recombination and dissociation is needed. The equations describing this phenomenon are commonly referred to as the master equations. Once the master equations have been developed, they can be coupled to the fluid dynamic equations developed in a later section, section 3.3.

The time rate of change of the concentration of clusters of size i atoms due to recombination and dissociation is

$$
\begin{aligned}
dC_i/dt \;=\; & \tfrac{1}{2} \sum_{j=1}^{i-1} \left[K_{rec}\left(j, i-j\right) C_j C_{i-j} - \left(1 - \delta_{j,i-j}\right) K_{diss}\left(j, i-j\right) C_i \right] \\
& + \sum_{j=1}^{\infty} \left[\left(1 + \delta_{i,j}\right) K_{diss}\left(i, j\right) C_{i+j} - K_{rec}\left(i, j\right) C_i C_j \right] + S_i \qquad (3.1)
\end{aligned}
$$

where

C_i is the concentration of cluster size i

S_i is the source term of cluster size i

$K_{rec}(j, i-j)$ is the rate constant for the formation of cluster size i from smaller size clusters of size j and $i-j$

$K_{diss}(j, i-j)$ is the rate constant for the destruction of cluster size i into smaller clusters of size j and $i-j$

$K_{diss}(i, j)$ is the rate constant for the formation of cluster size i from the destruction of larger clusters of size $i+j$

$K_{rec}(i, j)$ is the rate constant for the destruction of cluster size i due to recombination with other clusters

The master equations, just developed, form an infinite set of equations which cannot be solved easily. Several approximation methods have been developed to solve such a set of equations. The simplest of these is to truncate the set of equations at some arbitrary upper cluster size limit. This method has the disadvantage of only allowing the study of very small clusters, on the order of 1 to 3 nanometers in size. In order to study the formation and nucleation of larger size clusters, other methods must be employed. Two methods which have had success in other studies will be developed later in this section. These are the discrete sectional method and the method of moments, or moments method.

3.3 One-Dimensional-Kinetics (ODK)

In order to model clustering in flowing systems such as nozzles, the master equations must be coupled to the fluid dynamic equations. Using the control surface shown in figure 3.1, the one-dimension-kinetics (ODK) equations are developed

in the following subsections.
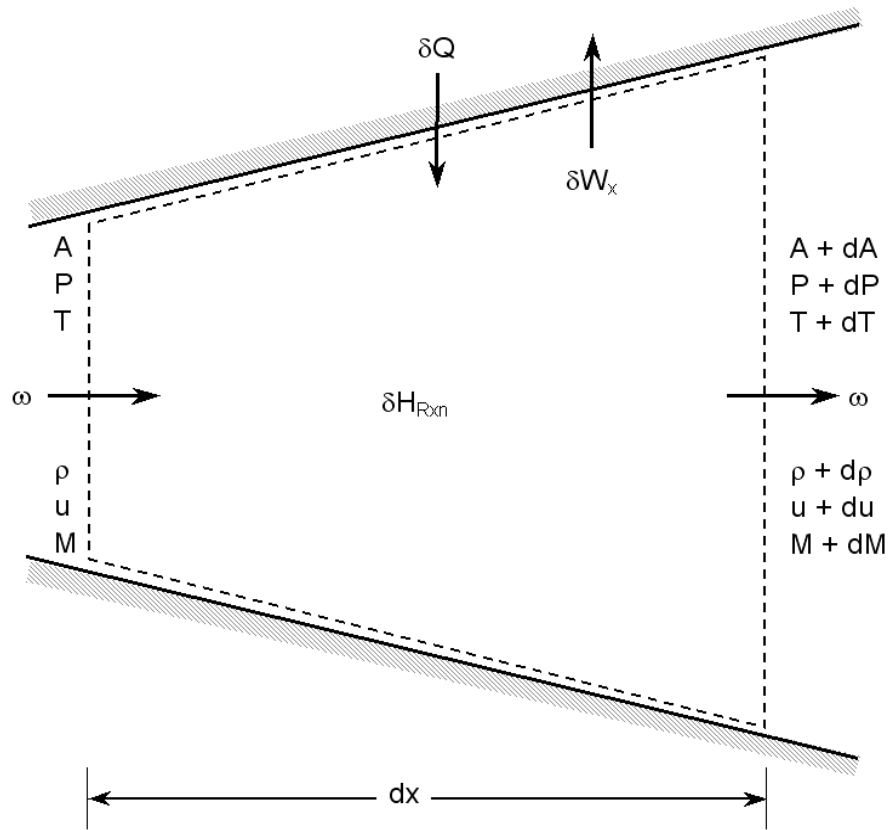
Figure 3.1: One-Dimensional-Kinetics (ODK) Control Surface

3.3.1   Equation of State

The equation of state for an ideal gas is

$$P = \frac{\rho \Re T}{W} \tag{3.2}$$

where

P is pressure

ρ is the gas density

$\mathfrak{R}$ is the universal gas constant

T is temperature

W is molecular weight

Taking logarithms and differentiating gives

$$dP/P = d\rho/\rho + \frac{dT}{T} - dW/W \tag{3.3}$$

3.3.2   Speed of Sound

The speed of sound is given as

$$c^2 = \frac{\gamma \mathfrak{R} T}{W} \tag{3.4}$$

or

$$dc/c = \tfrac{1}{2}\left(d\gamma/\gamma + dT/T - dW/W\right) \tag{3.5}$$

where

c is the speed of sound

γ is the ratio of specific heats, C_p/C_v

3.3.3 Mach Number

The definition of the Mach number is

$$M^2 = u^2 \big/ c^2 = \frac{u^2 W}{\gamma \Re T} \tag{3.6}$$

or

$$dM^2 \big/ M^2 = du^2 \big/ u^2 + dW \big/ W - d\gamma \big/ \gamma - dT \big/ T \tag{3.7}$$

where

$$M \quad \text{is the Mach number}$$

$$u \quad \text{is the gas velocity}$$

3.3.4 Conservation of Mass

In one dimension, the conservation of mass is

$$\frac{\partial}{\partial t}(\rho A \Delta x) = \rho u A\big|_x - \rho u A\big|_{x+\Delta x} \tag{3.8}$$

Dividing by Δx and taking the limit as Δx approaches zero gives

$$\frac{\partial}{\partial t}(\rho A) = -\frac{\partial}{\partial x}(\rho u A) \tag{3.9}$$

Finally, factoring and dividing both sides by $\rho u A$ gives

$$\frac{1}{u\rho}\frac{\partial \rho}{\partial t} = -\frac{1}{\rho}\frac{\partial \rho}{\partial x} - \frac{1}{u}\frac{\partial u}{\partial x} - \frac{1}{A}\frac{\partial A}{\partial x} \tag{3.10}$$

3.3.5 Conservation of Species

In addition to conservation of total mass, each species must be conserved. The
conservation equation for each species is

$$\frac{\partial}{\partial t}\left(y_i \rho A \Delta x\right) = y_i \rho u A\big|_x - y_i \rho u A\big|_{x+\Delta x} + A\Delta x \omega_i \tag{3.11}$$

where

$\qquad y_i \quad$ is the mass fraction of species i

$\qquad \omega_i \quad$ is the mass generation/consumption rate for species i

Dividing by $A\Delta x$ and taking the limit as Δx approaches zero gives

$$\frac{\partial}{\partial t}\left(y_i \rho\right) = -\frac{1}{A}\frac{\partial}{\partial x}\left(y_i \rho u A\right) + \omega_i \tag{3.12}$$

Differentiating and subtracting out the continuity equation (equation 3.10) gives

$$\frac{1}{u}\frac{\partial y_i}{\partial t} = -\frac{\partial y_i}{\partial x} + \omega_i\big/_{\rho u} \tag{3.13}$$

Noting that $\omega_i/_{W_i} = \tilde{\omega}_i$, equation 3.12 becomes

$$\frac{1}{u}\frac{\partial y_i}{\partial t} = -\frac{\partial y_i}{\partial x} + W_i\tilde{\omega}_i\big/_{\rho u} \tag{3.14}$$

where

$\qquad \tilde{\omega}_i \quad$ is the mole generation/consumption rate for species i

3.3.6 Conservation of Momentum

In one dimension, the conservation of momentum equation is

$$\frac{\partial}{\partial t}\left(\rho A \Delta x u\right) = \left. PA\right|_x - \left. PA\right|_{x+\Delta x} + \left. \rho u^2 A\right|_x - \left. \rho u^2 A\right|_{x+\Delta x} - 4fA\left(\Delta x/D\right)\frac{\rho u^2}{2} \quad (3.15)$$

where f is the friction factor. Again, dividing by Δx and taking the limit as Δx approaches zero gives

$$\frac{\partial}{\partial t}\left(\rho A u\right) = -\frac{\partial}{\partial x}\left(PA\right) - \frac{\partial}{\partial x}\left(\rho u^2 A\right) - 4fA\left(1/D\right)\frac{\rho u^2}{2} \quad (3.16)$$

Factoring gives

$$u\frac{\partial}{\partial t}\left(\rho A\right) + \rho A\frac{\partial u}{\partial t} = -\frac{\partial}{\partial x}\left(PA\right) - u\frac{\partial}{\partial x}\left(\rho u A\right) - \rho u A\frac{\partial u}{\partial x} - 4fA\left(1/D\right)\frac{\rho u^2}{2} \quad (3.17)$$

Subtracting out the equation of continuity (3.9) multiplied by the velocity, u gives

$$\rho A\frac{\partial u}{\partial t} = -\frac{\partial}{\partial x}\left(PA\right) - \rho u A\frac{\partial u}{\partial x} - 4fA\left(1/D\right)\frac{\rho u^2}{2} \quad (3.18)$$

Rearranging equation 3.18 and noting that $\rho u^2 = \gamma P M^2$ gives

$$\frac{1}{u^2}\frac{\partial u}{\partial t} = -\frac{1}{\gamma M^2}\frac{1}{P}\frac{\partial P}{\partial x} - \frac{1}{\gamma M^2}\frac{1}{A}\frac{\partial A}{\partial x} - \frac{1}{u}\frac{\partial u}{\partial x} - 2f\left(1/D\right) \quad (3.19)$$

3.3.7 Conservation of Energy

The conservation of energy equation can be stated as

$$\frac{\partial}{\partial t}\left\{\rho A \Delta x\left(h + u^2/2\right)\right\} = \left. \rho u A\left(h + u^2/2\right)\right|_x - \left. \rho u A\left(h + u^2/2\right)\right|_{x+\Delta x} \quad (3.20)$$

44

$$+ \quad \rho A \Delta x \left(\delta Q + \delta W_x + \delta H_{Rxn} \right)$$

where

h	is enthalpy
δQ	is heat added by external sources
δW_x	is work delivered to external sources
δH_{Rxn}	is heat added due to chemical reaction

Taking the limit as Δx approaches zero, subtracting out the continuity equation and rearrangement gives

$$\frac{1}{u} \frac{\partial}{\partial t} \left(h + \frac{u^2}{2} \right) = -\frac{\partial}{\partial x} \left(h + \frac{u^2}{2} \right) + \frac{1}{u} \left(\delta Q + \delta W_x + \delta H_{Rxn} \right) \qquad (3.21)$$

noting that $dh = C_p dT$, dividing through by $C_p T$ and rearrangement gives

$$\frac{1}{u} \frac{1}{T} \frac{\partial T}{\partial t} + \frac{1}{u} \frac{\gamma - 1}{2} M^2 \frac{1}{u^2} \frac{\partial u^2}{\partial t} = -\frac{1}{T} \frac{\partial T}{\partial x} - \frac{\gamma - 1}{2} M^2 \frac{1}{u^2} \frac{\partial u^2}{\partial x} + \frac{1}{u} \frac{\left(\delta Q + \delta W_x + \delta H_{Rxn} \right)}{C_p T}$$
$$(3.22)$$

3.3.8   Enthalpy, Molecular Weight and Ratio of Specific Heats

In addition to the conservation equations, we need to know how the enthalpy, molecular weight and specific heat ratio change as gas expands and the reactions progress through the nozzle. These are:

$$dh/dt = 1/\rho \sum W_i h_i \, dC_i/dt \qquad (3.23)$$

$$\frac{1}{W} dW/dt = -\frac{W}{\rho} \sum dC_i/dt \qquad (3.24)$$

$$\frac{d\gamma}{\gamma} = \frac{dc_p}{c_p} - \frac{dc_v}{c_v} \qquad (3.25)$$

where

$$dc_p/dt = \frac{1}{\rho} \sum W_i c_{p_i} dC_i/dt$$

and

$$dc_v/dt = \frac{1}{\rho} \sum W_i c_{v_i} dC_i/dt$$

3.3.9 Influence Coefficients

At steady state conditions, equations 3.3, 3.5, 3.7, 3.10, 3.19, 3.22, 3.23, 3.24, and 3.25 form a coupled set of differential equations that can be rearranged to form a desired set of dependent and independent variables. If the temperature is known as a function of T, such as for a constant quench rate, the following equations, presented in table 3.1, result. This type of table is referred to as an influence coefficient table[Sha53], because the dependent variables listed at the head of each row are influenced by the independent variables at the head of each column by an amount determined by the coefficients found at the column, row junctures.

3.4 Well Stirred Reactor Theory

The material balance for a well stirred reactor is

$$\rho V dy_i/dt = y_i|_{in} u\rho A - y_i u\rho A + R_i \qquad (3.26)$$

where

Table 3.1: Influence Coefficient Matrix

	$\frac{1}{T}dT/dt$	$\frac{1}{C_P T}\left(dQ/dt + dh/dt\right)$	$4f\frac{u}{D}$	$\frac{1}{W}dW/dt$	$\frac{1}{\gamma}d\gamma/dt$
$\frac{1}{M^2}dM^2/dt$	$-\frac{2\left(1+\frac{\gamma-1}{2}M^2\right)}{(\gamma-1)M^2}$	$\frac{2}{(\gamma-1)M^2}$	0	1	-1
$\frac{1}{c}dc/dt$	$1/2$	0	0	$-1/2$	$1/2$
$\frac{1}{P}dP/dt$	$\frac{\gamma}{\gamma-1}$	$-\frac{\gamma}{\gamma-1}$	$-\frac{\gamma M^2}{2}$	0	0
$\frac{1}{\rho}d\rho/dt$	$\frac{1}{\gamma-1}$	$\frac{\gamma}{\gamma-1}$	$-\frac{\gamma M^2}{2}$	-1	0

ρ is the density

V is the control volume

y_i is the mass fraction of cluster size i

$y_i|_{in}$ is the mass fraction of cluster size i in the inlet stream

u is velocity

A is cross-sectional area

and

$$R_i = V W_i \left. dC_i/dt \right|_{nucleation} \tag{3.27}$$

where

R_i is the mass rate of change of cluster size i due to nucleation

W_i is the molecular weight of cluster size i

$\left. dC_i/dt \right|_{nucleation}$ is the rate of change of concentration of cluster size i due to nucleation

Equation 3.26 can be rearranged to give the rate of change of the concentration

of cluster size i as follows:

$$VW_i \frac{dC_i}{dt} = uAW_i \left(C_i|_{in} - C_i \right) + VW_i \left. \frac{dC_i}{dt} \right|_{nucleation}$$

$$\frac{dC_i}{dt} = \frac{uA}{V} \left(C_i|_{in} - C_i \right) + \left. \frac{dC_i}{dt} \right|_{nucleation} \tag{3.28}$$

For steady state conditions, and taking note that $\frac{V}{uA}$ is the characteristic time constant, τ, upon rearrangement, equation 3.28 becomes

$$C_i = C_i|_{in} + \tau \left. \frac{dC_i}{dt} \right|_{nucleation} \tag{3.29}$$

which is the steady state solution for the concentration of cluster size i.

3.5 Discrete Sectional Method

The discrete sectional method tackles the problem of the large size domain by dividing the domain up into sections. Each section consists of a large portion of the size domain. All particles in a section take on the sectional average properties. This greatly reduces the number of conservation equations. Typically, the size domain is divided into several (10 - 30) equal logarithmic sections. Development of the discrete sectional method is as follows.

Multiplying equation 3.1 by i^k and summing over all i, gives[VG92, Dra72]

$$\begin{aligned} \frac{dN_k}{dt} &= \frac{1}{2} \sum_{i=1}^{\infty} \sum_{j=1}^{\infty} \left[K_{rec}(i,j) C_i C_j - (1 + \delta_{i,j}) K_d(i,j) C_{i+j} \right] \\ &\quad \times \left[(i+j)^k - i^k - j^k \right] + \sum_{i=1}^{\infty} i^k S_i \end{aligned} \tag{3.30}$$

where the moments of the cluster size distribution are defined as

$$N_k(t) = \sum_{i=1}^{\infty} i^k C_i(t) \tag{3.31}$$

For $k = 1$, equation 3.31 becomes

$$
\begin{aligned}
dN_1/dt &= \frac{1}{2} \sum_{i=1}^{\infty} \sum_{j=1}^{\infty} [K_{rec}(i,j)\, C_i C_j - (1 + \delta_{i,j})\, K_d(i,j)\, C_{i+j}] \times [(i+j) - i - j] \\
&+ \sum_{i=1}^{\infty} i S_i \tag{3.32}
\end{aligned}
$$

which is a conservation equation for the number of monomers in the system. The flux of monomers, Q, into section l due to recombination reactions is

$$\frac{1}{2} \sum_{i=1}^{k_l} \sum_{j=1}^{k_l} \theta(k_l < i + j \leq k_{l+1})\, (i+j)\, K_{rec}(i,j)\, C_i C_j$$

$$\frac{1}{2} \sum_{i=1}^{k_l} \sum_{j=k_l+1-i}^{\min(k_{l+1}-i,k_l)} (i+j)\, K_{rec}(i,j)\, C_i C_j$$

$$Q_{m+n \rightarrow l} = \frac{1}{2} \sum_{i=\max[(k_l+1-k_{n+1}),(k_m+1)]}^{\min\{[k_{l+1}-(k_n+1)],k_m+1\}} \sum_{j=\max(k_n+1,k_l+1-i)}^{\min(k_{n+1},k_{l+1}-i)} (i+j)\, K_{rec}(i,j)\, C_i C_j \tag{3.33}$$

The flux of monomers, Q, out of section l due to recombination reactions of particles in section l with those in lower sections is

$$- \sum_{i=1}^{k_l} \sum_{j=k_l+1}^{k_{l+1}} \theta(i + j > k_{l+1})\, j K_{rec}(i,j)\, C_i C_j$$

$$Q_{m+l \rightarrow n} = - \sum_{i=\max[(k_n+1-k_{l+1}),(k_m+1)]}^{\min\{[k_{n+1}-(k_l+1)],k_m+1\}} \sum_{j=\max(k_l+1,k_n+1-i)}^{\min(k_{l+1},k_{n+1}-i)} j K_{rec}(i,j)\, C_i C_j \tag{3.34}$$

The flux of monomers, Q, into section l due to recombination of particles in section l with particles in lower sections is

$$\sum_{i=1}^{k_l} \sum_{j=k_l+1}^{k_{l+1}} \theta \left(i+j \leq k_{l+1}\right) i K_{rec}\left(i,j\right) C_i C_j$$

$$Q_{m+l \to l} = \sum_{i=k_m+1}^{\min\{[k_{l+1}-(k_l+1)],k_{m+1}\}} \sum_{j=k_l+1}^{k_{l+1}-i} i K_{rec}\left(i,j\right) C_i C_j \tag{3.35}$$

The flux of monomers, Q, leaving section l due to recombination of particles in section l is

$$-\tfrac{1}{2} \sum_{i=k_l+1}^{k_{l+1}} \sum_{j=k_l+1}^{k_{l+1}} \theta \left(i+j > k_{l+1}\right) \left(i+j\right) K_{rec}\left(i,j\right) C_i C_j$$

$$Q_{l+l \to n} = -\tfrac{1}{2} \sum_{i=\max[(k_n+1-k_{l+1}),(k_l+1)]}^{\min\{[k_{n+1}-(k_l+1)],k_{l+1}\}} \sum_{j=\max(k_l+1,k_n+1-i)}^{\min(k_{l+1},k_{n+1}-i)} \left(i+j\right) K_{rec}\left(i,j\right) C_i C_j$$
$$\tag{3.36}$$

Finally, the flux of monomers, Q, leaving section l due to recombination of particles in section l with particles in higher sections is

$$-\sum_{i=k_l+1}^{k_{l+1}} \sum_{j=k_{l+1}+1}^{k_{\max}} i K_{rec}\left(i,j\right) C_i C_j$$

$$Q_{l+m \to n} = -\sum_{i=(k_l+1)}^{\min\{[k_{n+1}-(k_m+1)],k_{l+1}\}} \sum_{j=\max(k_m+1,k_n+1-i)}^{\min(k_{m+1},k_{n+1}-i)} i K_{rec}\left(i,j\right) C_i C_j \tag{3.37}$$

Collecting terms and defining $\dot{Q}_l$ as

$$\dot{Q}_l = \left[\left(Q_{m+n \to l} + Q_{m+l \to l}\right) - \left(Q_{m+l \to n} + Q_{l+l \to n} + Q_{l+m \to n}\right)\right]$$

The conservation of monomers as expressed by the discrete sectional method becomes

$$dQ_l/dt = \dot{Q}_l + \sum_{i=k_{l-1}+1}^{k_l} iS_i \qquad (3.38)$$

To express dQ_l/dt in terms of Q_l, so as to obtain a closed set of equations for Q_l, it is necessary to introduce the fundamental approximation inherent in the discrete sectional method. A convenient functional form of the size distribution within the sections must be introduced such that the integral quantity of monomers within the section is equal to Q_l[Gel80]. The simplest functional form is to assume that iC_i is constant within the section. Thus

$$Q_l = \sum_{k_l}^{k_{l+1}-1} iC_i \qquad (3.39)$$

Defining

$$q_l = iC_i$$

Equation 3.39 becomes

$$Q_l = q_l \left(k_{l+1} - k_l \right) \qquad (3.40)$$

Rearrangement then gives

$$C_i = \frac{Q_l}{i \left(k_{l+1} - k_l \right)} \qquad (3.41)$$

Equation 3.41 can then be substituted into equations 3.33, 3.34, 3.35, 3.36, 3.37 yielding the conservation equation of Q in closed form.

3.6 Moments Method

The next approximation method for solving the master equations for the size distribution is the method of moments, or moments method. Starting with the master equations, equation 3.1, and the definition of the moments of the size distribution, equations 3.30, and 3.31, we begin by dividing the cluster size domain into two groups: those smaller than x^*, and those larger than x^*. The quantity x^* is some small integer, usually arbitrarily chosen, but may be suggested, in some cases, by physical properties of the clusters (e.g. their stability). Those clusters sizes smaller than x^* are modeled discretely, and those larger than x^* are modeled as a continuum. For the small size clusters, (i.e. $< x^*$) equation 3.1 becomes

$$
\begin{aligned}
dC_i/dt \;=\; & \tfrac{1}{2}\sum_{j=1}^{i-1}\left[K_{rec}\left(j,i-j\right)C_jC_{i-j}-\left(1+\delta_{j,i-j}\right)K_{diss}\left(j,i-j\right)C_i\right] \\[4pt]
& +\;\sum_{j=i+1}^{x*}\left(1+\delta_{i,j-i}\right)K_{diss}\left(i,j-i\right)C_j-\sum_{j=1}^{x*}K_{rec}\left(i,j\right)C_iC_j \qquad (3.42) \\[4pt]
& +\;\int_{x*}^{\infty}dx\,K_{diss}\left(i,x-i\right)C_x-\int_{x*}^{\infty}dx\,K_{rec}\left(i,x\right)C_iC_x+S_i
\end{aligned}
$$

And similarly, equation 3.30 becomes

$$
\begin{aligned}
dN_k/dt \;=\; & \tfrac{1}{2}\sum_{i=1}^{x*}\sum_{j=1}^{x*}\left[K_{rec}\left(i,j\right)C_iC_j\right]\times\left[(i+j)^k-i^k-j^k\right] \\[4pt]
& -\;\tfrac{1}{2}\sum_{j=2}^{x*}\sum_{i=1}^{j-1}\left[(1+\delta_{i,j-i})K_{diss}\left(i,j-i\right)C_j\right]\times\left[j^k-i^k-(j-i)^k\right] \\[4pt]
& +\;\sum_{i=1}^{x*}\int_{x*}^{\infty}dx\left[K_{rec}\left(i,x\right)C_iC_x\right]\times\left[(i+x)^k-i^k-x^k\right] \\[4pt]
& -\;\sum_{i=1}^{x*-1}\int_{x*}^{\infty}dx\left[K_{diss}\left(i,x-i\right)C_x\right]\times\left[x^k-i^k-(x-i)^k\right] \qquad (3.43)
\end{aligned}
$$

$$+ \quad \tfrac{1}{2} \int\limits_{x*}^{\infty} \int\limits_{x*}^{\infty} dx\,dy\, [K_{rec}(x,y)\,C_x C_y] \times \left[(x+y)^k - x^k - y^k\right]$$

$$- \quad \tfrac{1}{2} \int\limits_{x*}^{\infty} dx \int\limits_{x*}^{x} dy\, [K_{diss}(x,x-y)\,C_x] \times \left[x^k - y^k - (x-y)^k\right]$$

$$+ \quad \sum_{i=1}^{x*} i^k S_i + \int\limits_{x*}^{\infty} dx\, x^k S(x)$$

where N_k are the full moments of the size distribution. The moments of the large size cluster distribution are defined as

$$M_k(t) = \int\limits_{x*}^{\infty} dx\, x^k C(x,t) \tag{3.44}$$

which are related to the full moments approximately by

$$M_k = N_k - \sum_{i=1}^{x*} i^k C_i \tag{3.45}$$

Inserting this into equation 3.43 gives upon rearrangement

$$
\begin{aligned}
dM_k/dt \;=\; & -\sum_{i=1}^{x*} i^k dC_i/dt + \sum_{i=1}^{x*} i^k S_i + \int\limits_{x*}^{\infty} dx\, x^k S_x \\[2mm]
+ \; & \tfrac{1}{2} \sum_{i=1}^{x*} \sum_{j=1}^{x*} [K_{rec}(i,j)\,C_i C_j] \times \left[(i+j)^k - i^k - j^k\right] \\[2mm]
- \; & \tfrac{1}{2} \sum_{j=2}^{x*} \sum_{i=1}^{j-1} [(1+\delta_{i,j-i})\, K_{diss}(i,j-i)\,C_j] \times \left[j^k - i^k - (j-i)^k\right] \\[2mm]
+ \; & \sum_{i=1}^{x*} \int\limits_{x*}^{\infty} dx\, [K_{rec}(i,x)\,C_i C_x] \times \left[(i+x)^k - i^k - x^k\right] \qquad (3.46) \\[2mm]
- \; & \sum_{i=1}^{x*-1} \int\limits_{x*}^{\infty} dx\, [K_{diss}(i,x-i)\,C_x] \times \left[x^k - i^k - (x-i)^k\right] \\[2mm]
+ \; & \tfrac{1}{2} \int\limits_{x*}^{\infty} \int\limits_{x*}^{\infty} dx\,dy\, [K_{rec}(x,y)\,C_x C_y] \times \left[(x+y)^k - x^k - y^k\right]
\end{aligned}
$$

$$- \frac{1}{2} \int_{x*}^{\infty} dx \int_{x*}^{x} dy \left[K_{diss}\left(x, x-y\right) C_x \right] \times \left[x^k - y^k - \left(x-y\right)^k \right]$$

In general, a function of the sort

$$G = \int dx\, g\left(x\right) C\left(x\right) \tag{3.47}$$

can be expanded in terms of its moments. Expanding $g(x)$ in a Taylor series expansion gives

$$
\begin{aligned}
g\left(x\right) &= \sum_{n=0}^{\infty} \frac{1}{n!} g_{x_0}^{(n)} \left(x - x_0\right)^n \\
&= \sum_{n=0}^{\infty} \frac{1}{n!} g_{x_0}^{(n)} \sum_{\nu=0}^{n} \binom{n}{\nu} \left(-x_0\right)^{n-\nu} x^{\nu}
\end{aligned}
\tag{3.48}
$$

Inserting equation 3.48 into equation 3.47 yields

$$G = \sum_{n=0}^{\infty} \frac{1}{n!} g_{x_0}^{(n)} \sum_{\nu=0}^{n} \binom{n}{\nu} \left(-x_0\right)^{n-\nu} M_{\nu} \tag{3.49}$$

Inserting equation 3.49 into equation 3.42 gives

$$
\begin{aligned}
dC_i/dt &= \frac{1}{2} \sum_{j=1}^{i-1} \left[K_{rec}\left(j, i-j\right) C_j C_{i-j} - \left(1 + \delta_{j,i-j}\right) K_{diss}\left(j, i-j\right) C_i \right] \\
&+ \sum_{j=i+1}^{x*} \left(1 + \delta_{i,j-i}\right) K_{diss}\left(i, j-i\right) C_j - \sum_{j=1}^{x*} K_{rec}\left(i, j\right) C_i C_j \quad (3.50) \\
&+ \sum_{n=0}^{\infty} \frac{1}{n!} K_{diss}^{(n)}\left(i, \bar{x}\right) \sum_{\nu=0}^{n} \binom{n}{\nu} \left(-\bar{x}\right)^{n-\nu} \sum_{l=0}^{\nu} \binom{\nu}{l} \left(-i\right)^{\nu-l} M_l \\
&- C_i \sum_{n=0}^{\infty} \frac{1}{n!} K_{rec}^{(n)}\left(i, \bar{x}\right) \sum_{\nu=0}^{n} \binom{n}{\nu} \left(-\bar{x}\right)^{n-\nu} M_{\nu} + S_i
\end{aligned}
$$

Also, it is noted that

$$(x+y)^k - x^k - y^k = \sum_{l=1}^{k-1} \binom{k}{l} y^{k-l} x^l \qquad (3.51)$$

and

$$x^k - y^k - (x-y)^k = \sum_{l=1}^{k-1} \sum_{\lambda=0}^{l} \binom{k}{l} \binom{l}{\lambda} (-1)^{l-\lambda} y^{k-\lambda} x^{\lambda} \qquad (3.52)$$

For $k = 0$, the $(x+y)^k - x^k - y^k$ and the $x^k - y^k - (x-y)^k$ terms reduce to -1 and equation 3.46 becomes

$$
\begin{aligned}
dM_0/dt &= -\sum_{i=1}^{x*} dC_i/dt + \sum_{i=1}^{x*} S_i + \int_{x*}^{\infty} dx\, S_x \\
&\quad - \tfrac{1}{2} \sum_{i=1}^{x*} \sum_{j=1}^{x*} [K_{rec}(i,j)\, C_i C_j] + \tfrac{1}{2} \sum_{j=2}^{x*} \sum_{i=1}^{j-1} [(1+\delta_{i,j-i})\, K_{diss}(i,j-i)\, C_j] \\
&\quad - \sum_{i=1}^{x*} C_i \sum_{n=0}^{\infty} \frac{1}{n!} K_{rec}^{(n)}(i,\bar{x}) \sum_{\nu=0}^{n} \binom{n}{\nu} (-\bar{x})^{n-\nu} M_\nu \\
&\quad + \sum_{i=1}^{x*-1} \sum_{n=0}^{\infty} \frac{1}{n!} K_{diss}^{(n)}(i,\bar{x}) \sum_{\nu=0}^{n} \binom{n}{\nu} (-\bar{x})^{n-\nu} \sum_{l=0}^{\nu} \binom{\nu}{l} (-i)^{\nu-l} M_l \qquad (3.53) \\
&\quad - \tfrac{1}{2} \sum_{m=0}^{\infty} \sum_{n=0}^{\infty} \frac{1}{m!} \frac{1}{n!} K_{rec}^{(m,n)}(\bar{x},\bar{x}) \sum_{\mu=0}^{m} \sum_{\nu=0}^{n} \binom{m}{\mu} \binom{n}{\nu} (-\bar{x})^{m+n-\mu-\nu} M_\mu M_\nu \\
&\quad + \tfrac{1}{2} \left[\sum_{m=0}^{\infty} \sum_{n=0}^{\infty} \frac{1}{m!} \frac{1}{n!} K_{diss}^{(m,n)}(\bar{x},\bar{x}) \sum_{\mu=0}^{m} \sum_{\nu=0}^{n} \binom{m}{\mu} \binom{n}{\nu} \bar{x}^{m+n-\mu-\nu} \right. \\
&\quad \times \left. \left[\sum_{l=0}^{\nu} \binom{\nu}{l} \frac{(-1)^{m+n-\mu-l}}{\nu-l+1} \left[M_{\mu+\nu+1} - x*^{\nu-l+1} M_{\mu+l} \right] \right] \right]
\end{aligned}
$$

For $k = 1$, the $(x+y)^k - x^k - y^k$ and the $x^k - y^k - (x-y)^k$ terms reduce to 0 and equation 3.46 becomes

$$dM_1/dt = -\sum_{i=1}^{x*} i\, dC_i/dt + \sum_{i=1}^{x*} i S_i + \int_{x*}^{\infty} dx\, x S_x \qquad (3.54)$$

And for arbitrary k, equation 3.46 becomes

$$
\begin{aligned}
dM_k/dt &= -\sum_{i=1}^{x*} i^k\, dC_i/dt + \sum_{i=1}^{x*} S_i + \int_{x*}^{\infty} dx\, S_x \\
&+ \tfrac{1}{2}\sum_{i=1}^{x*}\sum_{j=1}^{x*} [K_{rec}(i,j)\, C_i C_j] \times \left[(i+j)^k - i^k - j^k\right] \\
&- \tfrac{1}{2}\sum_{j=2}^{x*}\sum_{i=1}^{j-1} [(1+\delta_{i,j-i})\, K_{diss}(i,j-i)\, C_j] \times \left[j^k - i^k - (j-i)^k\right] \\
&+ \sum_{i=1}^{x*} C_i \sum_{l=1}^{k-1} \binom{k}{l} i^{k-l} \sum_{n=0}^{\infty} \frac{1}{n!} K_{rec}^{(0,n)}(i,\bar{x}) \sum_{\nu=0}^{n} \binom{n}{\nu} (-\bar{x})^{n-\nu} M_{\nu+l} \\
&- \left[\sum_{i=1}^{x*-1}\sum_{l=1}^{k-1} \binom{k}{l} i^{k-l} \sum_{\lambda=0}^{l} \binom{l}{\lambda} (-i)^{l-\lambda} \sum_{n=0}^{\infty} \frac{1}{n!} K_{diss}^{(0,n)}(i,\bar{x})\right] \\
&\times \left[\sum_{\nu=0}^{n} \binom{n}{\nu} (-\bar{x})^{n-\nu} \sum_{\mu=0}^{\nu} \binom{\nu}{\mu} (-i)^{\nu-\mu} M_{\lambda+\mu}\right] \qquad (3.55) \\
&+ \left[\tfrac{1}{2}\sum_{l=1}^{k-1} \binom{k}{l} \sum_{m=0}^{\infty}\sum_{n=0}^{\infty} \frac{1}{m!}\frac{1}{n!} K_{rec}^{(m,n)}(\bar{x},\bar{x})\right] \\
&\times \left[\sum_{\mu=0}^{m}\sum_{\nu=0}^{n} \binom{m}{\mu}\binom{n}{\nu} (-\bar{x})^{m+n-\mu-\nu} M_{\mu+k-l} M_{\nu+l}\right] \\
&- \tfrac{1}{2}\left[\sum_{l=1}^{k-l}\sum_{\lambda=0}^{l} \binom{k}{l}\binom{l}{\lambda} \sum_{m=0}^{\infty}\sum_{n=0}^{\infty} \frac{1}{m!}\frac{1}{m!} K_{diss}^{(m,n)}(\bar{x},\bar{x})\right] \\
&\times \left[\sum_{\mu=0}^{m}\sum_{\nu=0}^{n} \binom{m}{\mu}\binom{n}{\nu} \bar{x}^{m+n-\mu-\nu}\right]
\end{aligned}
$$

56

$$\times \quad \left[\sum_{\varepsilon=0}^{\nu} (-1)^{l-\lambda+m+n-\mu-\varepsilon} \begin{pmatrix} \nu \\ \varepsilon \end{pmatrix} \frac{1}{k+\nu+1-\lambda-\varepsilon} \right]$$

$$\times \quad \left[\left(M_{k+\mu+\nu+1} - x *^{k+\nu+1-\lambda-\varepsilon} M_{\mu+\varepsilon+\lambda} \right) \right]$$

Equations 3.50 and 3.55 are two coupled sets of nonlinear ordinary differential equations for the small-size cluster concentrations and the continuum moments. If we take only the first two terms in the Taylor series expansion for K_{rec} and K_{diss} into account (i.e. we truncate all terms with m, $n > 2$), then the system is self-contained for any number of moments M_k, $k = 0, 1, ..., N$, with $N > 1$. Because the recombination and the dissociation rates are supposed to be smooth functions of size for the large-size clusters, this truncation is not considered to be too severe.

CHAPTER 4

Results and Comparison With Experiments

4.1 Cluster Energetics, Geometry, Vibrations, and Electron Densities

The energetics of silicon clusters of up to size 10 atoms and carbon clusters of up to size 10 atoms have been calculated. The calculations were performed using the General Atomic and Molecular Electronic Structure System (GAMESS) Quantum Mechanics software package[Sch63]. Calculations were performed using both ab initio and semi-empirical methods for silicon clusters, and the ab initio method only for carbon clusters. The basis sets used were the TZV[MC80] basis set for the ab initio calculations and the PM3[Ste89] basis set for the semi-empirical calculations. In this manner, the cluster binding energy, configuration, and normal modes of vibration were determined.

Figure 4.1 shows the cluster binding energy per atom for silicon clusters as a function of cluster size for both the ab initio and semi-empirical models, and Figure 4.2 is a similar curve for carbon clusters, but for ab initio calculations only. The data points are the calculated binding energies, and the smooth curves are the binding energies based on a modified capillary model. For silicon, the large differences in binding energies between the ab initio model and the semi-empirical model is due to the nature of the semi-empirical calculations, where the lack in rigor is augmented with empirical constants.
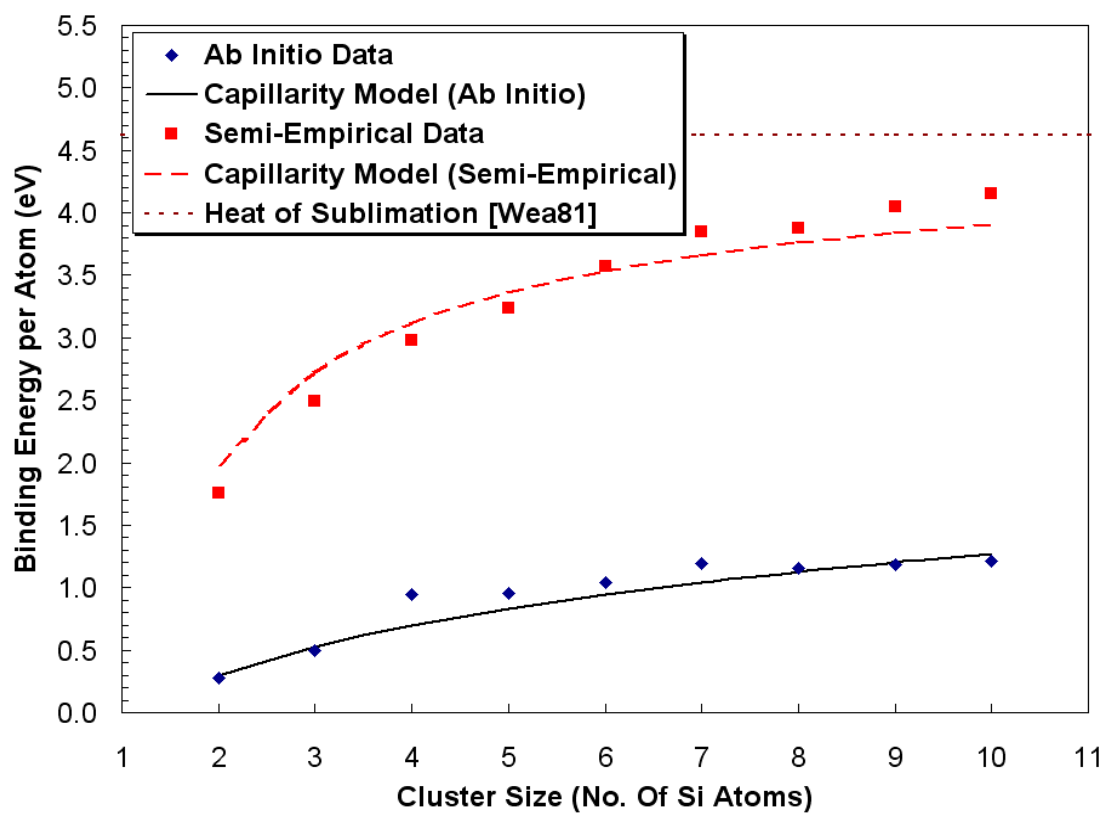
Figure 4.1: Binding energy per atom for Si as a function of the cluster size using the ab initio and the semi-empirical quantum methods. A capillary model is fitted to the data.
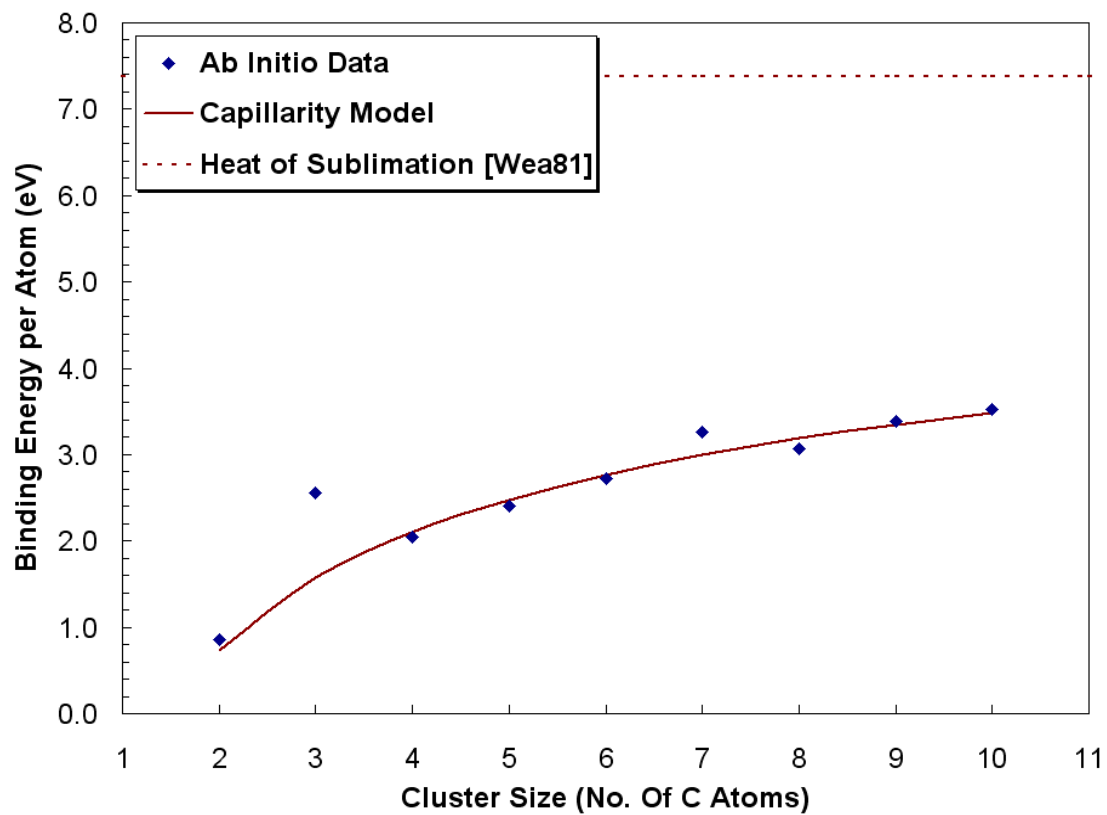
Figure 4.2: Binding energy per atom for C clusters as a function of the cluster size using the ab initio quantum method. A capillary model is fitted to the data.

The capillarity model is given as[LA78, SP98, Bur73]

$$E_{binding} = m\phi x \left(1 - ax^{-1/3}\right) \tag{4.1}$$

where

$\quad E_{binding}$ is the total cluster binding energy

$\quad m$ is the number of bonds per atom

$\quad \phi$ is the energy per bond

$\quad x$ is the number of atoms in the cluster

$\quad a$ is a surface energy parameter

which was modified by combining it to a power law as follows:

$$E_{binding} = m\phi \left(1 - x^{-\alpha}\right) x \left(1 - ax^{-1/3}\right) \tag{4.2}$$

where

$\quad \alpha$ is the power law coefficient

The crystalline structure for bulk silicon is the diamond structure[INS88]. Each atom within the bulk of the structure has four nearest neighbors (i.e. each bulk atom is bonded to four other atoms). Therefore, the number of bonds per atom, m, is two for this structure. Similarly, the crystalline structure for bulk carbon is the graphite structure. Each atom in this structure has three nearest neighbors. Thus the number of bonds per atom, m, in the hexagonal closed pack is 1.5. The energy per bond is related to the heat of sublimation at zero Kelvin by

$$\phi = \frac{\Delta H_{sublimation}}{m} \tag{4.3}$$

61

The surface energy parameter, a, was determined a priori from the bulk crystalline structure in the following manner: The cluster volume is given as

$$V = n\Omega \tag{4.4}$$

where

V is the cluster volume

n is the number of atoms in the cluster

Ω is the atomic volume

Assuming the cluster is spherical, the volume can also be given as

$$V = \tfrac{4}{3}\pi r^3 \tag{4.5}$$

where

r is the cluster radius

Equating the two volume equations, equations 4.4 and 4.5, the cluster radius can be determined as

$$r = \left(\frac{3n\Omega}{4\pi}\right)^{1/3} \tag{4.6}$$

The cluster surface area, S, can then be determined as

$$S = 4\pi \left(\frac{3n\Omega}{4\pi}\right)^{2/3} \tag{4.7}$$

For the diamond structure, the atomic volume, Ω, is given as

$$\Omega = \left(\tfrac{a_0}{2}\right)^3 \tag{4.8}$$

where

a_0 is the lattice constant (5.4305 Å for Silicon)

Assuming that the surface atoms cleave along the 1,1,1 plane, the surface density, ρ_S, becomes

$$\rho_S = \frac{1}{\sqrt{3}} \left(\frac{2}{a_0}\right)^2 \tag{4.9}$$

Multiplying equation 4.7 by equation 4.9 and using equation 4.8, the number of surface atoms, n_S, is

$$n_S = \frac{4\pi}{\sqrt{3}} \left(\frac{3}{4\pi}\right)^{2/3} n^{2/3} \tag{4.10}$$

Assuming that the average bond deficiency per surface atom is unity, the surface energy parameter, a, for silicon becomes

$$a = \frac{\pi}{\sqrt{3}} \left(\frac{3}{4\pi}\right)^{2/3} \tag{4.11}$$

For carbon, the graphite structure was assumed. The atomic volume, Ω, for this structure is

$$\Omega = \sqrt{3} \left(\frac{a_0}{2}\right)^2 \left(\frac{c_0}{2}\right) \tag{4.12}$$

where

a_0 is the hexagonal lattice constant (2.4612 Å for graphite)

c_0 is the distance between basal planes (6.7079 Å for graphite)

Assuming the surface cleaves at the basal planes, the number of surface atoms, n_S, is

$$n_S = (4\pi)^{1/3} \sqrt{3} \left(c_0/a_0\right)^{2/3} n^{2/3} \tag{4.13}$$

Assuming that each surface atom is deficient $3/7$ of a bond, the carbon surface energy parameter becomes

$$a = (4\pi)^{1/3} \frac{\sqrt{3}}{7} \left(c_0/a_0\right)^{2/3} \tag{4.14}$$

A heat of sublimation of 4.619 eV at 0 K[Wea81] was used to determine the bond energies of silicon clusters, and likewise, a heat of sublimation of 7.373 eV at 0 K[Wea81] was used to determine the bond energies of carbon clusters. For silicon, the power law coefficient, α, was determined to be 0.225682 by a least squares fit to the ab initio data. For carbon, and also for the silicon semi-empirical data, the power law coefficient vanished. Note how the ab initio calculations differ markedly from the semi-empirical calculations. The semi-empirical model predicts binding energies greater than those predicted by the ab initio method. This is due to the nature of the semi-empirical calculations, where the lack in rigor is augmented with empirical constants. It is plausible that these empirical constants may be adjusted to give better agreement with the ab initio calculations.

Additionally, the morphology, normal modes of vibration, and electron density were determined for clusters of up to size 10 silicon atoms and size 10 carbon atoms. The geometry of the silicon dimer (i.e. 2 atom cluster) through the silicon decamer (i.e. 10 atom cluster) are shown in appendix A, and the geometry of the carbon dimer through decamer are shown in appendix B. Although the bond distances differ somewhat, in general, the semi-empirical model predicts the same cluster geometry as the ab initio model. The normal modes of vibration were also determined for each of these clusters. These are shown in the tables in appendix A for the silicon clusters and the tables in appendix B for the carbon clusters.

Tables A-1 through A-9 contain predictions from both the semi-empirical model and the ab initio model for the silicon clusters. Semi-empirical calculations were not performed for the carbon clusters. As can be seen from these tables, the semi-empirical model predicts higher frequencies for each mode when compared to the ab initio model. As will be shown later, this is an important consideration when computing thermochemistry or reaction rates. Finally, plots of cluster electron density were developed using the Molden software package[SN00] for each of these clusters and are shown in appendices A and B.

4.2 Nano-Cluster Nucleation

In order to study the nano-cluster nucleation phenomena, the rate constants developed in section 2.3 were inserted into the master equations developed in section 3.2. These were coupled to the one dimensional kinetics (ODK) nozzle expansion equations (section 3.3) to study nucleation within a nozzle, and to the well-stirred reactor model (section 3.4)to study nucleation in a turbulent environment. Either the discrete sectional method (section 3.5) or the moments method (section 3.6) was used to solve the system of equations.

4.2.1 Expanding Nozzle Model

The developed model for cluster nucleation in expanding nozzle flow will now be tested by comparison with experimental data. An earlier experiment was performed at the University of Minnesota in which they produced nanophase silicon[Rao95]. The model was run against the conditions reported in reference [Rao95] and compared to their data. The experiment consisted of using a plasma arc to generate silicon monomers in hot argon at the nozzle entrance. The resul-

tant mixture was then quenched by expanding it through a nozzle. Experimental conditions are given in table 4.1. The discrete sectional method was used to solve the coupled ODK / Master Equations for the nozzle. The moments method was not used for this type of problem because it is ill-posed. This type of problem is ill-posed because the initial conditions for the unknown continuum distribution do not exist[Sto90]. The nozzle geometry is shown in figure 4.3, and the nozzle conditions are illustrated in figures 4.4 through 4.6. Temperature, pressure, velocity, and saturation ratio versus nozzle length are illustrated. The particle size evolution through the nozzle is illustrated in figure 4.7. This figure shows that, although some particle size distribution is starting to develop, nucleation and growth of larger size particles does not occur in the nozzle. This is supported by earlier models of the same experiment[Rao95, Wei94]. As can be seen in figures 4.4 through 4.6, the quench rate is sufficient to produce a rapid increase in saturation ratio (see figure 4.6), and the experimental evidence indicates that nucleation is occurring[Rao95]. There must be some other mechanism that is occurring to cause the nucleation. This will be discussed in the next section.

4.2.2   Well Stirred Reactor Model

The reason that nucleation does not occur in the nozzle is that the nucleation rate is so much slower than the nozzle velocity. This situation is very similar to combustion in a jet afterburner. If not for the flame holders, combustion would not occur in the supersonic section of a jet. The reason is that the velocity of the gas stream is greater than the flame speed of the combustion process. Hence, the combustion reaction is snuffed-out, similar to blowing out a candle. In order to promote combustion in high velocity streams, flame holders are inserted to stabilize the combustion process. A flame holder consists of either inserting a
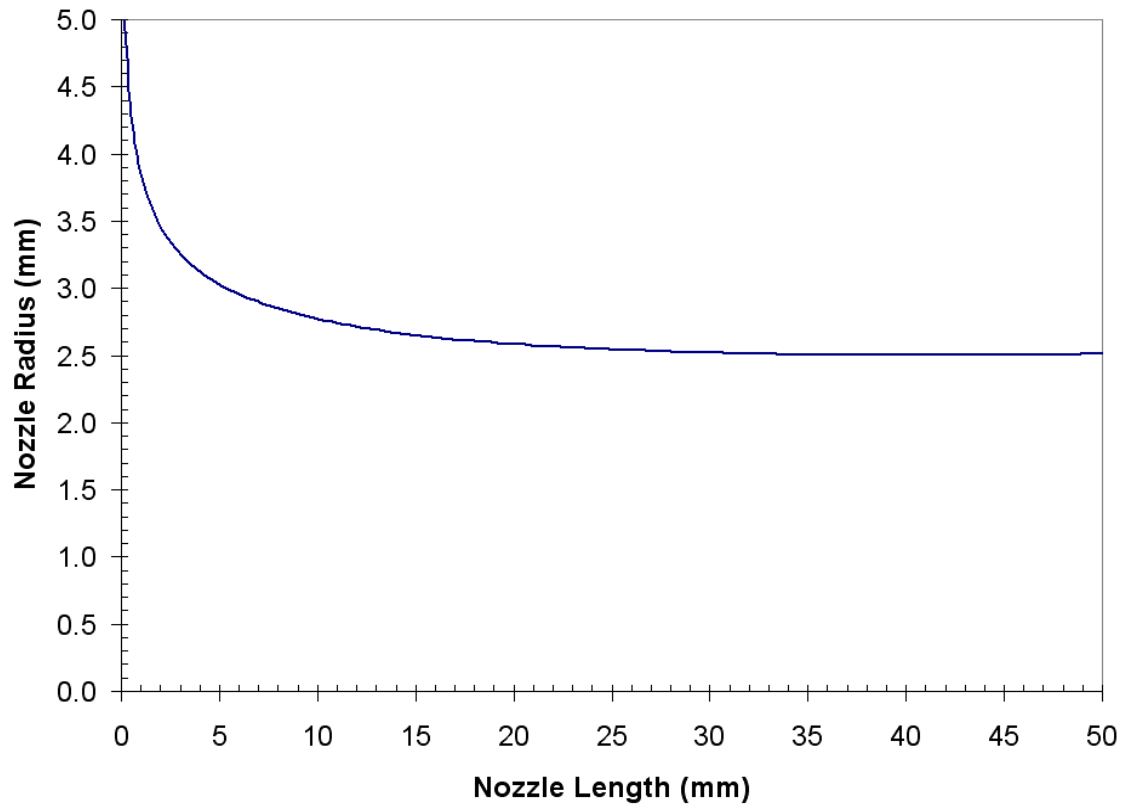
Figure 4.3: Nozzle Temperature and Pressure Profile
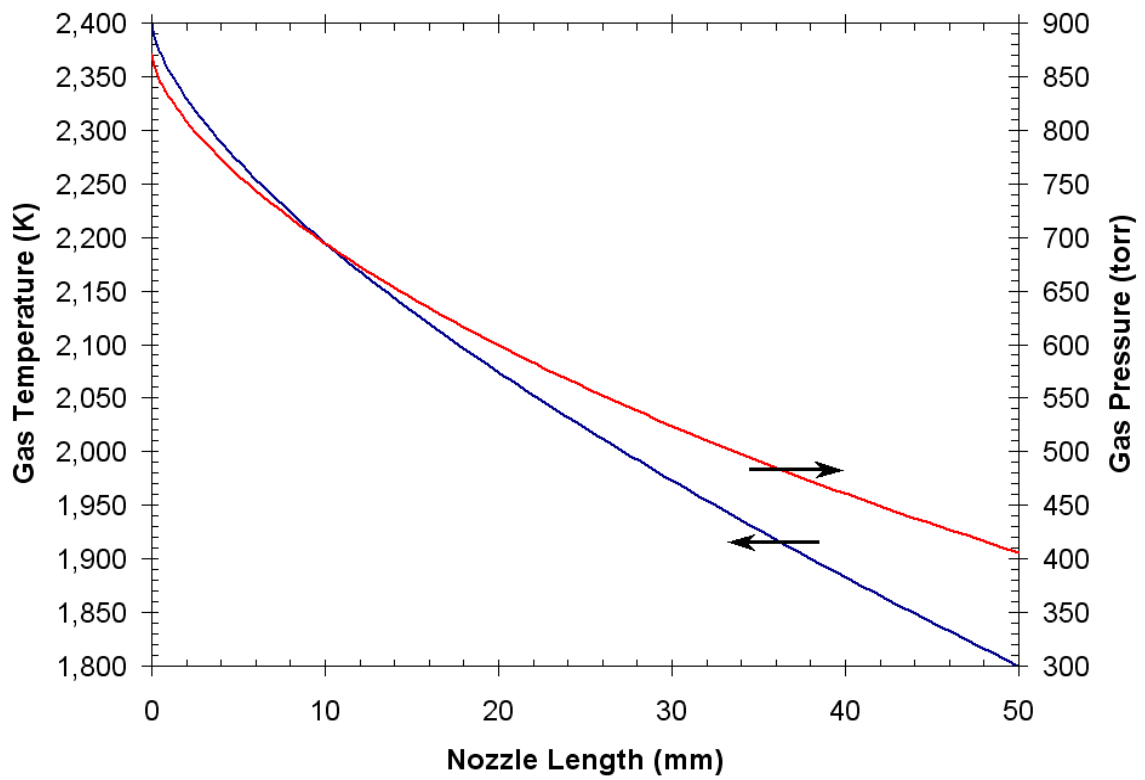
Figure 4.4: Nozzle Temperature and Pressure Profile
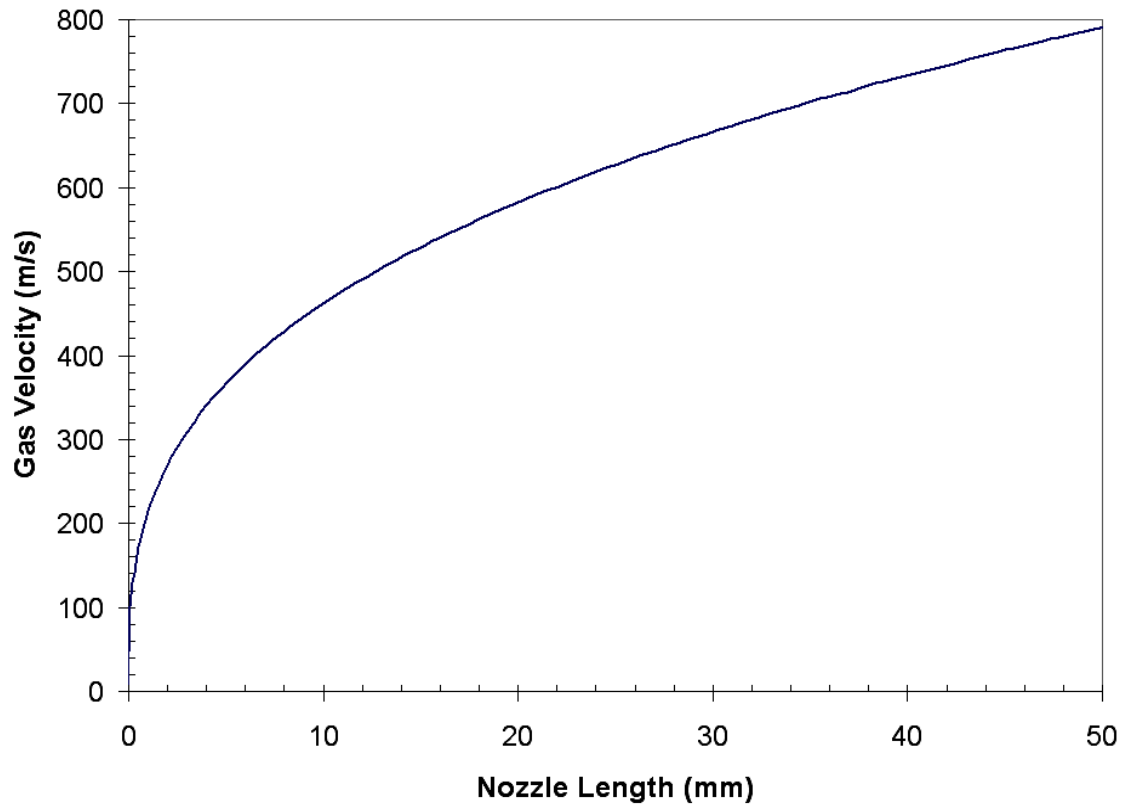
Figure 4.5: Nozzle Velocity Profile
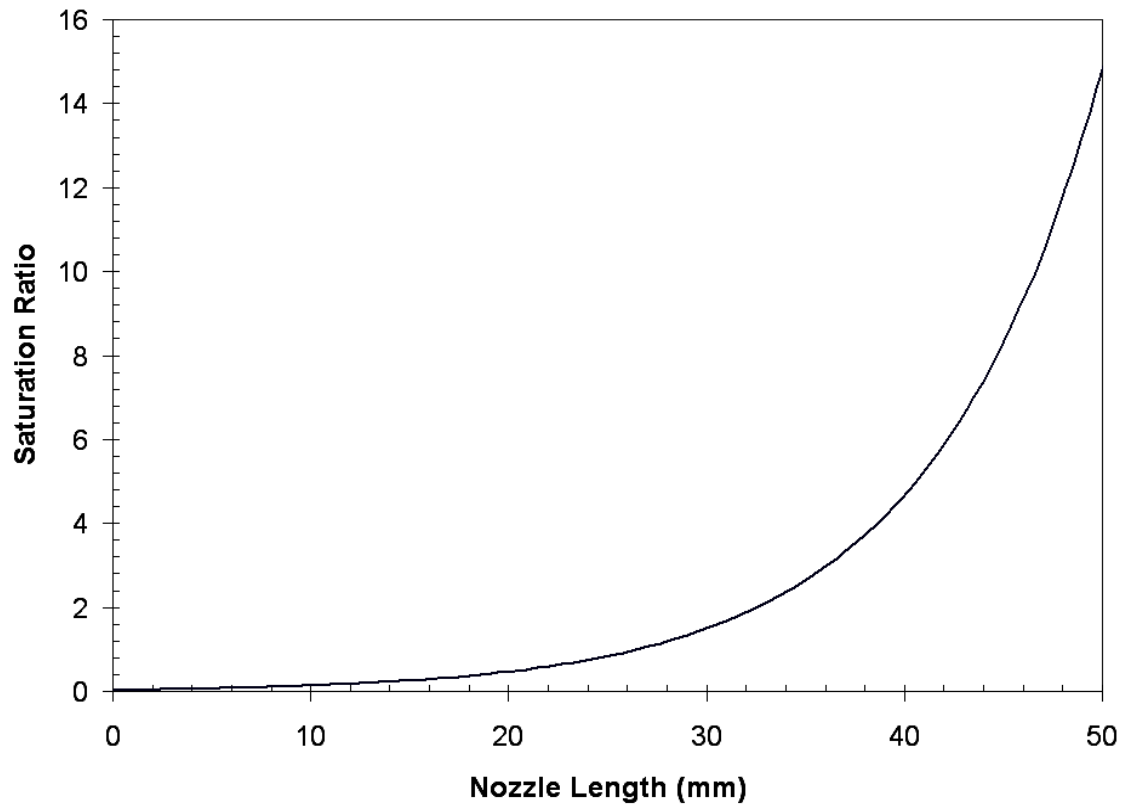
Figure 4.6: Nozzle Saturation Ratio Profile
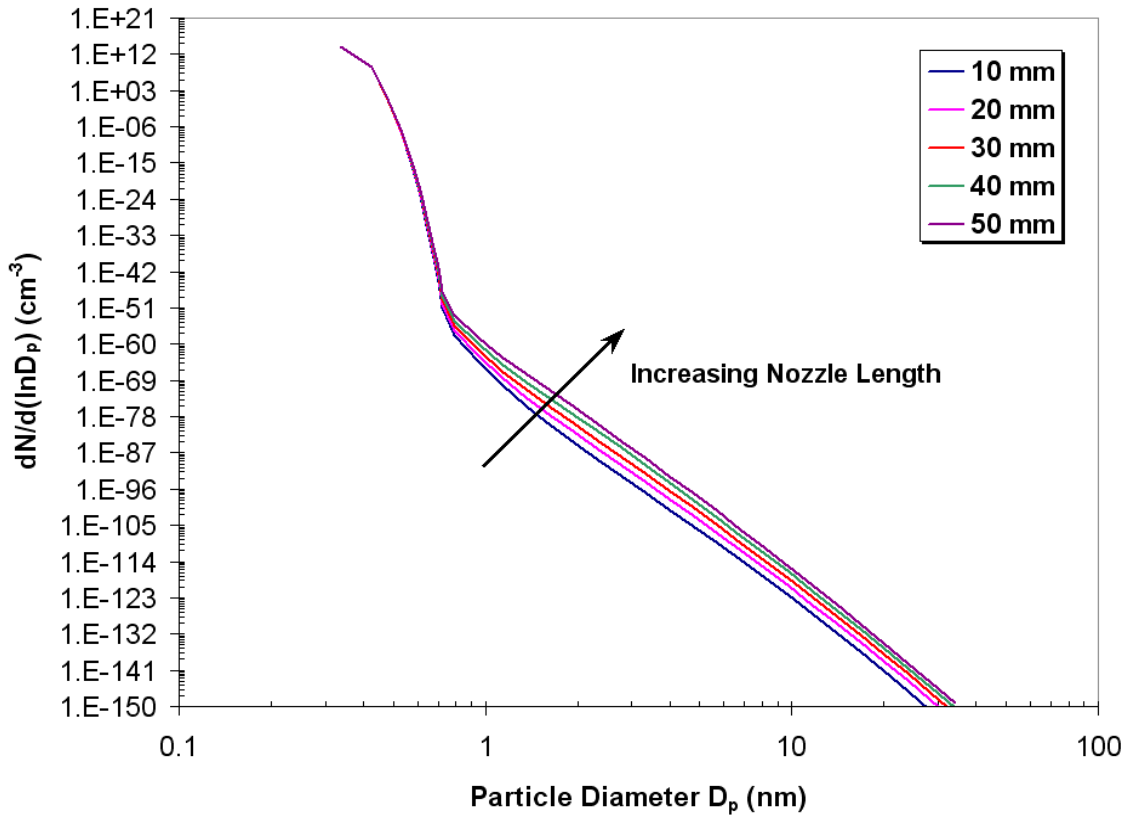
Figure 4.7: Particle Size Evolution Within Nozzle - Discrete Sectional Method

Table 4.1: Minnesota Experiment Conditions

	Inlet	Outlet
Diameter (mm)	–	5
Length (mm)	–	50
Pressure (torr)	871	405.6
Temperature (K)	2,400	1,800
N_{Si} (cm^{-3})	10^{14}	6.2×10^{13}
Saturation Ratio	0.024	15
Elapsed Time (μs)	–	95
Velocity (m/s)	–	790.8
Mach No.	–	1.0

bluff body in the flow stream or a sudden disruption of the flow stream such as a step or sudden expansion, wall recess, or by secondary gas injection as illustrated in figure 4.8. Flame holders promote strong recirculation zones which stabilize the combustion process. Experiments have shown that combustion is complete within the recirculation zones. The combustion products from the recirculation zone mix with the main flow and ignite it[Gla87, Oat85].

Curan has done extensive research into coaxial dump combustors and has developed a design methodology[Cur79]. More recently, Morrison has refined the dump combustor design methodology[Mor97]. Both techniques are highly empirical.

A similar process is occurring with the Minnesota experiment. After the gas is expanded to its final temperature, pressure and supersaturation, it exits the nozzle into a chamber. The interface between the nozzle and the chamber is a large sudden expansion. This sudden expansion causes turbulent recirculation
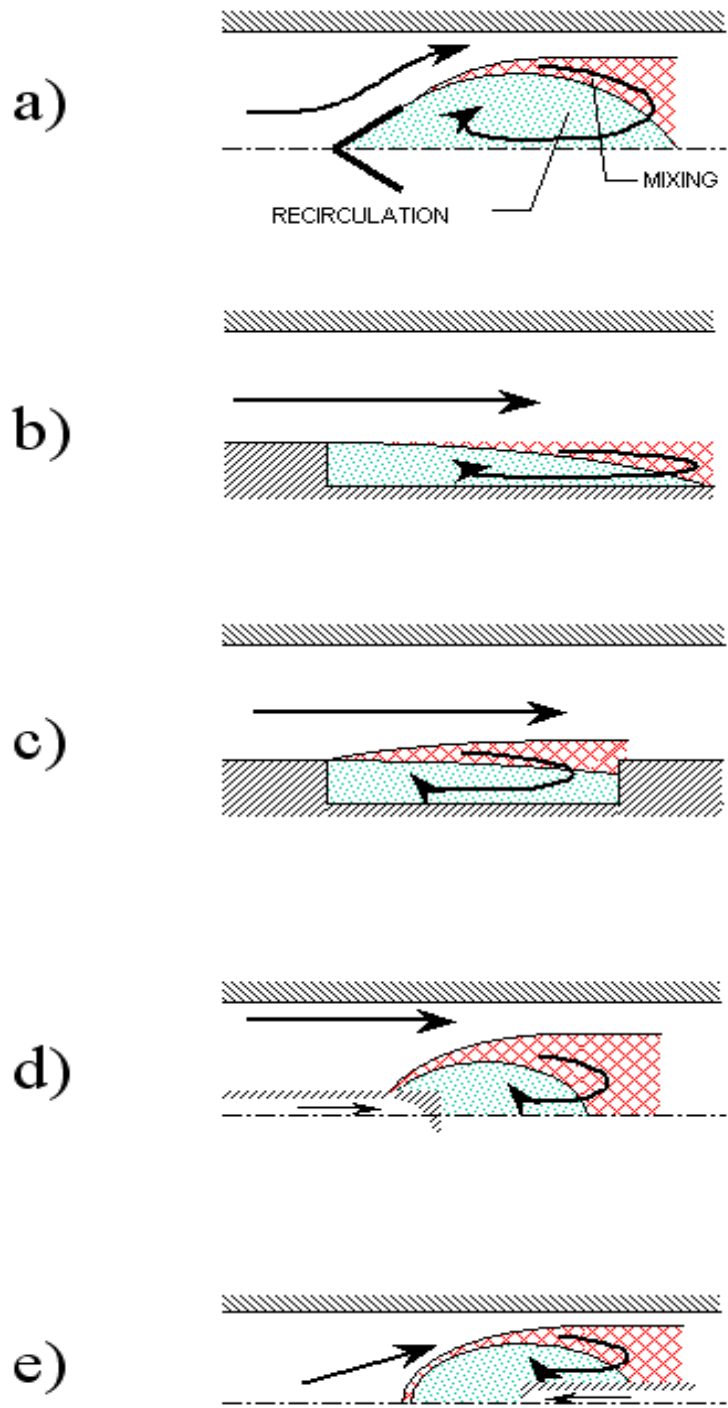
Figure 4.8: Flame/Nucleation Stabilization Schemes for Premixed Flows (After Oates[Oat85])

zones to occur. Complete nucleation occurs within the recirculation zones. The complete nucleation products from the recirculation zones mix with the main stream. The nucleation products from the recirculation zones act as nucleation seeds in the main stream and promote nucleation there.

Unfortunately, the geometry of the chamber is not given, so a crude approximation will need to be made. It will be assumed that the nucleation process occuring at the nozzle/chamber interface can be modeled as a well stirred reactor. The time constant will be determined a posteriori and checked for reasonableness. The results of the model are shown in figure 4.9. The resultant time constant, τ, is 2.5 sec. The monomer concentration at the nozzle exit is 4.4×10^{13} cm^{-3} which compares very well with the results of 6.2×10^{13} cm^{-3} from the nozzle expansion model and Ref. [Rao95]. The geometry of the resultant dump condenser to achieve this characteristic time constant was estimated using the method outlined by Morrison[Mor97]. This geometry is shown in figure 4.10.

In order to test the validity of the model, the time constant, τ, was varied from 2.0 sec to 2.5 sec. Results are shown in figure 4.11. As expected, the results show the number density and dispersion increasing with increasing τ.

4.3   Design Applications

In this section, it will be shown how the model developed herein can be used to design nanophase material reactors. Suppose it is desired to form nanophase silicon particles of average particle diameter of 30 nm and with a very narrow size distribution. The two variables in our control are the characteristic time constant, τ, and the saturation ratio at the dump plane. In addition, in order to ensure reasonable reactor geometries, we restrict the characteristic time constant, τ, to
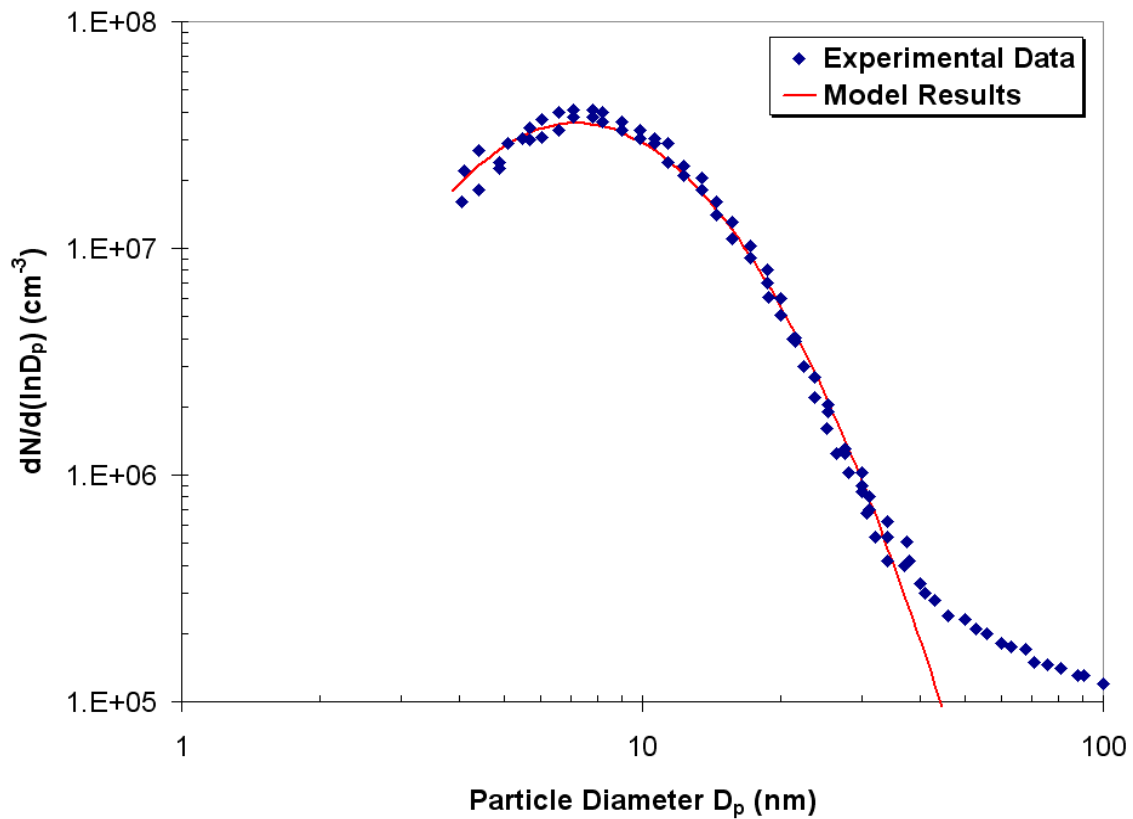
Figure 4.9: Comparison of Model to Experiment
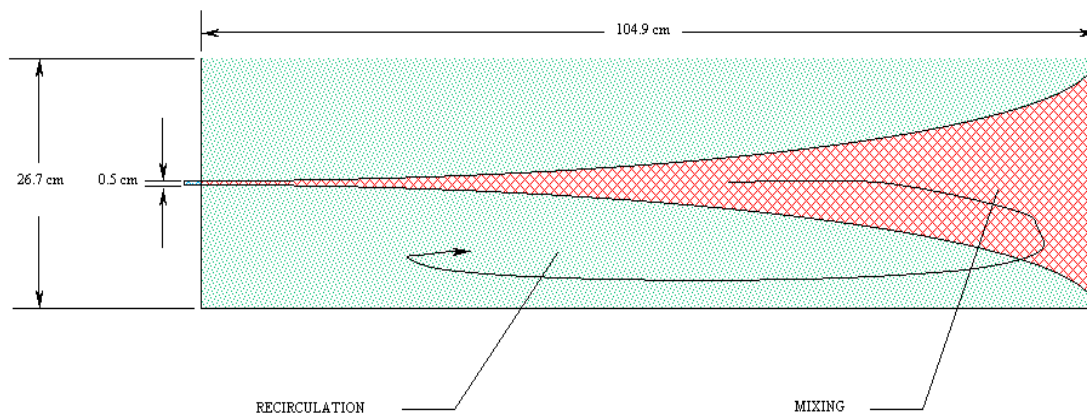
Figure 4.10: Minnesota Experiment Estimated Dump Condenser Geometry
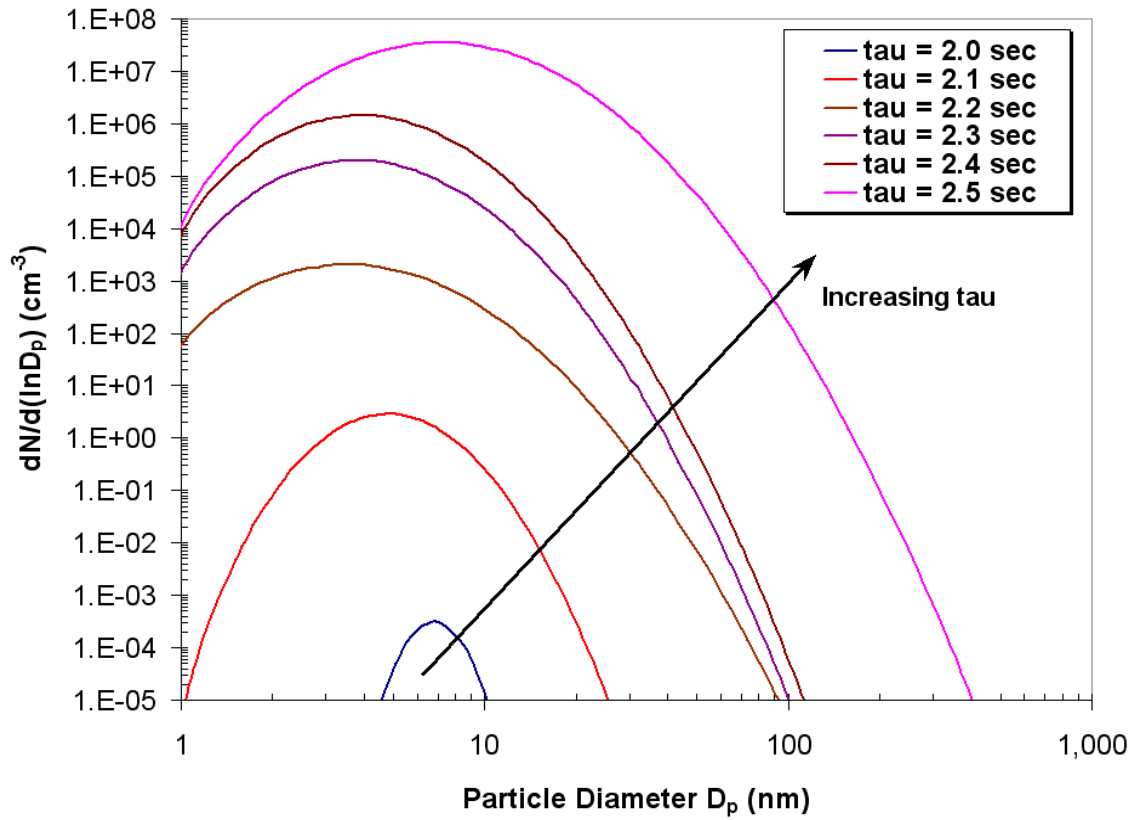
Figure 4.11: Results of Varying τ on Final Distribution

0.01 *sec*. Further, let us keep the nucleation temperature at 1, 800 K, the pressure at 400 *torr*, use argon as the carrier gas, and the nozzle diameter at 5 *mm*. Using the method developed by Morrison[Mor97] to design the dump nucleator, we get the geometry illustrated in figure 4.12. The desired particle size distribution is illustrated in figure 4.13. The Minnesota results are included for comparison. Using the above stated conditions and the desired size distribution, the initial conditions and the conditions at the dump plane can be determined from the model developed herein. Results of the calculation are given in table 4.2.
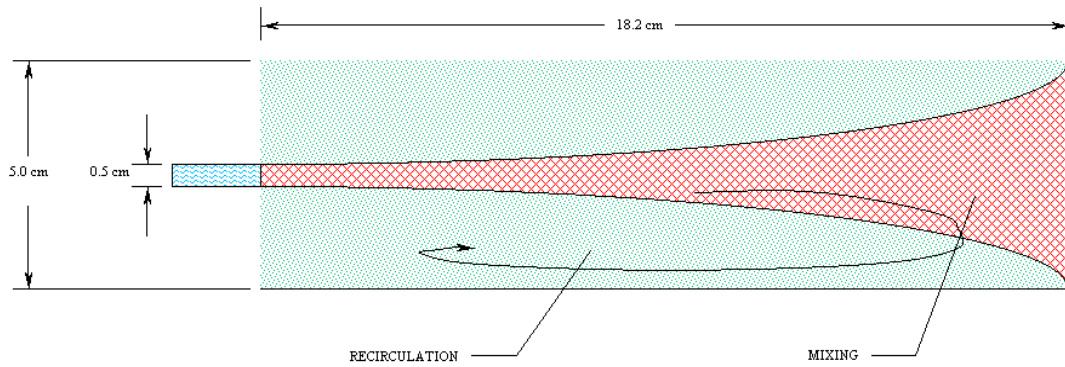
Figure 4.12: Design Case Nanophase Si Reactor Design
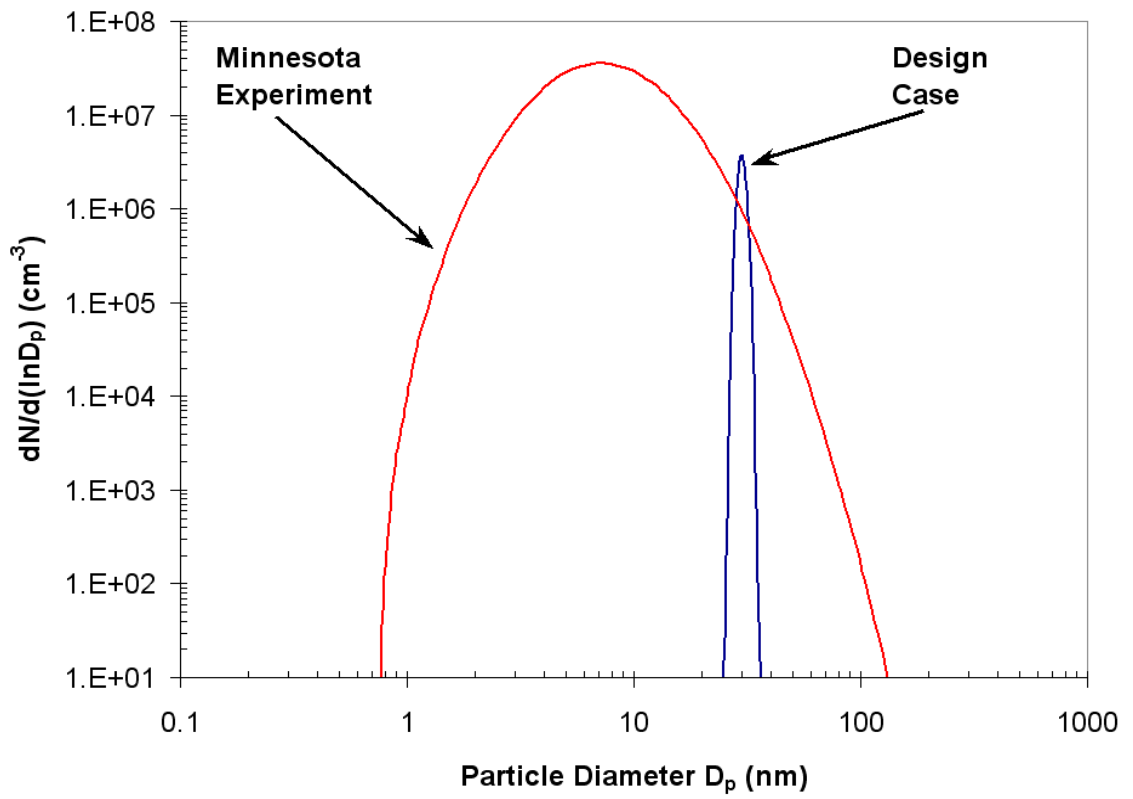
Figure 4.13: Design Case Distribution

Table 4.2: Design Case Results

		Dump	
	$Inlet$	$Upstream$	$Downstream$
$Diameter$ (cm)	$-$	0.5	5
$Length$ (cm)	$-$	$-$	18.2
$Pressure$ $(torr)$	$1,557$	400	400
$Temperature$ (K)	$3,100$	$1,800$	$1,800$
N_{Si} (cm^{-3})	7.2×10^{15}	3.2×10^{15}	3.2×10^{15}
$Saturation Ratio$	0.016	841.5	841.5
$Velocity$ (m/s)	$-$	$1,163$	$-$
$Mach No.$	$-$	1.472	$-$

CHAPTER 5

Conclusions and Recommendations

The work performed in this thesis has demonstrated that

1) Quantum mechanics calculations are needed to accurately determine the characteristics of small-size clusters (e.g. shapes, binding energies, vibrational modes, etc.).

2) Small size cluster energetics can be tied to large size cluster energetics by a modified capillary model.

3) The QRRK theory predicts the energy transfer limited recombination and dissociation reactions of the small size clusters fairly well. For larger size clusters where the recombination/dissociation reactions are not energy transfer limited, the QRRK method reverts to absolute rate theory (also known as transition state theory (TST)).

4) Rates predicted by QRRK and TST are much smaller than rates predicted by collision rate theory.

5) Fissioning of large clusters with one fission fragment larger than 1 atom in size is easily modeled with the methods developed herein. This cannot be easily achieved with collision rate theory.

6) The rate equations coupled to the gas dynamics equations show that nucleation of nano-clusters does not occur in the quenching nozzle experiment performed at the University of Minnesota. The gas velocity in the nozzle is much

greater than the nucleation rate, and most of the particles at the nozzle exit are monomers or dimers.

7) Nucleation is occurring outside the nozzle where the gas exits the nozzle into the vacuum chamber.

8) Nucleation is stabilized by the turbulent recirculation zones that are created at the nozzle exit by the sudden expansion.

9) The model developed herein predicts the results of the University of Minnesota experiment very well, although the exact geometry of the experimental apparatus and turbulent recirculation zone pattern are not known. Only the nozzle geometry is reported.[Rao95]

10) The turbulent recirculation zone pattern and characteristic time constant determined herein to match experimental results obtained in Ref. [Rao95] are reasonable.

11) The model developed herein can be used to design nanophase material reactors to yield a desired size distribution. The two parameters which control the resultant size distribution are the characteristic time constant, τ, and the saturation ratio in the reaction zone.

The research presented herein offers numerous opportunities for future work. An experiment should be designed to verify the model. As stated earlier, details of the experimental apparatus associated with the experimental data used to validate the model are unknown. Only the nozzle geometry is described in detail. Earlier researchers assumed that nucleation would occur in the nozzle prior to it exiting into the vacuum vessel[Rao95]. Now that it has been shown that the condensation holding mechanism - which is analogous to the flame holding mechanism in combustion - presented herein agrees very well with the experimental data, an experiment should be designed to confirm this hypothesis.

Another opportunity for future work would be to couple the rate equations developed herein to a computational fluid dynamics (CFD) model. This would enable a researcher to investigate the finer details of the condensation reactor physics. It is envisioned, during reactor design, that the gross design will be determined by the methods developed herein, but the design would be refined using a CFD model with the rate expressions coupled to it.

Other opportunities for future work are to expand the model to include other materials of interest. Silicon was chosen for this work because there was experimental data available with which to compare this model. The model presented herein can be applied to any number of materials, and is not limited to single component materials, but can be expanded to include multi-component materials such as SiC, Al_2O_3, TiO, metal alloys, etc.

APPENDIX A

Silicon Data from Quantum Mechanics Calculations

A.1   Silicon Dimer

The silicon dimer is shown in figure A.1. The normal modes of vibration for the silicon dimer are given in table A.1. The electron density is shown in figure A.2.

Table A.1: Silicon Cluster Dimer Normal Modes of Vibration

| Mode	PM3[Ste89]		TZV[MC80]	
	Frequency (cm^{-1})	Intensity $\left(Debye^2/Amu - \mathring{A}^2\right)$	Frequency (cm^{-1})	Intensity $\left(Debye^2/Amu - \mathring{A}^2\right)$
1	723.01	0.00000	551.64	0.00000

Figure A.1: Silicon Cluster Dimer
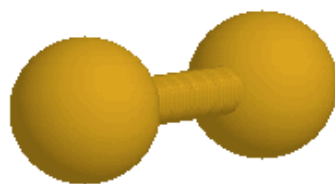
Figure A.2: Silicon Dimer Electron Density

A.2 Silicon Trimer

The silicon trimer is shown in figure A.3. The normal modes of vibration for the silicon trimer are given in table A.2. The electron density is shown in figure A.4.
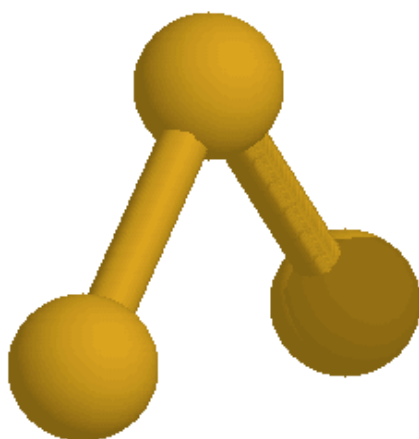

Figure A.3: Silicon Cluster Trimer

Table A.2: Silicon Cluster Trimer Normal Modes of Vibration

|	PM3[Ste89]		TZV[MC80]	
Mode	Frequency (cm^{-1})	Intensity $\left(Debye^2/Amu - \mathring{A}^2\right)$	Frequency (cm^{-1})	Intensity $\left(Debye^2/Amu - \mathring{A}^2\right)$
1	139.9	0.02282	123.05	0.23229
2	449.18	0.05647	491.23	0.26916
3	501.06	0.10964	516.79	2.26295
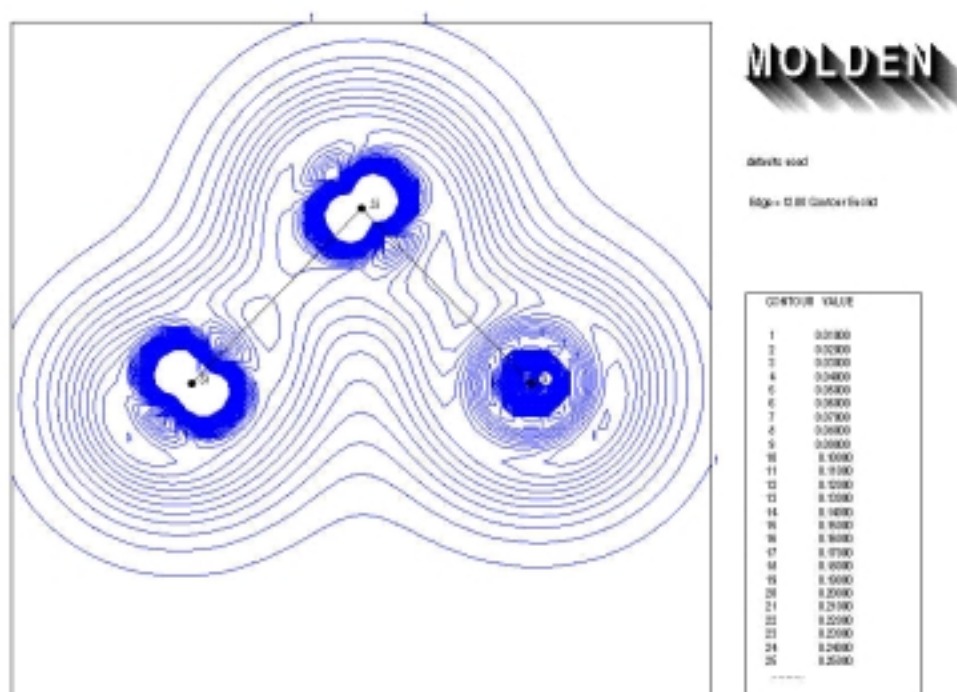
Figure A.4: Silicon Trimer Electron Density

A.3 Silicon Quadramer

The silicon quadramer is shown in figure A.5. The normal modes of vibration for the silicon quadramer are given in table A.3. The electron density is shown in figure A.6.
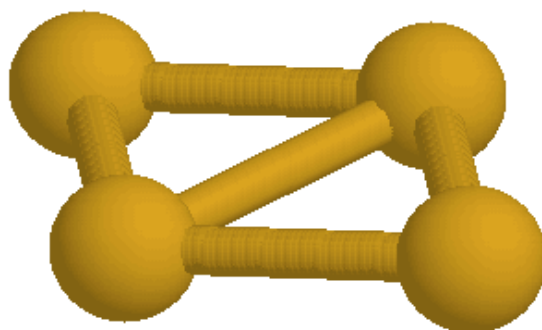
Figure A.5: Silicon Cluster Quadramer

Table A.3: Silicon Cluster Quadramer Normal Modes of Vibration

	PM3[Ste89]		TZV[MC80]	
Mode	Frequency (cm^{-1})	Intensity $\left(Debye^2/Amu - \AA^2\right)$	Frequency (cm^{-1})	Intensity $\left(Debye^2/Amu - \AA^2\right)$
1	123.64	0.08687	137.34	0.00476
2	182.38	0.51674	140.93	0.0037
3	313.26	0.00000	336.62	0.00000
4	391.72	0.00000	389.59	0.00000
5	475.68	0.13065	436.83	0.00000
6	519.99	0.00000	485.62	4.07875
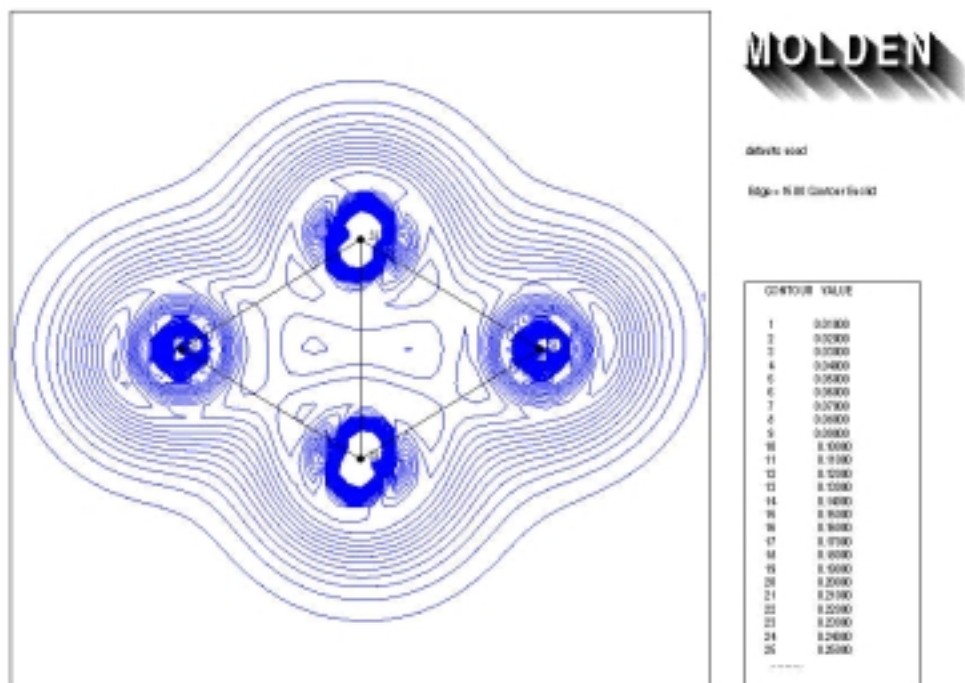
Figure A.6: Silicon Quadramer Electron Density

A.4   Silicon Pentamer

The silicon pentamer is shown in figure A.7. The normal modes of vibration for the silicon pentamer are given in table A.4. The electron density is shown in figure A.8.
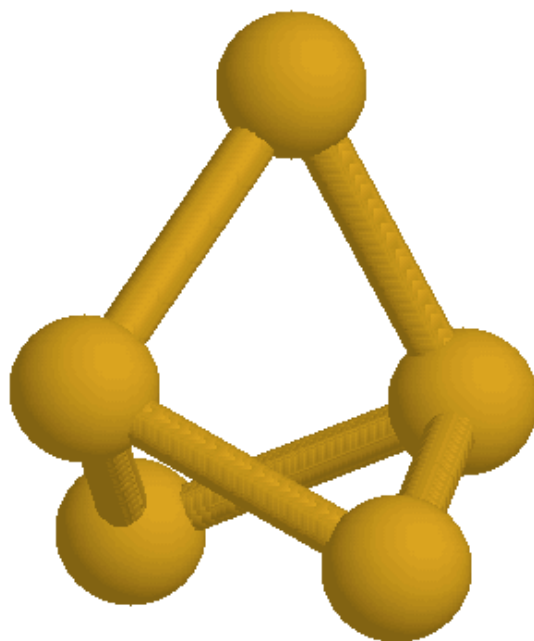

Figure A.7: Silicon Cluster Pentamer

Table A.4: Silicon Cluster Pentamer Normal Modes of Vibration

|	PM3[Ste89]		TZV[MC80]	
Mode	Frequency (cm^{-1})	Intensity $\left(Debye^2/Amu - \mathring{A}^2\right)$	Frequency (cm^{-1})	Intensity $\left(Debye^2/Amu - \mathring{A}^2\right)$
1	145.39	0.08189	159.52	0.01846
2	145.44	0.08156	159.52	0.01845
3	147.81	0.00000	244.57	0.00000
4	305.09	0.00000	252.38	0.00000
5	305.09	0.00000	252.4	0.00000
6	372.47	0.15935	252.4	0.205
7	408.73	0.00862	421.66	0.00000
8	408.81	0.00846	433.24	1.87644
9	493.4	0.00000	433.26	1.87583
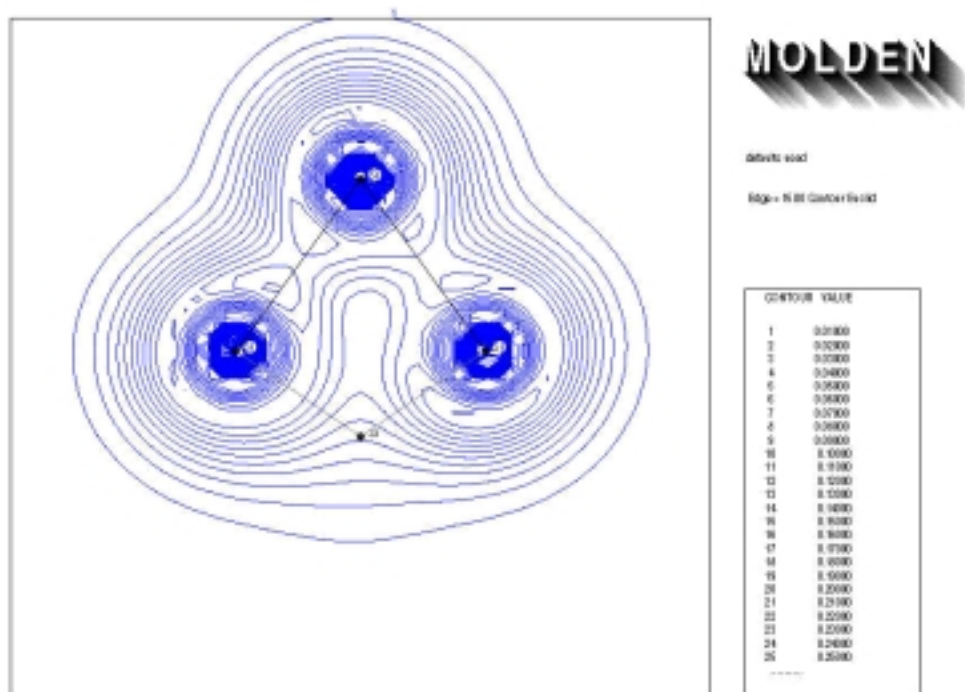
Figure A.8: Silicon Pentamer Electron Density

A.5 Silicon Hexamer

The silicon hexamer is shown in figure A.9. The normal modes of vibration for the silicon hexamer are given in table A.5. The electron density is shown in figure A.10.
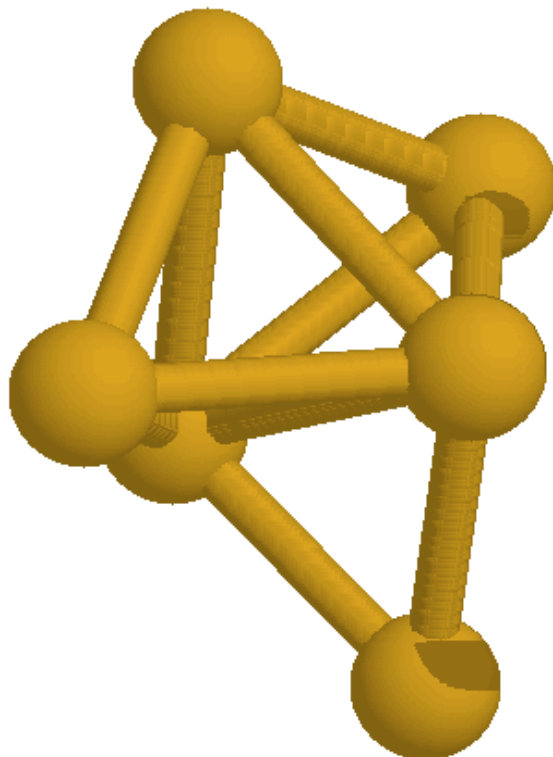

Figure A.9: Silicon Cluster Hexamer

Table A.5: Silicon Cluster Hexamer Normal Modes of Vibration

	PM3[Ste89]		TZV[MC80]	
Mode	Frequency (cm^{-1})	Intensity $\left(Debye^2/Amu - \mathring{A}^2\right)$	Frequency (cm^{-1})	Intensity $\left(Debye^2/Amu - \mathring{A}^2\right)$
1	63	0.2446	16.94	0.00733
2	63	0.2446	54.47	0.00045
3	163.43	0.00000	173.65	0.01131
4	251.72	0.00000	223.9	0.03794
5	275.37	0.00000	249.62	0.21453
6	357.47	0.00000	251.11	0.00000
7	374.89	0.148	312.17	0.03452
8	399.35	0.00000	346.92	0.00201
9	399.35	0.00000	351.65	0.0003
10	482.16	0.05053	413.42	0.02072
11	482.16	0.05053	452.97	1.27915
12	552.1	0.00000	461.41	1.3757
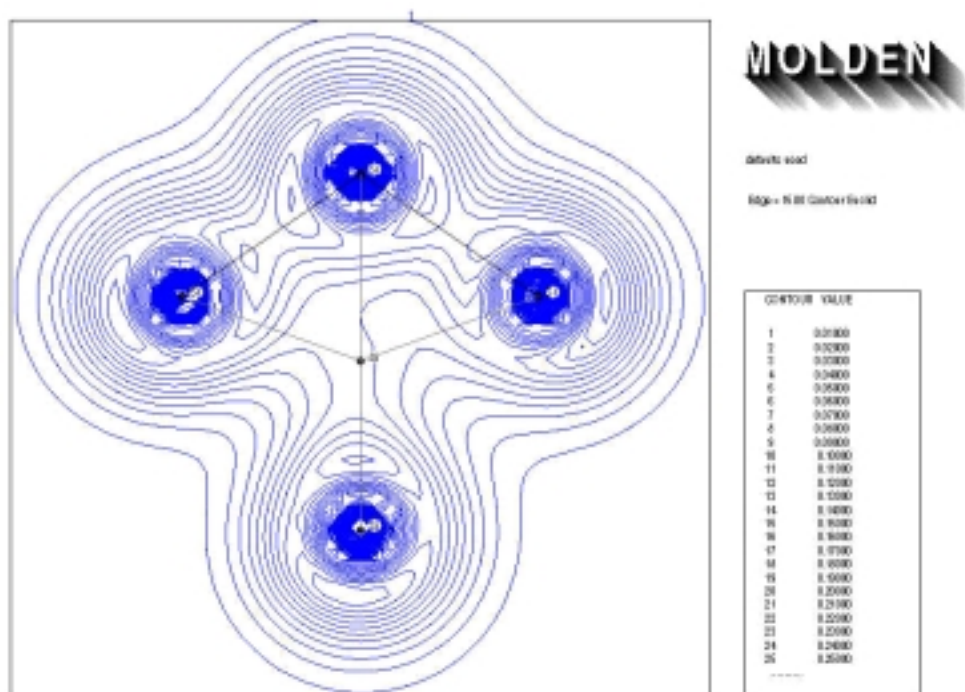
Figure A.10: Silicon Hexamer Electron Density

A.6 Silicon Heptamer

The silicon heptamer is shown in figure A.11. The normal modes of vibration for the silicon heptamer are given in table A.6. The electron density is shown in figure A.12.
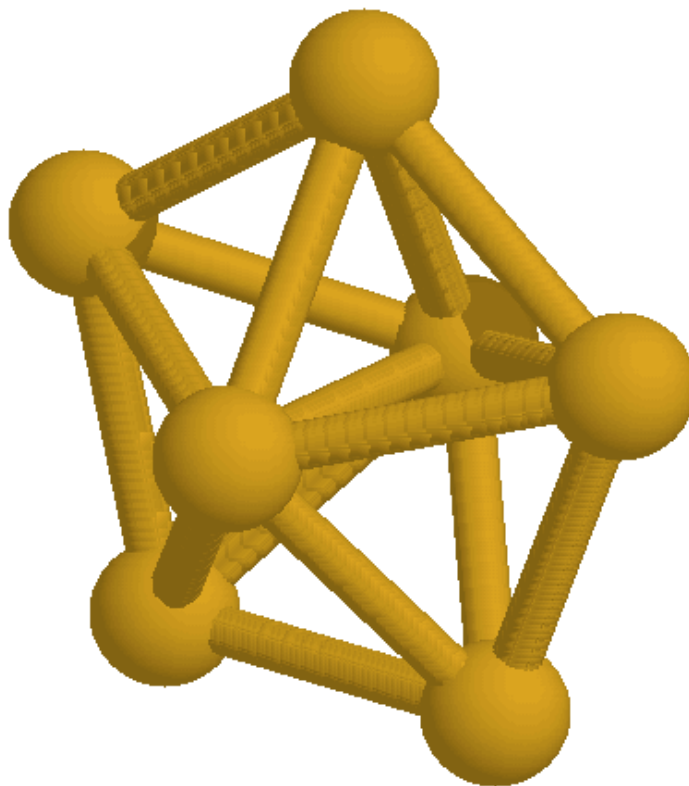

Figure A.11: Silicon Cluster Heptamer
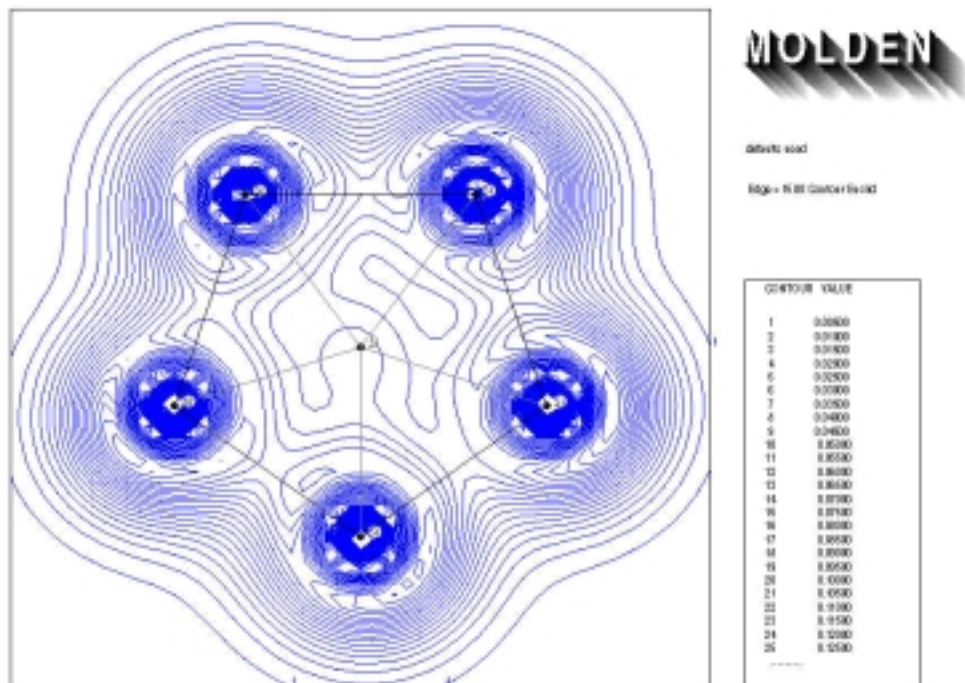
Figure A.12: Silicon Heptamer Electron Density

Table A.6: Silicon Cluster Heptamer Normal Modes of Vibration

	PM3[Ste89]		TZV[MC80]	
Mode	Frequency (cm^{-1})	Intensity $\left(Debye^2/Amu - \AA^2\right)$	Frequency (cm^{-1})	Intensity $\left(Debye^2/Amu - \AA^2\right)$
1	188.52	0.00000	115.47	0.00000
2	188.52	0.00000	115.47	0.00000
3	263.2	0.28387	195.98	0.00149
4	263.2	0.28387	221.7	0.00000
5	287.35	0.00003	221.7	0.00000
6	306.22	0.00000	224.52	0.00032
7	306.22	0.00000	224.52	0.00032
8	338.02	0.00000	325.41	0.00000
9	387.64	0.00000	325.41	0.00000
10	387.65	0.00000	337.72	0.00000
11	411.42	0.00000	337.72	0.00000
12	411.42	0.00000	353.41	0.00000
13	517.98	0.12122	398.43	0.00000
14	517.98	0.12122	409.82	1.10352
15	560.78	0.00000	409.82	1.10352

A.7 Silicon Octamer

The silicon octamer is shown in figure A.13. The normal modes of vibration for the silicon octamer are given in table A.7. The electron density is shown in figure A.14.
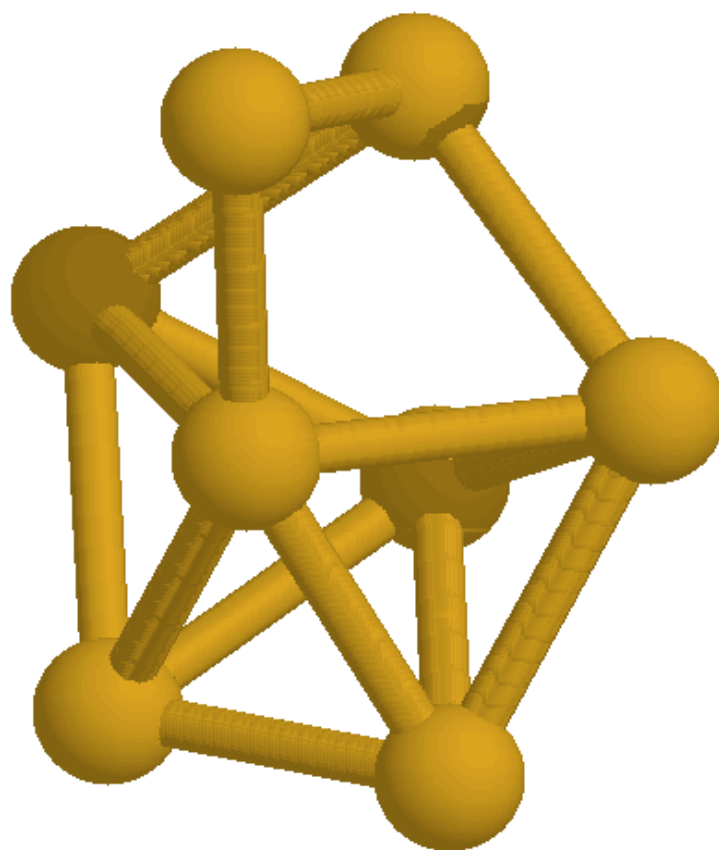
Figure A.13: Silicon Cluster Octamer
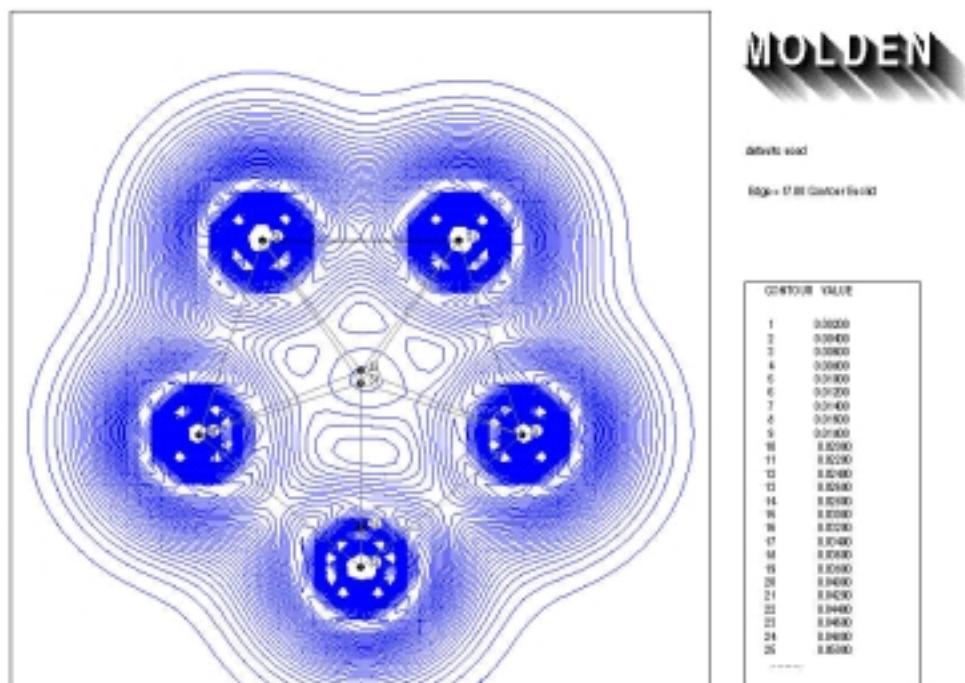
Figure A.14: Silicon Octamer Electron Density

Table A.7: Silicon Cluster Octamer Normal Modes of Vibration

Mode	PM3[Ste89]		TZV[MC80]	
	Frequency (cm^{-1})	Intensity $\left(Debye^2/Amu - \mathring{A}^2\right)$	Frequency (cm^{-1})	Intensity $\left(Debye^2/Amu - \mathring{A}^2\right)$
1	81.44	0.05369	82.62	0.03147
2	90.75	0.31763	97.26	0.00225
3	174.5	0.42972	121.77	0.00033
4	211.36	0.12348	160.28	0.10092
5	223.55	0.00009	160.78	0.01742
6	249.59	0.01658	175.49	0.01896
7	265.03	0.03199	180.3	0.04206
8	302.91	0.39197	192.8	0.00363
9	303.55	0.15788	235.51	0.0423
10	308.16	0.01734	256.39	0.02787
11	377.23	0.12714	281.75	0.01623
12	380.88	0.06426	296.34	0.03787
13	390.53	0.02665	321.88	0.01015
14	399.2	0.01705	344.92	0.06402
15	431.11	0.24902	354.41	0.17971
16	477.41	0.34181	376.12	0.11813
17	487.99	0.28036	388.75	1.07102
18	533.1	0.13735	496.72	0.8298

A.8 Silicon Nanomer

The silicon nanomer is shown in figure A.15. The normal modes of vibration for the silicon nanomer are given in table A.8. The electron density is shown in figure A.16.
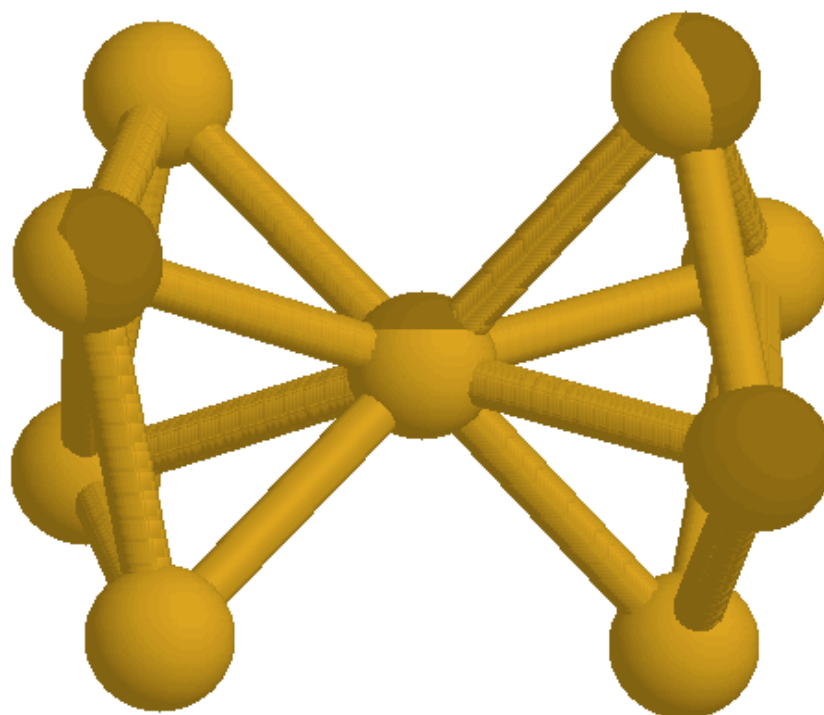


Figure A.15: Silicon Cluster Nanomer
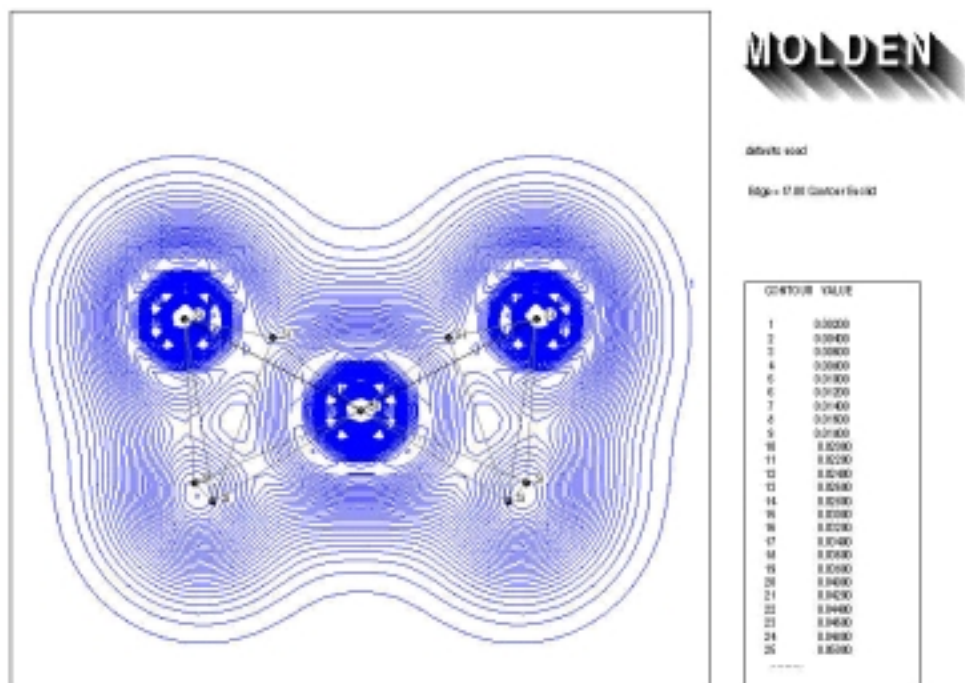
Figure A.16: Silicon Nanomer Electron Density

Table A.8: Silicon Cluster Nanomer Normal Modes of Vibration

	PM3[Ste89]		TZV[MC80]	
Mode	Frequency (cm^{-1})	Intensity $\left(Debye^2/Amu - \mathring{A}^2\right)$	Frequency (cm^{-1})	Intensity $\left(Debye^2/Amu - \mathring{A}^2\right)$
1	152.32	0.00416	21.16	0.00035
2	178.23	0.00000	27.75	0.01633
3	203.18	0.07906	60.15	0.02307
4	217.47	0.00277	145.07	0.00000
5	223.55	0.16908	153.84	0.44342
6	263.49	0.00000	156.67	0.00617
7	263.79	0.25169	172.91	0.00245
8	263.79	0.7914	184.75	0.00000
9	276.5	0.00006	216.58	0.10542
10	286.41	0.0345	240.39	0.06879
11	307.68	0.76757	268.16	0.66134
12	318.21	0.00184	298.97	0.00000
13	363.42	0.80009	309.52	0.32655
14	401.33	0.00743	315.03	0.1204
15	401.63	0.00137	325.14	0.00013
16	411.07	0.04661	337.57	0.12972
17	434.38	0.00016	384.5	0.0105
18	450.34	0.87291	407.31	0.00009
19	486.07	0.35218	453.84	0.43244
20	498.46	0.00052	455.1	1.70171
21	532.32	0.94482	490.14	5.4624

A.9 Silicon Decamer

The silicon decamer is shown in figure A.17. The normal modes of vibration for the silicon decamer are given in table A.9. The electron density is shown in figure A.18.
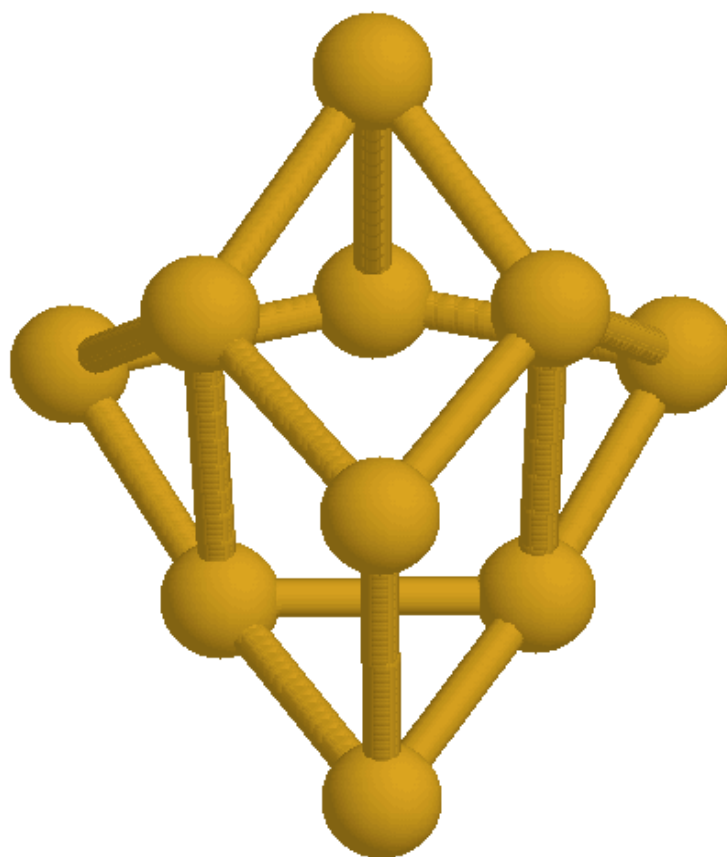

Figure A.17: Silicon Cluster Decamer

Table A.9: Silicon Cluster Decamer Normal Modes of Vibration

	PM3[Ste89]		TZV[MC80]	
Mode	Frequency (cm^{-1})	Intensity $\left(Debye^2/Amu - \mathring{A}^2\right)$	Frequency (cm^{-1})	Intensity $\left(Debye^2/Amu - \mathring{A}^2\right)$
1	107.4	0.0506	97.67	0.01633
2	129.23	0.25013	115.43	0.06006
3	163.77	0.05906	122.51	0.0502
4	177.28	0.13912	138.76	0.03576
5	195	0.0544	156.12	0.01204
6	210.14	0.04283	182.55	0.00721
7	245.65	0.17557	187.72	0.0155
8	272.46	0.15356	203.19	0.05347
9	280.3	0.28278	208.69	0.08163
10	290.24	0.08212	220.64	0.01632
11	295.47	0.35968	233.96	0.00235
12	319.57	0.15844	236.53	0.00282
13	327.49	0.10226	243.44	0.00004
14	339.12	0.03904	250.65	0.02034
15	343.36	0.08822	287.54	0.08173
16	395.49	0.02072	311.39	0.2188
17	401.86	0.12305	332.5	0.01736
18	429.71	0.1444	369.29	0.03418
19	437.95	0.05694	386.16	0.00002
20	457.07	0.24305	399.99	0.37683

Table A.9: (continued)

| Mode	PM3[Ste89]		TZV[MC80]	
	Frequency (cm^{-1})	Intensity $\left(Debye^2/Amu - \mathring{A}^2\right)$	Frequency (cm^{-1})	Intensity $\left(Debye^2/Amu - \mathring{A}^2\right)$
21	504.15	0.16464	409.26	0.5552
22	521.8	0.14993	467.95	0.38404
23	532.32	0.0147	482.17	0.6804
24	577.59	0.1588	523.81	0.89638

Figure A.18: Silicon Decamer Electron Density

APPENDIX B

Carbon Data from Quantum Mechanics Calculations

B.1   Carbon Dimer

The carbon dimer is shown in figure B.1. The normal modes of vibration for the carbon dimer are given in table B.1. The electron density is shown in figure B.2.

Table B.1: Carbon Cluster Dimer Normal Modes of Vibration

|	TZV[MC80]	
Mode	Frequency (cm^{-1})	Intensity $\left(Debye^2/Amu - \mathring{A}^2\right)$
1	1201.64	0.00000
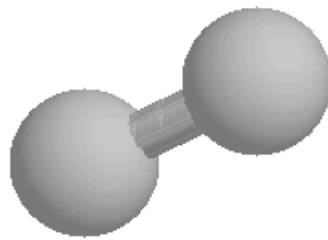
Figure B.1: Carbon Cluster Dimer
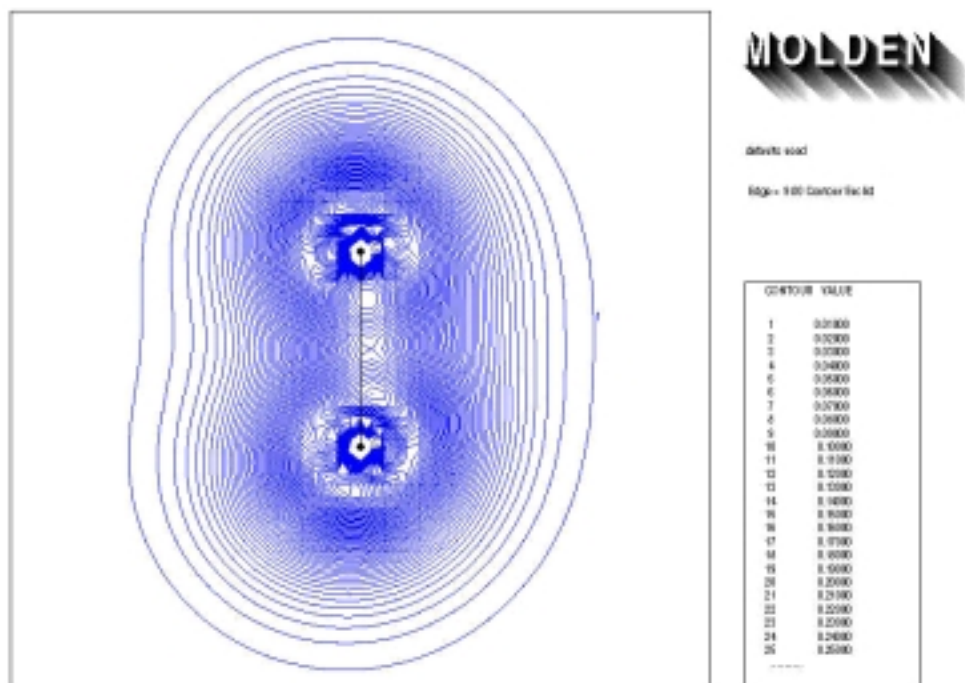
Figure B.2: Carbon Dimer Electron Density

B.2   Carbon Trimer

The carbon trimer is shown in figure B.3. The normal modes of vibration for the carbon trimer are given in table B.2. The electron density is shown in figure B.4.
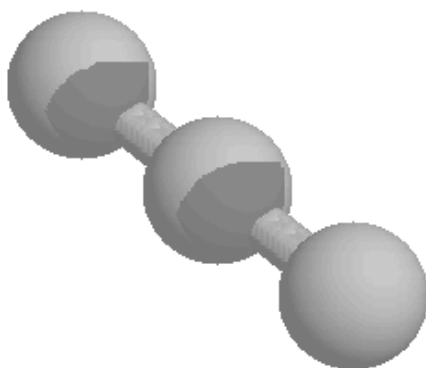

Figure B.3: Carbon Cluster Trimer

Table B.2: Carbon Cluster Trimer Normal Modes of Vibration

|	TZV[MC80]	
Mode	Frequency (cm^{-1})	Intensity $\left(Debye^2/Amu - \mathring{A}^2\right)$
1	331.67	0.00007
2	331.67	0.00007
3	1318.73	0.00000
4	2255.74	34.642
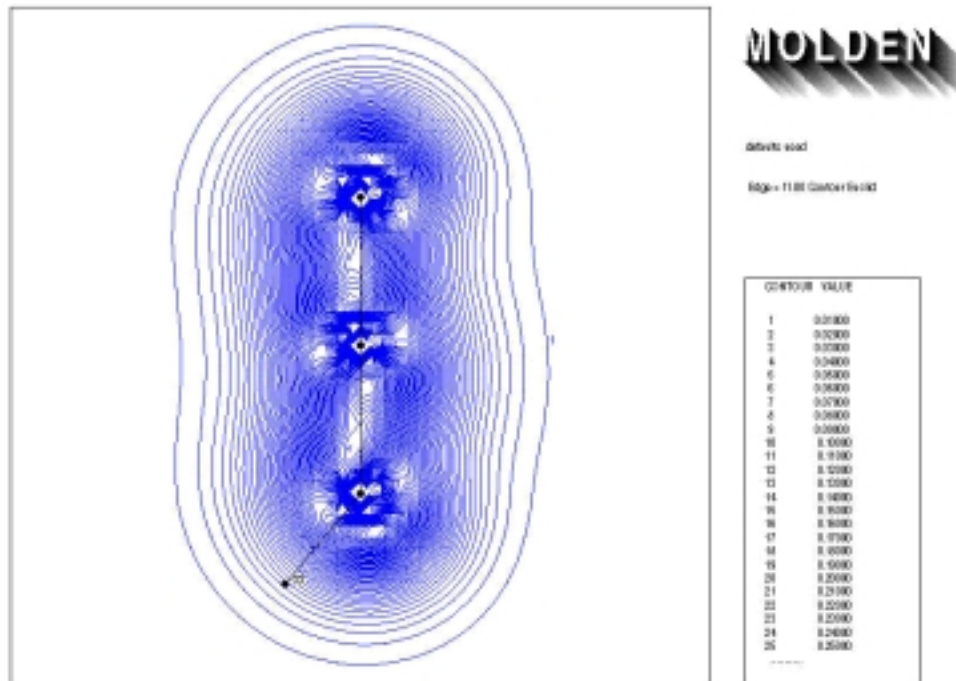
Figure B.4: Carbon Trimer Electron Density

B.3 Carbon Quadramer

The carbon quadramer is shown in figure B.5. The normal modes of vibration for the carbon quadramer are given in table B.3. The electron density is shown in figure B.6.
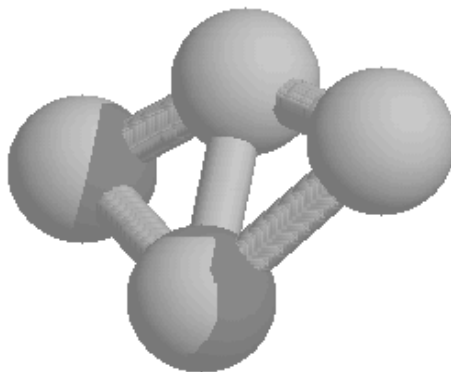

Figure B.5: Carbon Cluster Quadramer

Table B.3: Carbon Cluster Quadramer Normal Modes of Vibration

|	TZV[MC80]	
Mode	Frequency (cm^{-1})	Intensity $\left(Debye^2/Amu - \mathring{A}^2\right)$
1	371.8	0.0923
2	434.96	0.37893
3	548.22	1.0534
4	903.74	0.48928
5	1259.8	0.21754
6	1601.86	8.09854
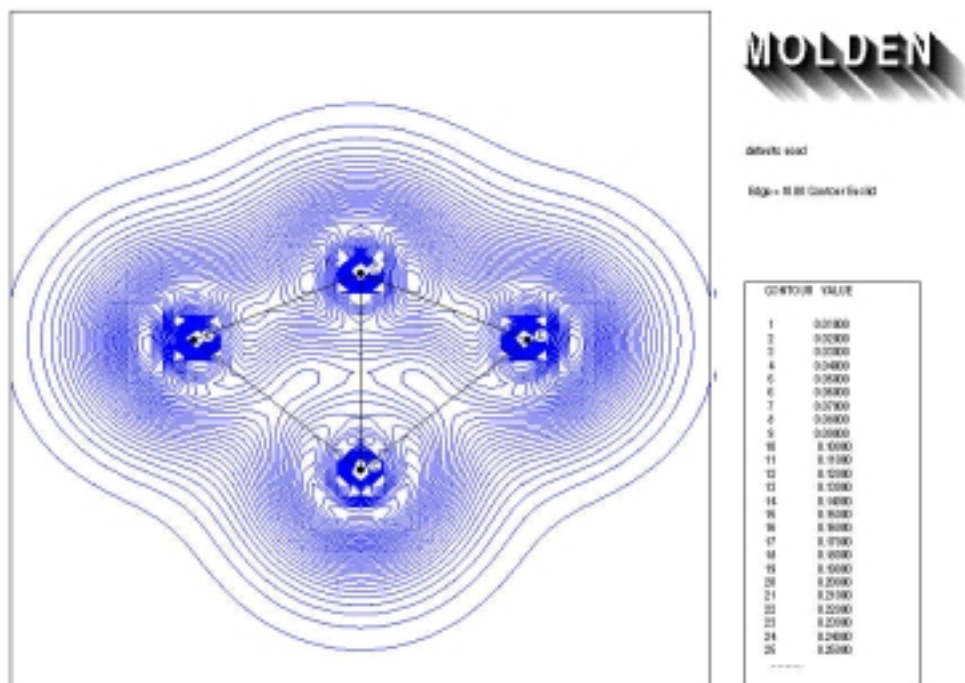
Figure B.6: Carbon Quadramer Electron Density

B.4   Carbon Pentamer

The carbon pentamer is shown in figure B.7. The normal modes of vibration for the carbon pentamer are given in table B.4. The electron density is shown in figure B.8.
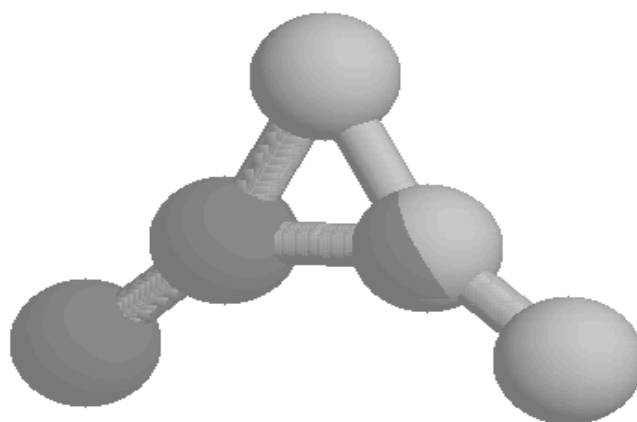

Figure B.7: Carbon Cluster Pentamer

Table B.4: Carbon Cluster Pentamer Normal Modes of Vibration

|	TZV[MC80]	
Mode	Frequency (cm^{-1})	Intensity $\left(Debye^2/Amu - \mathring{A}^2\right)$
1	316.2	0.00000
2	316.2	0.00000
3	638.52	0.25748
4	638.52	0.25777
5	638.52	0.25775
6	953.02	0.00000
7	1714.61	46.81824
8	1714.61	46.82103
9	1714.61	46.81791
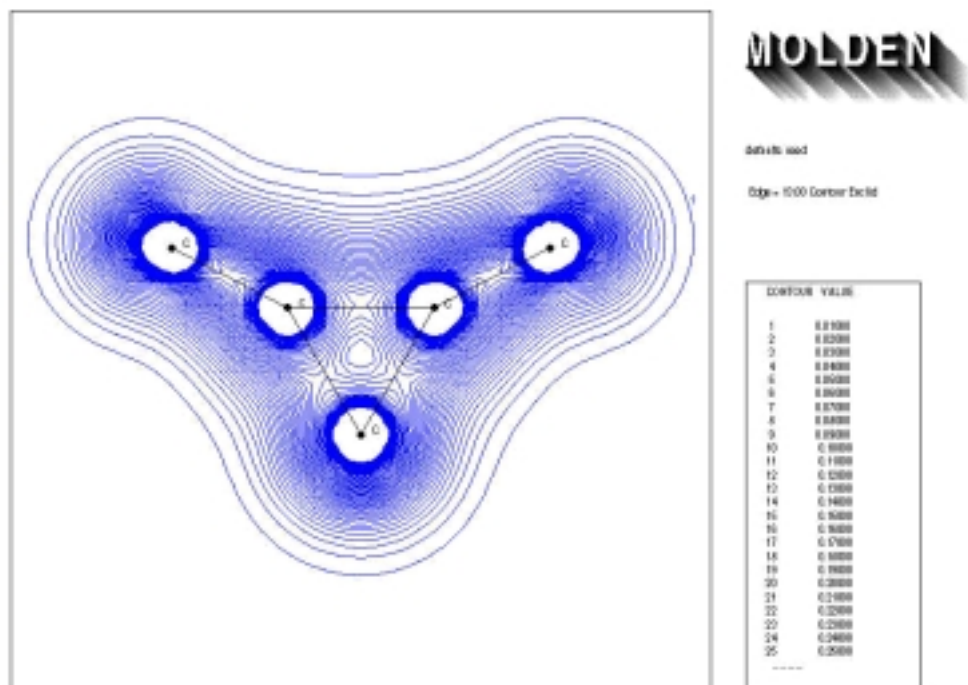
Figure B.8: Carbon Pentamer Electron Density

B.5 Carbon Hexamer

The carbon hexamer is shown in figure B.9. The normal modes of vibration for the carbon hexamer are given in table B.5. The electron density is shown in figure B.10.
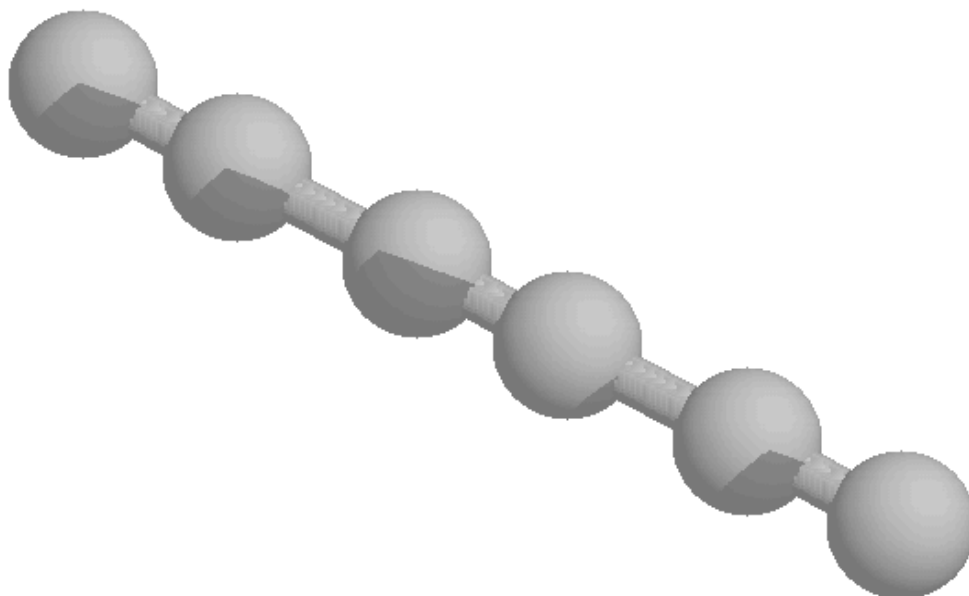
Figure B.9: Carbon Cluster Hexamer

Table B.5: Carbon Cluster Hexamer Normal Modes of Vibration

	TZV[MC80]	
Mode	Frequency (cm^{-1})	Intensity $\left(Debye^2/Amu - \mathring{A}^2\right)$
1	108.51	0.01902
2	108.51	0.01902
3	315.64	0.0001
4	315.65	0.0001
5	553.22	0.42403
6	553.22	0.42399
7	651.81	0.00000
8	1272.61	720.64918
9	1378.68	0.00000
10	1378.68	0.00000
11	2264	0.00000
12	2561.57	0.00000
13	3283.95	1000
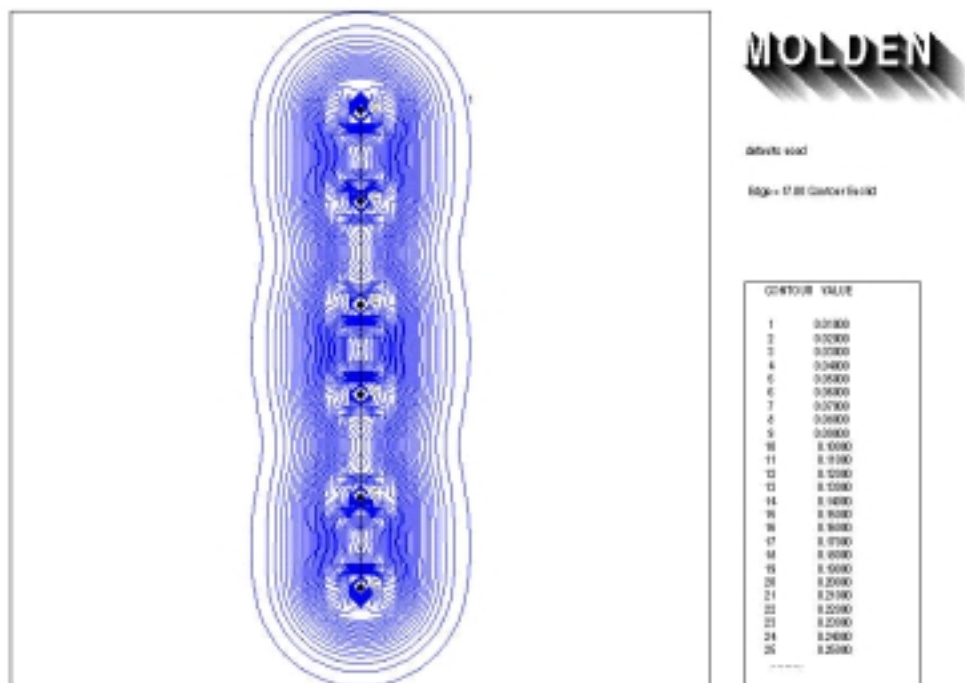
Figure B.10: Carbon Hexamer Electron Density

B.6 Carbon Heptamer

The carbon heptamer is shown in figure B.11. The normal modes of vibration for the carbon heptamer are given in table B.6. The electron density is shown in figure B.12.
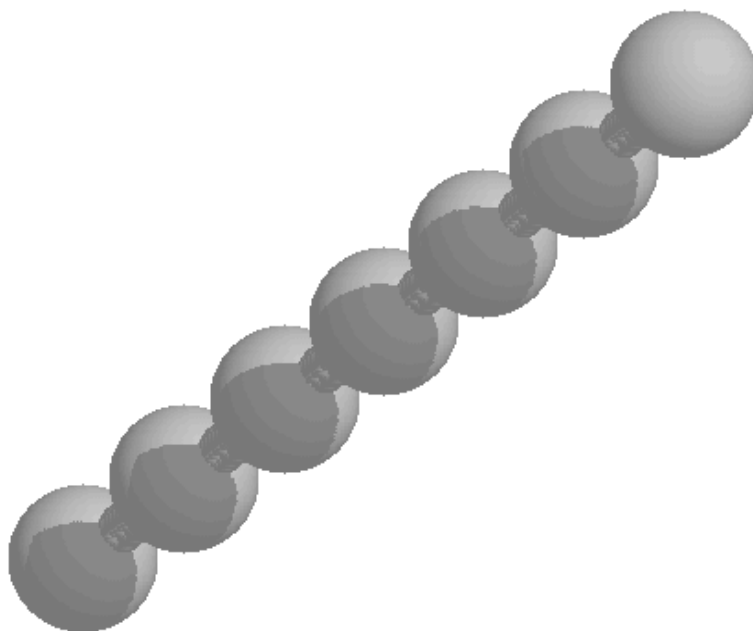

Figure B.11: Carbon Cluster Heptamer
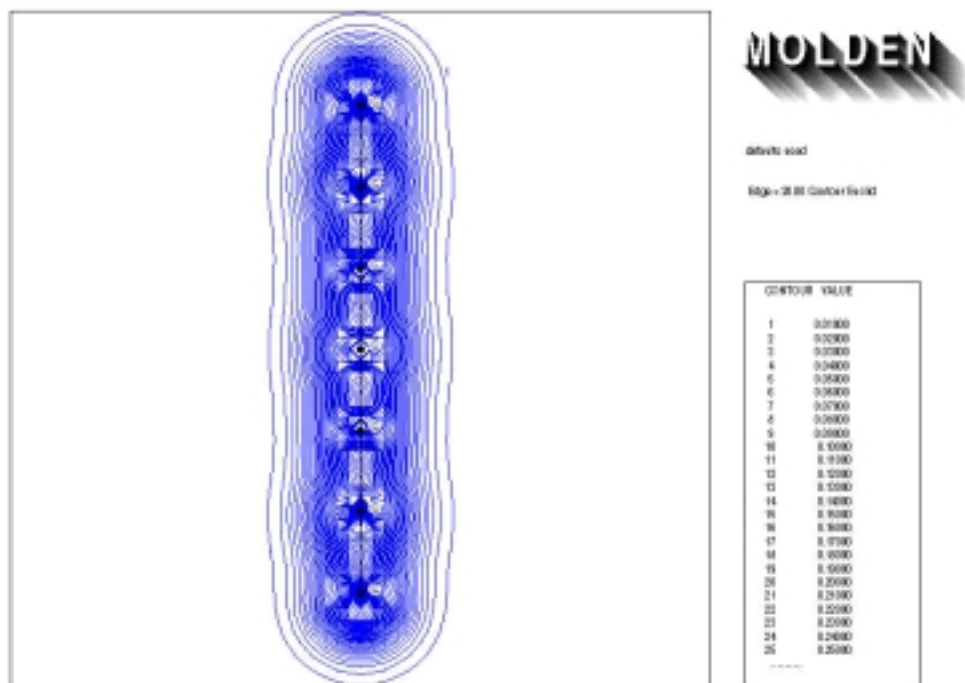
Figure B.12: Carbon Heptamer Electron Density

Table B.6: Carbon Cluster Heptamer Normal Modes of Vibration

	TZV[MC80]	
Mode	Frequency (cm^{-1})	Intensity $\left(Debye^2/Amu - \mathring{A}^2\right)$
1	75.04	0.1149
2	75.04	0.1149
3	190.21	0.0001
4	190.21	0.0001
5	323.25	0.0004
6	323.25	0.0004
7	615.03	0.00000
8	671.92	0.00000
9	671.92	0.00000
10	817.72	2.43255
11	817.72	2.43255
12	1169.94	0.00009
13	1686.66	0.00000
14	2083.78	146.52838
15	2272.61	325.57962
16	2340.6	0.00000

B.7   Carbon Octamer

The carbon octamer is shown in figure B.13. The normal modes of vibration for the carbon octamer are given in table B.7. The electron density is shown in figure B.14.
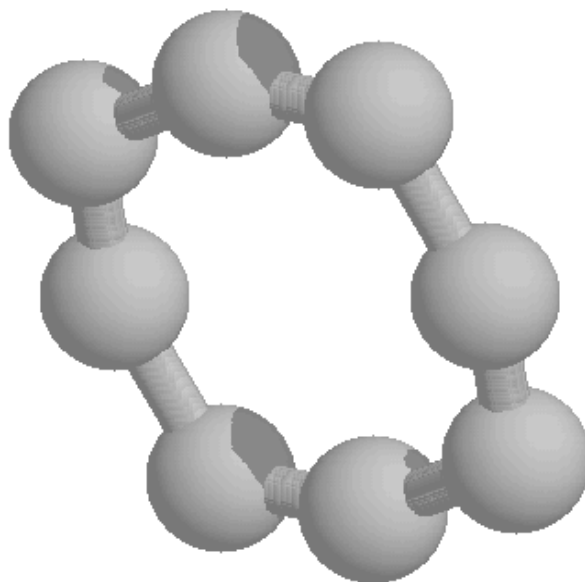
Figure B.13: Carbon Cluster Octamer

Figure B.14: Carbon Octamer Electron Density

Table B.7: Carbon Cluster Octamer Normal Modes of Vibration

	TZV[MC80]	
Mode	Frequency (cm^{-1})	Intensity $\left(Debye^2/Amu - \mathring{A}^2\right)$
1	152.14	0.0001
2	330.07	0.0001
3	358.27	0.0001
4	388.25	0.21233
5	486.86	0.00000
6	556.15	0.00000
7	556.15	0.00000
8	632.78	4.70253
9	632.78	4.70253
10	708.75	0.00000
11	948.04	0.00000
12	1069.51	1.28299
13	1069.51	1.28299
14	1256.51	0.00000
15	1872.72	0.00000
16	1952.28	0.00000
17	1971.25	10.17834
18	1971.25	10.17834

B.8   Carbon Nanomer

The carbon nanomer is shown in figure B.15. The normal modes of vibration for the carbon nanomer are given in table B.8. The electron density is shown in figure B.16.
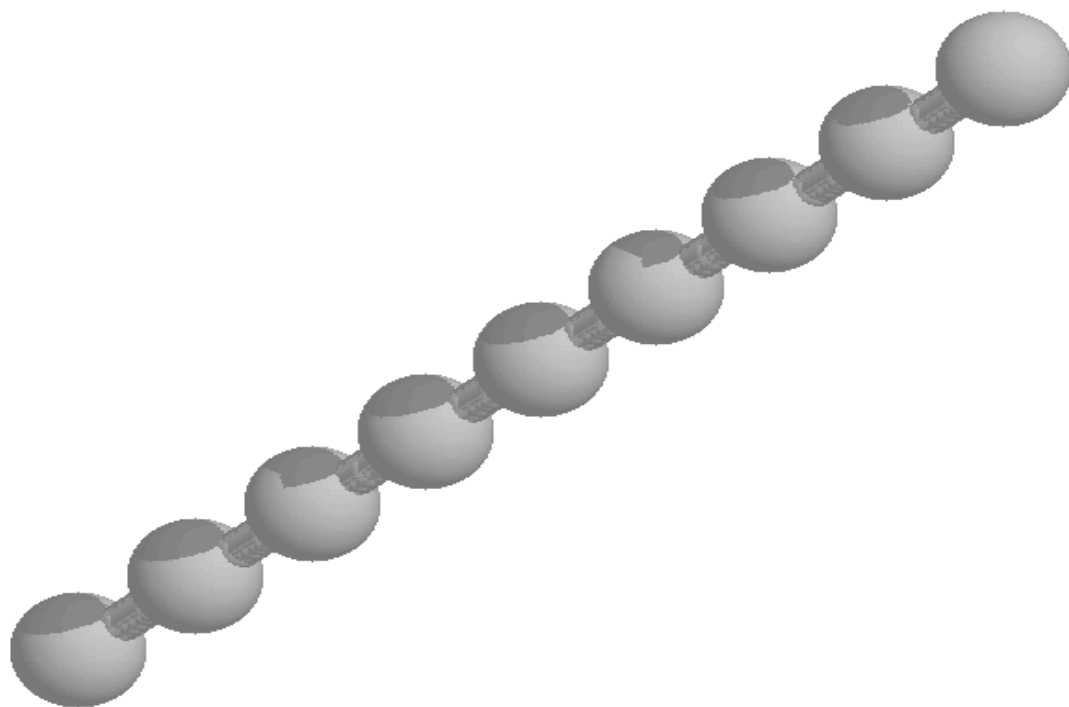
Figure B.15: Carbon Cluster Nanomer
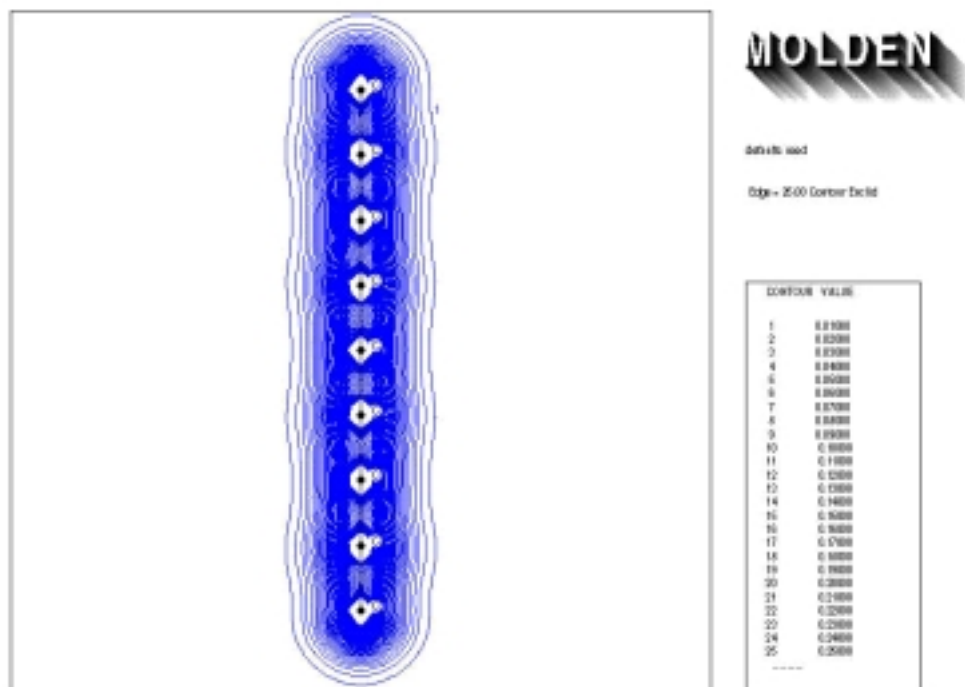
Figure B.16: Carbon Nanomer Electron Density

Table B.8: Carbon Cluster Nanomer Normal Modes of Vibration

	TZV[MC80]	
Mode	Frequency (cm^{-1})	Intensity $\left(Debye^2/Amu - \mathring{A}^2\right)$
1	215.52	0.68963
2	297.44	0.57496
3	346.8	0.41291
4	367.28	0.0001
5	462.92	0.00000
6	499.66	0.10664
7	550.93	0.63322
8	575.36	0.27231
9	627.17	0.57504
10	725.28	0.00000
11	744.31	0.92364
12	795.08	0.10486
13	839.74	0.13702
14	908.23	0.0006
15	942.55	1.23397
16	1025.03	0.20265
17	1281.46	2.25687
18	1334.83	0.0121
19	1432.03	0.05207
20	1920.34	0.37537
21	2028.1	0.07507

B.9   Carbon Decamer

The carbon decamer is shown in figure B.17. The normal modes of vibration for the carbon decamer are given in table B.9. The electron density is shown in figure B.18.
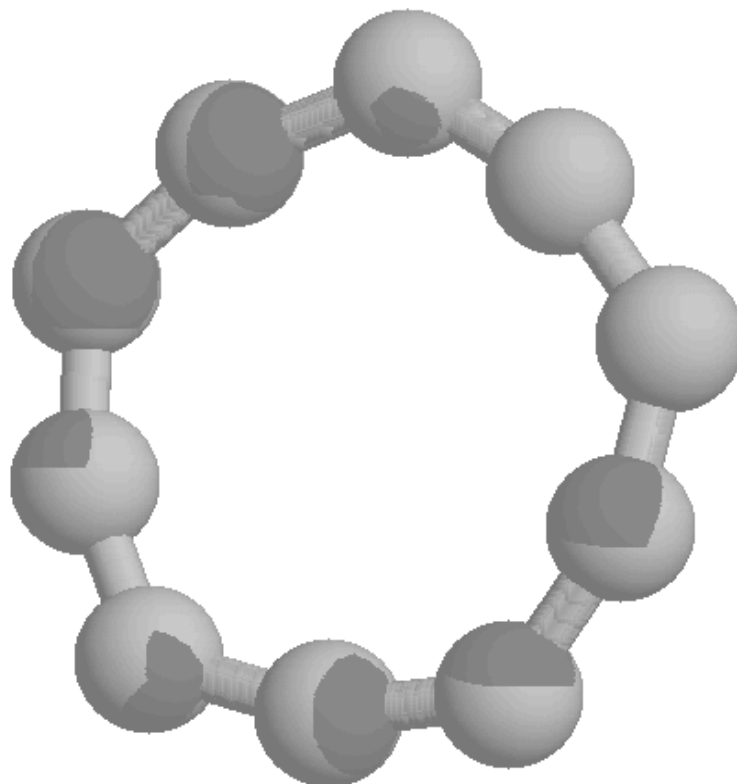


Figure B.17: Carbon Cluster Decamer

Table B.9: Carbon Cluster Decamer Normal Modes of Vibration

	TZV[MC80]	
Mode	Frequency (cm^{-1})	Intensity $\left(Debye^2/Amu - \mathring{A}^2\right)$
1	210.44	0.00000
2	210.44	0.00000
3	267.51	0.00000
4	267.51	0.00000
5	332.01	0.00000
6	470.67	0.15963
7	544.67	0.00000
8	544.67	0.00000
9	571.48	0.00000
10	571.48	0.00000
11	655.08	0.00000
12	655.08	0.00000
13	709.69	3.43059
14	709.69	3.43059
15	719.08	0.00000
16	861.32	0.00000
17	1090.93	0.96320
18	1090.93	0.96320
19	1548.12	0.00000
20	1548.12	0.00000

Table B.9: (continued)

| | TZV[MC80] | |
Mode	Frequency (cm^{-1})	Intensity $\left(Debye^2/Amu - \mathring{A}^2\right)$
21	2003.46	0.00000
22	2003.46	0.00000
23	2047.47	11.53539
24	2047.47	11.53539
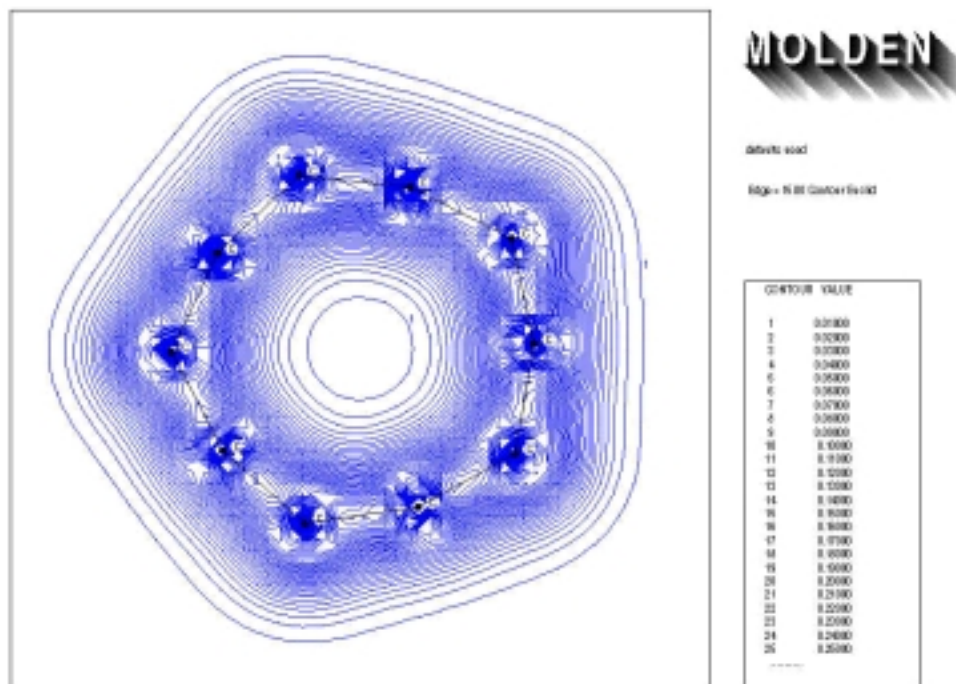
Figure B.18: Carbon Decamer Electron Density

References

[AT95a] M. Abdulkhadar and B. Thomas. "DC Conductivity and Dielectric Properties of Nano-Particles of Red Mercuric Iodide." *Cyrstal Research and Technology*, **30**:723–728, 1995.

[AT95b] M. Abdulkhadar and B. Thomas. "Study of Dielectric Properties of Nano-Particles of Cadmium Sulphide." *Physica Status Solidi A*, **150**:755–762, 1995.

[Atk82] P. W. Atkins. *Physical Chemistry*. W. H. Freeman and Co., 2 edition, 1982.

[Atk86] P. W. Atkins. *Molecular Quantum Mechanics*. Oxford University Press, 1986.

[Bur73] J. J. Burton. "On The Validity of Homogeneous Nucleation Theory." *Acta Metallurgica*, **21**:1225–1232, 1973.

[Car98a] D. L. Carroll et al. "Effects of Nanodomain Formation on the Electronic Structure of Doped Carbon Nanotubes." *Physical Review Letters*, **81**:2332–2335, 1998.

[Car98b] D. L. Carroll et al. "Spatial Variations in the Electronic Structure of Pure and b-Doped Nanotubes." In *EMRS 1997 Meeting, Symposium A: Fullerenes and Carbon Based materials*, volume 36, pp. 753–756. Carbon, 1998.

[Chi98] H. Chiriac et al. "Giant Magneto-Impedance Effect in Nanocrystalline Glass-Covered Wires." In *7th Joint Magnetism and Magnetic Materials-Intermag Conference*, volume 83, pp. 6584–6586. J. Applied Physics, 1998.

[Cur79] E. T. Curan. *An Investigation of Flame Stability in a Coaxial Dump Combustor*. PhD thesis, Air Force Institute of Technology, 1979.

[Dau83] R. Daudel et al. *Quantum Chemistry*. John Wiley & Sons Ltd., 1983.

[Dra72] R. L. Drake. In G. M. Hidy and J. R. Brock, editors, *Topics in Current Aerosol Research*, volume 3, p. 201. Pergamon, Oxford, 1972.

[DW87] A. M. Dean and P. R. Westmoreland. "Bimolecular QRRK Analysis of Methyl Radical Reactions." *Int. J. Chem. Kinetics*, **19**:207–228, 1987.

[Fan98]   H. C. Fang et al. "Preparation and Magnetic Properties of (Zn-Sn) Sub-
           stituted Barium Hexaferrite Nanoparticles for Magnetic Recording." *J.
           Magnetism and Magnetic Materials*, **187**:129–135, 1998.

[Fri01]   M. J. Frisch et al. *Gaussian 98 (Revision A.1x)*. Gaussian, Inc., Pitts-
           burgh, PA, 2001.

[Gaz98]   F. Gazeau et al. "Magnetic Resonance of Ferrite Nanoparticles: Ev-
           idence of Surface Effects." *J. Magnetism and Magnetic Materials*,
           186:175–187, 1998.

[GC89]   S. L. Girshick and C. P. Chiu. "Homogeneous Nucleation of Particles
           from the Vapor Phase in Thermal Plasma Synthesis." *Plasma Chem-
           istry and Plasma Processing*, **9**(3):355–369, 1989.

[Gel80]   F. Gelbard et al. "Sectional Representations for Simulating Aerosol
           Dynamics." *J. of Colloid and Interface Science*, **76**(2):541–556, 1980.

[Gla41]   S. Glasstone et al. *The Theory of Rate Processes*. McGraw-Hill Book
           Co., 1941.

[Gla87]   I. Glassman. *Combustion*. Academic Press, Inc., 2 edition, 1987.

[GT84]   Jr. Gardiner, W. C. and J. Troe. "Rate Coefficients of Thermal dissoci-
           ation, Isomerization, and Recombination Reactions." In Jr. W. C. Gar-
           diner, editor, *Combustion Chemistry*, pp. 173–196. Springer-Verlag,
           1984.

[HA79]   C. D. Holland and R. G. Anthony. *Fundamentals of Chemical Reaction
           Engineering*. Prentice-Hall, 1979.

[INS88]   INSPEC, Inst. Elec. Eng. *Properties of Silicon*, 1988.

[Joh66]   H. S Johnston. *Gas Phase Reaction Rate Theory*. The Ronald Press
           Co., 1966.

[Kai98]   L. Kai et al. "Giant Positive Magnetoresistance in Arrays of Semi-
           Metallic Bismuth Nanowires." In *7th Joint Magnetism and Mag-
           netic Materials-Intermag Conference*, volume 34, pp. 1093–1095. IEEE
           Transactions on Magnetics, 1998.

[Kar87]   J. Karch et al. "Ceramics Ductile at Low Temperature." *Letters to
           Nature, Nature*, **330**, 1987.

[Kas28a]   L. S. Kassel. "The Distribution of Energy in Molecules." In *Proc. Nat.
           Acad. Sci.*, volume 14, pp. 23–30, 1928.

[Kas28b] L. S. Kassel. "Studies in Homogeneous Gas Reactions I." *J. Phys. Chem.*, **32**:225–242, 1928.

[Kas28c] L. S. Kassel. "Studies in Homogeneous Gas Reactions II, Introduction of Quantum Theory." *J. Phys. Chem.*, **32**:1065–1079, 1928.

[Kas32] L. S. Kassel. *The Kinetics of Homogeneous Gas Reactions.* The Chemical Catalog Company, Inc., 1932.

[Kno98] M. Knobel. "Giant Magnetoimpedance in Soft Magnetic Amorphous and Nanocrystalline Materials." In *J. de Physique IV (Proceedings)*, volume 8, pp. 213–220, 1998.

[Kon97] I. A. Konovalov et al. "High Sensitive Strain Microsensor Based on Dielectric Matrix with Metal Nanoparticles." In E. P. George et al., editors, *Materials for Smart Systems II, Symposium*, volume 36, pp. 261–265. Mater. Res. Soc., 1997.

[LA78] B. Lewis and J.C. Anderson. *Nucleation and Growth of Thin Films.* Academic Press, 1978.

[Lin84] M. R. Lindeburg. *Mechanical Engineering Review Manual.* Professional Publications, 7 edition, 1984.

[Low93] J. P. Lowe. *Quantum Chemistry.* Academic Press, 2 edition, 1993.

[MC80] A. D. McLean and G. S. Chandler. *J. Chem. Phys.*, **72**:5639–5648, 1980.

[Mor97] C. Morrison et al. "Fuel Sensitivity Studies Based On A Design System for High Speed Airbreathing Combustors." XIII ISABE Conf., September 1997.

[Oat85] G. C. Oates. *Aerothermodynamics of Aircraft Engine Components.* AIAA, Inc., 1985.

[Pan96] S. V. Pan'kova et al. "The Giant Dielectric Constant of Opal Containing Sodium Nitrate Nanoparticles." *J. Physics: Condensed Matter*, **8**:L203–6, 1996.

[Par64] D. A. Park. *Introduction to the Quantum Theory.* McGraw-Hill Book Co., 1964.

[PB70] J. A. Pople and D. Beveridge. *Approximate Molecular Orbital Theory.* McGraw-Hill Book Co., 1970.

[PC73]   R. H. Perry and C. H. Chilton, editors. *Chemical Engineers' Handbook.* McGraw-Hill Book Co., 5 edition, 1973.

[Pre58]   R. D. Present. *Kinetic Theory of Gases.* McGraw-Hill Book Co., 1958.

[Rao95]   N. P. Rao et al. "Nanoparticle Formation Using a Plasma Expansion Process." *Plasma Chemistry and Plasma Processing*, **15**(4):581–606, 1995.

[RH72]   P. J. Robinson and K. A. Holbrook. *Unimolecular Reactions.* John Wiley & Sons Ltd., 1972.

[RM89]   N. P. Rao and P. H. McMurry. "Nucleation and Growth of Aerosol in Chemically Reacting Systems. A Theoretical Study of the Near-Collsion-Controlled Regime." *Aerosol Science and Technology*, **11**:120–132, 1989.

[Row94]   R. L. Rowley. *Statistical Mechanics for Thermophysical Property Calculations.* Prentice-Hall, 1994.

[Sch63]   M. W. Schmidt et al. "General Atomic and Molecular Electronic Structure System." *Journal of Computational Chemistry*, **14**:1347–1363, 1963.

[Sen92]   S. M. Senkan. "Detailed Chemical Kinetic Modeling: Chemical Reaction Engineering of The Future." In *Advances in Chemical Engineering*, volume 18, pp. 95–196. Academic Press, Inc., 1992.

[Sha]   S. Sharafat et al. "A Plasma-Based Experiment for Nanocluster sysnthesis & Engineered Applications.".

[Sha53]   A. H. Shapiro. *The Dynamics and Thermodynamics of Compressible Fluid Flow.* The Ronald Press Co., 1953.

[Sie96]   R. W. Siegel. "Creating Nanophase Materials." *Scientific American*, pp. 74–79, December 1996.

[SN00]   G. Schaftenaar and J. H. Noordik. "Molden: a pre- and post-processing program for molecular and electronic structures." *J. Comput.-Aided Mol. Design*, **14**:123–134, 2000.

[SP98]   J. H. Seinfeld and S. N. Pandis. *Atmospheric Chemistry and Physics; From Air Pollution to Climate Change.* John Wiley & Sons, Inc., 1998.

[Ste87]   J. J. P. Stewart. "MOPAC: A General Molecular Orbital Package." *QCPE*, p. 455, 1987.

[Ste89]   J. J. P. Stewart. *J. Comp. Chem.*, **10**:209, 1989.

[Sto90]   C. A. Stone. *A Kinetic Rate Model Simulationof the Initial Stages of Thin Film Nucleation and Growth Under Low-Energy Particle Bombardment.* PhD thesis, University of California, Los Angeles, 1990.

[Stu91]   G. D. Stucky. "Nanochemistry and Nanoclusters: The Beginning of Matter." *Naval Research Reviews*, **3**:28–39, 1991.

[Sub98]   L. Suber et al. "Size and Shape Effect on the Magnetic Properties of Alpha-Fe2O3 Nanoparticles." In *Mechanically Alloyed, Metastable and nanocrystalline Materials, International Symposium*, volume 269–272, pt. 2:, pp. 937–942. Materials Science Forum, 1998.

[TA95]   B. Thomas and M. Abdulkhadar. "Dielectric Properties of Nano-Particles of Zinc Sulphide." *J. Physics*, **45**:431–438, 1995.

[VG92]   M. Vicanek and N. M. Ghoniem. "Two-Group Approach to the Kinetics of Particle Cluster Aggregation." *Journal of Computational Physics*, **101**(1), July 1992.

[Wan98]   W. Wang et al. "Nanoparticle Morphology in a Granular Cu-Co Alloy with Giant Magnetoresistance." *Applied Physics Letters*, **72**:1118–1120, 1998.

[Wea81]   R. C. Weast, editor. *CRC Handbook of Chemistry and Physics.* CRC Press, 61 edition, 1981.

[Wei94]   Q. Wei. *"Modeling of Nanosize Silicon Particle Synthesis in a Plasma Reactor."*. Master's thesis, University of Minnesota, 1994.

[Wes71]   P. R. Westmoreland et al. "Prediction of Rate Constants for Combustion and Pyrolysis Reactions by Bimolecular QRRK." *AIChE Journal*, **32**(12), 1971.

[Wu87]   J. J. Wu. "A Method for the Synthesis of Submicron Particles." *Langmuir*, **3**(2):266–271, 1987.